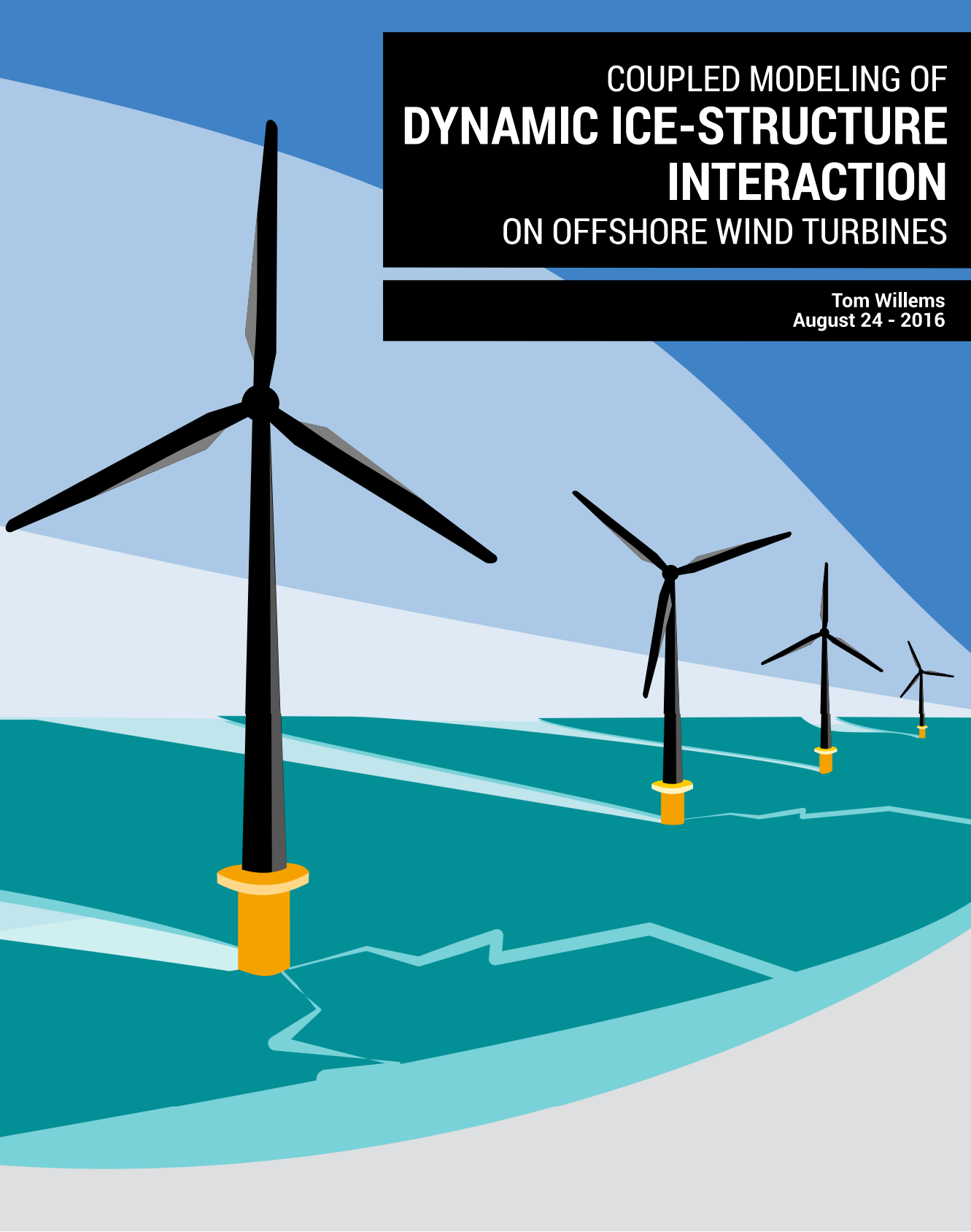

COUPLED MODELING OF DYNAMIC ICE-STRUCTURE INTERACTION ON OFFSHORE WIND TURBINES

Tom Willems
August 24 - 2016

TU Delft

SIEMENS

Coupled modeling of dynamic ice-structure interaction on offshore wind turbines

Master of Science Thesis

Author:	Tom Willems	
Committee:	Prof. Dr. A. Metrikine	TU Delft - Chairman
	Ir. H. Hendrikse	TU Delft
	Ir. J.S. Hoving	TU Delft
	Dr. Ir. S.N. Voormeeren	Siemens Wind Power
	Ir. A.K. de Groot	Siemens Wind Power
	Ir. B. Verheugt	Siemens Wind Power

August 24, 2016

TU Delft Delft University of Technology

SIEMENS

Summary

The offshore wind industry is growing at high pace and is already one of the major renewable energy sources in Europe. To support this growth, costs must be further decreased, amongst others by efficiently designing the support structure of the offshore wind turbines. This requires accurate prediction of environmental loading such as dynamic ice-structure interaction. From industry practice it is known, that current phenomenological models show results that are highly sensitive to the used input parameters. In this thesis it is investigated if the methodology used in industry practice, can be improved by coupled phenomenological modeling of dynamic ice-structure interaction.

First, an introduction is given on the growing process and the properties of sea ice. These properties are related to the deformation and failure behavior of the ice. The failure behavior is divided into three regimes: the ductile regime, the transitional regime and the brittle regime.

The ice load at which brittle failure occurs seems to decrease with increasing deformation rate. However, since this is debated in literature, a phenomenological approach is used to describe dynamic ice-structure interaction. The phenomena are related to the aspect ratio b/h and the ice velocity v_{ice} and denoted as failure modes. The failure modes for ice failing against a vertical structure are: creep, crushing, and buckling.

During crushing failure against a compliant structure, three ice-induced vibration regimes can occur: Intermittent crushing, frequency lock-in, and continuous brittle crushing. The ice-induced vibrations are often modeled in a phenomenological manner since the physics behind the phenomena are not well understood. A recently published phenomenological model by Hendrikse and Metrikine (2015a), is based on the variation of contact area at the interaction surface between the ice and the structure.

The phenomenological model proposed by Hendrikse and Metrikine (2015a) is implemented and extended with creep and buckling. The model entails elastic-visco-plastic elements that deform inelastically at lower deformation rates, enabling the contact area to increase. Moreover, buckling is included to the model by the implementation of a finite element model. Here, the ice sheet is represented by a wedge-shaped beam on an elastic

Winkler foundation.

The phenomenological model is implemented numerically to simulate dynamic ice-structure interaction in the time domain. The model uses a Newmark scheme for nonlinear dynamics to solve the system of equations iteratively. Moreover, a variable time stepping algorithm is created to increase the accuracy of the results.

The input parameters of the model are derived from reference data that is obtained from full-scale measurements. The measurement data is acquired and translated to the reference parameters enabling to realistically model the ice-structure interaction. A verification study is performed to demonstrate that the reference parameters are matched. Furthermore, a qualitative verification is successfully performed on the failure modes and ice-induced vibration regimes.

In the second part of this thesis, the phenomenological model is applied to a structural model of an offshore wind turbine and investigated in two case studies. For the implementation of the structural model, firstly the phenomenological model for ice-structure interaction is adjusted for cylindrical structures. The adjustments involved a reduction in the longitudinal ice load and the introduction of lateral loading. Aerodynamic damping and thrust are included to enable simulations of the ice-structure interaction during the production of electrical energy.

The coupled model is applied in two cases. The first case considered an offshore wind turbine model, with ice loading as the only subjected load to the structure. The second case considers the combination of ice and wind loading.

In the first case resonance behavior, unrelated to frequency lock-in, is observed during the intermittent crushing regime. In the second case it is shown that the phenomenological model predicts an ice-induced decrease in fatigue damage at mudline, at ice velocities where intermittent crushing is occurs. Moreover, due to aerodynamic effects, frequency lock-in does not occur in the specific case study.

A comparison is made between coupled and uncoupled models for ice-structure interaction. The uncoupled models use an external ice load series to represent the ice-structure interaction and are based on methodology used in industry practice. The same cases as for the coupled model are considered.

In case of ice-only loading, it is concluded that the uncoupled model is not capable of capturing intermittent crushing and frequency lock-in behavior due to inconsistency between the load signal and the response. In case of combined ice and wind loading, it is concluded that the uncoupled model is incapable of capturing intermittent crushing behavior and the ice-induced decrease in fatigue damage. The same inconsistency is used as an explanation.

Acknowledgements

Since this thesis is finished, I have opened a small beer to celebrate with Michiel (it is nine o'clock in the evening) and started on writing the acknowledgments. Firstly, I must elaborate on the amazing time I had in the past nine months. Besides the fact that ice-structure interaction was an inspiring and motivating subject, I had a lot of fun in the office as well. That is why I will start with thanking my fellow students and my future colleagues at Siemens Wind Power. Sometimes you made me crawl under the football table, but many more times we could settle it on Friday afternoon.

I also want to thank my large team of supervisors. First of all thanks to Hayo for all the help with the model. I really appreciated the fact that any email I sent to you was answered within a day, including elaborate explanations and derivations on the parameters. Thanks to Jeroen for the afternoons with the (badly working) pencils and the whiteboard, helping me figure out how stick and slip really works. And of course thanks to professor Metrikine for asking me the difficult questions that pushed me to go the extra mile.

I would like to thank Sven for his lectures on dynamics and his tips on how to approach this project, I never expected to learn so many things during this project. I also never saw anyone programming that fast in MATLAB as well. Thanks to Anneke for all her support during the countless meetings we had and always reminding me to keep having fun. Having fun was not a problem at all, certainly not with the amazing team I had to support me. Of course I also want to thank Bas for all the sparring sessions, and Paul for his match box collection.

Finally, thanks to my parents for supporting me during my studies and many thanks friends and my lovely girlfriend for supporting me and accepting the fact that I was living under as stone for the past few months. I had a great time doing this project and writing this thesis, I hope you enjoy reading.

The Hague, August 2016,

Tom Willems

Contents

Nomenclature

Latin symbols

A	Area	m^2
A	Rotor area	m^2
b	Structure width/diameter	m
b_0	Floating wedge width at ice-structure interface	m
$\boldsymbol{C}$	Damping matrix	Ns/m
C	Damping	Ns/m
C^*	Modal damping	Ns/m
C_T	Thrust coefficient	$-$
D	Fatigue damage	$-$
D	Flexural stiffness	Nm^2
E	Expected value	$-$
E	Young's modulus	Pa
$f1$	Maximum deflection tolerance	$-$
F_crit	Dry friction activation force	N
F_fric	Friction force	N
F_mean	Mean load at v_ref	N
F_n	Normal load	N
f_peak	Peak frequency	Hz
f_n	Natural frequency	Hz
F_std	Standard deviation of the load at v_ref	N
F_{con}	Reaction load due to confinement	N
F_t	Tangential load	N
F_trans	Mean load at v_trans	N
P_trans	Measured pressure at v_trans	Pa
F_2vtrans	Mean load at $2v_\mathrm{trans}$	N
P_2vtrans	Measured pressure at $2v_\mathrm{trans}$	Pa

F_{wedge}	Horizontal load on a wedge	$-$
F_{w}	Thrust	N
$\boldsymbol{g}$	External load vector	N
G	Shear modulus	Pa
g	Gravitational constant	m/s^2
h	Ice thickness	m
$\boldsymbol{I}$	Identity matrix	$-$
I	Moment of inertia	m^4
i	Number of the amplitude ranges	$-$
j	Total number of amplitude ranges	$-$
$\boldsymbol{G}$	Geometric stiffness matrix	N/m
$\boldsymbol{K}$	Stiffness matrix	N/m
$\boldsymbol{r}$	Residual vector	$-$
K	Stiffness	N/m
K^*	Modal stiffness	N/m
$\boldsymbol{K}_{\text{W}}$	Winkler foundation stiffness matrix	N/m
L_{el}	Element length	m
L_{bf}	Buckling failure length	m
$\boldsymbol{M}$	Mass matrix	kg
m	Wohler constant	$-$
M^*	Modal mass	kg
N	Maximum number of cycles before failure	$-$
N	Number of creep-crushing elements	$-$
N_{sim}	Number of performed simulations	$-$
N_{wedge}	Number of wedges	$-$
P	Horizontal load on a floating wedge	m
P_{mean}	Mean pressure	Pa
P_{std}	Standard deviation of pressure	Pa
r	Element offset	m
T	Temperature	K
t	Time instance	s
Δt	Time step size	s
t_{f1}	Time to maximum deflection	s
t_{fail}	Time to failure	s
t_{ini}	Initialization time	s
T_m	Melting temperature	K

t_{peak}	Peak time instance	s
U	Uniform distribution	$-$
u	Deflection	m
$\dot{u}$	Velocity	m/s
V_b	Brine volume fraction	%
v_{ice}	Ice velocity	m/s
v_{trans}	Transition velocity	m/s
V_{w}	Wind velocity	m/s
w	Vertival deflection	m
y	Direction of the ice velocity	$-$

Greek symbols

α	Coefficient for determining C_2	-
β	Coefficient for determining K_2	-
γ	Coefficient for determining F_{crit}	-
γ_{w}	Specific weight of water	N/m^3
δ_{crit}	Critical elastic deformation	m
ϵ	Strain	$-$
ϵ_e	Elastic strain	$-$
ϵ_{tot}	Total strain	$-$
ϵ_{ve}	Visco-elastic strain	$-$
ϵ_{vp}	Visco-plastic strain	$-$
ζ	Damping ratio	$-$
$\boldsymbol{\eta}$	Modal amplitude vector	$-$
$\dot{\boldsymbol{\eta}}$	Modal velocity vector	$-$
η	Porosity	%
ν_{ice}	Poisson's ratio	rad
$\boldsymbol{\Phi}$	Eigen matrix	$-$
$\boldsymbol{\phi}$	Eigen vector	$-$
ϕ	Angle along the circumference of a cylindrical structure	rad
ϕ^*	Wedge angle	rad
ϕ_{rc}	Radial crack angle	rad
ϕ_{MSL}	Mode shape amplitude at MSL	$-$
ρ_{ice}	Ice density	kg/m^3
ρ_a	Air density	kg/m^3
ρ_w	Water density	kg/m^3

σ_c^H	Horizontal compressive strength	MPa
σ_c^V	Vertical compressive strength	MPa
σ_f	Flexural strength	MPa
σ_t	Tensional strength	MPa
τ	Shear strength	%
$\mathbf{\Omega}$	Frequency matrix	$-$
ω	Eigen frequency	rad/s

Subscripts

b	Buckling
i	Element number
max	Maxium
min	Minimum
ref	Reference
n	Time step number
s	Structural

Superscripts

T	Transpose

Abbreviations

BHawC	Bonus Horizontal axis wind turbine Code
DEL	Damage Equivalent Load
FLI	Frequency lock-in
hpz	High pressure zone
HSVA	Hamburgische Schiffbau-Versuchsanstalt
IIV	Ice-induced vibrations
LCoE	Levelized Cost of Electricity
OWT	Offshore wind turbine
RNA	Rotor Nacelle Assembly

Chapter 1
Introduction

As oil prices fluctuate with high uncertainty, the world's leading economies need to improve on the risks of their energy resources. Offshore wind energy is currently one of the most stable sources of renewable energy in Europe and therefore growing at high pace. It is expected that the in total 8GW installed by the end of 2014, will be increased to 23.5GW by 2020 (Ernst & Young et Associés, 2015). This growth is boosted by the Paris agreement adopted by 195 countries in December 2015 (European Commission, 2015). However, offshore wind energy still remains relatively expensive. Therefore, in the long term, energy production costs must be reduced. A common way to measure these costs is by comparing the Levelized Cost of Electricity (LCoE). The LCoE incorporates all costs incurred during the lifetime of an energy source and the total amount of energy delivered. To give the reader some insight in the current costs of energy Table 1.1 is shown. It gives a comparison of LCoE's for the European market in 2015.

Table 1.1: Average LCoE per energy source in 2015 [euro/MWh] VGB PowerTech e.V. (2015)

Conventional energy source	**Average LCoE**
Gas	110
Coal	78
Nuclear	60
Renewable energy source	
Offshore Wind	118
Solar Panels: Utility Scale	108
Onshore Wind	72

Table 1.1 shows that renewable energy is already cost competitive to conventional sources. However, offshore wind is still relatively expensive. Predictions assume that the LCoE for offshore wind will decrease to 90 euro/MWh by 2030 (Ernst & Young et Associés, 2015). Recent contracts have shown that projects can already be realized at LCoE of 72.7

euro/MWh , demonstrating potential cost savings (DONG Energy, 2016).

To enable these cost reductions, a number of factors have to be improved. Besides the optimization of commercial and logistic processes, many technical improvements are still to be made. These technical improvements include more efficient and higher capacity turbines, which have to be carried by larger and cheaper support structures.

To reduce the cost of the support structure one must carefully find a design optimum. The driving design factor behind these tall structures over 100m , is the environmental loading and the corresponding dynamic responses. Uncertainties in the environmental loading will force the engineer to use a conservative approach. Subsequently, a conservative approach results in over designing the support structure. Therefore, it is vital to accurately and correctly determine the environmental loads encountered by the offshore wind turbine (OWT).

Figure 1.1: Ice cover in the Baltic Sea. From left to right: a mild, an average, and an extreme winter (ISO 19906, 2010)

This thesis focuses on the prediction of the little-known dynamic responses induced by floating ice. One could raise the question if this is necessary, as no plans for wind farms in arctic conditions exist. However, floating ice is seen almost every year in the Baltic Sea where many wind farms are under construction and planned. Figure 1.1 shows a map during a mild, an average, and an extreme winter. The marked area shows the sea surface covered by floating ice. From this illustration one could conclude that floating ice should be considered as a serious threat to offshore wind farms near the east coast of Denmark.

Solutions to mitigate the risks of interaction between ice and OWT's are already applied to some of the wind farms in this area. For example the Nysted Windfarm near Denmark, shown in Figure 1.2, makes use of concrete conical structures at water level to reduce the ice load. However, these concrete structures are expensive and a conical shape at mean sea

Figure 1.2: Nysted wind farm near the coast of Denmark (Boesen and Corlin Hassing)

level increases the diameter at that location. The latter results in higher wave loading for the larger part of the year. Alternatively, a method is required to more accurately predict the dynamic effects of interaction between ice and OWT's.

1.1. Motivation and current practice

The load exerted by the ice depends on the structural response; the interaction between a structure and the ice is of major importance to predict the response of a structure. This means that not only the structural response is depending on the ice load, but the ice load is also depending on the structural response. Many ice-structure interaction models therefore make use of coupling between the ice and the structure.

From experience at Siemens Wind Power, the methods currently used in industry are varying from the application of relatively simple design rules like ISO19906, to the usage of sophisticated coupled ice-structure interaction models. The methods all have in common that an ice-load time series is first generated and then applied to an OWT model in a combination with wind loading.

At Siemens Wind Power, the Bonus Horizontal axis wind turbine Code (BHawC) is used to realistically model the OWT as it is exposed to the ice load. For commercial reasons the ice load is often generated by a consultant, using merely the mode shapes and frequencies of the BHawC model as an input. While the load series is produced in a coupled manner, it is applied in an uncoupled way. Differences in the structural model, and the effect of aero-

dynamic loading are therefore not included in the ice load. In other words, only coupling between ice and structure in incorporated. However, the influence of structural motion originating from other external loads is neglected. In-house experience has shown that this results in large variations in the structural response raising questions on the reliability and accuracy of the method.

The most commonly used model today is an advanced ice-structure interaction model created by Karna et al. (1999). This model has shown promising results on a wide variety of projects. However, the results of this model showed that the response is highly sensitive to the input parameters. Moreover, the parameters that define the ice are depending on the structural properties which seems nonphysical. Recently Hendrikse and Metrikine (2015a) published a proposal for a phenomenological model based on a novel approach to ice-structure interaction. The ice parameters are independent of the structural parameters and therefore it is considered as a more realistic alternative.

1.2. Thesis objectives and outline

The combination of the questionable reliability of uncoupled simulations, and the recently published model result in two objectives. These objectives will form the basis of this thesis.

The first objective is to create a coupled model that can predict the response of a structure subjected to ice-structure interaction. The model is be based on the phenomenological model published by Hendrikse and Metrikine (2015a). Extensions are made to include the most important phenomena that occur during ice-structure interaction.

The second objective is to quantify the difference between the fully coupled simulations and the models used in current practice. This is done to study the accuracy of the current models, and investigate if a coupled model can contribute to a more efficient OWT design.

1. **Create a coupled model for dynamic ice-structure interaction on offshore wind turbine support structures**
2. **Compare the the results of the coupled model and uncoupled modeling as is more commonly applied in industry**

Based on the two objectives, the thesis is divided in two separate parts. The first part contains the extension and implementation of the numerical model for ice-structure interaction. Part I starts with an introduction to the properties of sea ice in chapter 2. As the knowledge on the mechanics of ice is limited a step is made to the phenomenological approach in chapter 3. The extended numerical model used to describe these phenomena is discussed in chapter 4. The first part is concluded by chapter 5 on the implementation and verification of the described model.

The second part contains the application of the phenomenological model to an offshore wind turbine. The part starts with the implementation of the OWT to the ice-structure interaction model discussed in the first part in chapter 6. The differences between coupled modeling and uncoupled are studied in chapter 8. Finally, the thesis is concluded in chapter 9 with the conclusions following from the defined objectives, and recommendations for future research.

Part I
Extension and implementation of a phenomenological model for dynamic ice-structure interaction

Chapter 2
Properties of sea ice

The interaction between ice and offshore structures is known to be a complex process. The material properties of ice, and even more the phenomena induced by this interaction are still not well understood. Even though the phenomenological model used for the research in this thesis will not be based on the physical properties of ice, the reader requires basic knowledge on the physical and mechanical properties of ice to understand the mechanism used and the choices that have been made.

Firstly, section 2.1 gives an overview on the growth process of ice. It starts at molecular scale and follows the ice until it has grown to a first-year ice sheet. Based on this growing process four physical properties are deducted and related to the strength of the ice in section 2.2. The chapter is concluded by the mechanical behavior of the ice sheet in section 2.3. It must be emphasized that the properties found in this chapter are the results of small-size experiments done in a laboratory as well as in the field.

2.1. Ice physics

To study the interaction between sea ice and offshore wind turbines, the macroscopic properties of sea ice are of the most interest. However, these large scale properties are mere averages of the continuous ice-sheet. To understand the phenomena happening during the interaction between an ice sheet and a structure, one requires at least basic knowledge of the physics behind the material. This section gives a comprehensive overview on the growth process of an ice sheet and aims to help the reader to get a feeling for the structure of the material. The section is build up from the molecular scale to the properties of a full scale ice sheet. First the crystal properties are discussed followed by the formation of the primary ice sheet. Next, the secondary ice which grows below the primary ice is treated, followed by the existence of brine pockets. Finally an overview of the formed ice sheet is given.

2.1.1. Ice crystals

The properties of an ice sheet are in fact determined by the microscopic properties, which depend on the distribution, size, and shape of the ice crystals (Petrich and Eicken, 2010). When a closer look is taken at the properties of ice, one will immediately notice the unusual characteristic that ice has a lower density compared to its liquid form. It causes the ice to float on rivers and seas, and enables aquatic life to exist in temperate or polar regions. The fact that ice has such low density properties is caused by its open crystal structure. Although many crystal structures for ice exist, hexagonal ice is the only structure that exists in significant quantities on Earth (Weeks and Ackley, 1986). A drawing of the structure of hexagonal ice is given in Figure 2.1

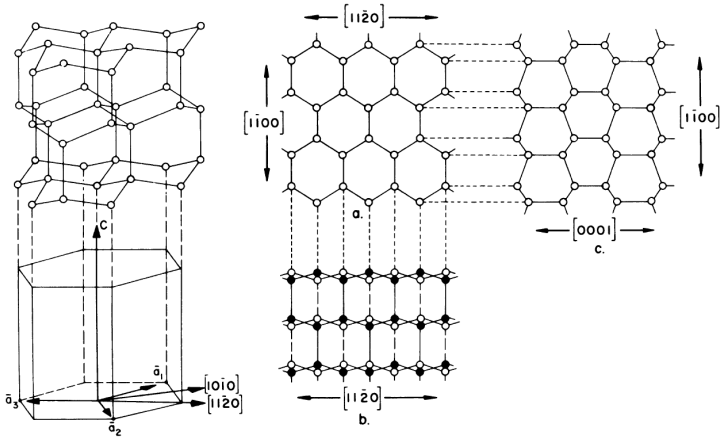

Figure 2.1: Hexagonal crystal structure of ice (Weeks and Ackley, 1986)

Weeks and Ackley (1986) explain how the oxygen atoms are concentrated in a series of parallel planes that are referred to as basal-planes. In Figure 2.1 the basal plane is denoted with 'a.', and can easily be recognized by the hexagonal shapes in top view. The basal planes are stacked on top of each other in a direction that is called the c-axis. Each oxygen atom has three hydrogen bonds in the basal plane and one in the direction of the c-axis. The concentration of hydrogen bonds in the basal planes is therefore higher than the concentration in the direction of the c-axis. From this fact on molecular scale two conclusions are drawn that will help us understand phenomena discussed further on in this thesis.

1. One would need to break more hydrogen bonds in the the basal plane compared to the amount of hydrogen bonds in the direction of the c-axis to induce failure of the crystal. Therefore, the strength of the crystal is anisotropic, i.e. not equal in all directions. The fact that ice glides and cleaves along its basal plane can thus be explained by its crystal structure.

2. As the concentration of hydrogen bonds is higher in the direction of the basal plane, it is more attracted to forming new bonds in that direction. Therefore, the crystal will grow faster in the direction of the basal plane compared to the direction of the c-axis, with ratios up to 100:1 (Hobbs, 1974). A likable example of this phenomenon is the growth of snow flakes. The dendritic growth of ice crystals even adds arms to the crystal as shown in Figure 2.2. However, due to turbulence in sea water and collisions with other crystals these arms will break of in the formation of sea ice (Weeks and Ackley, 1986).

These two statements conclude the subsection on the crystal structure of ice. From this point on a closer look is taken at the growth process off sea ice.

Figure 2.2: Snowflake grown from water vapor (Booth, 2014)

2.1.2. Primary ice

Before there is ice, there will be water. As air starts to cool the water, a thin super-cooled layer will start to form on top op the sea water. In this layer water molecules form hexagonal crystals of pure ice. The salt ions do not fit inside the crystals and will be expelled to the sea water below. As discussed earlier, the crystals will grow faster in the direction of the basal plane. Therefore, they will grow into discoids which can get up to 3 mm in diameter (Figure 2.3(a))(Weeks and Ackley, 1986). The formed mixture of water and ice crystals is often called frazil ice (Figure 2.3(b)). In more turbulent waters the frazil crystals do not in particular stay at the surface but mix with the water column beneath. This causes the super-cooled layer to suspend up to a few meters deep.

Over time, as wind and waves agitate the water surface frazil ice will accumulate into ice clumps. The agglomerations of frazil crystals can take multiple forms before transitioning to

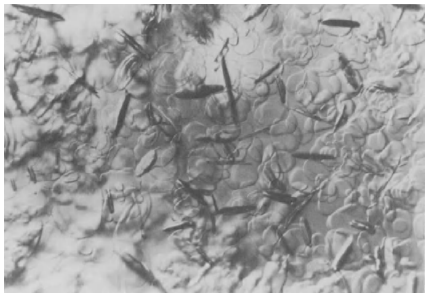

(a) Discoids Weeks and Ackley (1986)

(b) Frazil ice Mills and Tristan (2016)

Figure 2.3

a solid layer of ice. An overview of these forms is described in Petrich and Eicken (2010), but is outside the scope of this thesis. Depending on its form the agglomerated ice will consolidate into a continuous layer of solid granular ice. The newly formed layer of ice has the important characteristic of having randomly oriented ice crystals and therefore is isotropic. The primary ice forms a granular ice sheet of a few centimeters thick and will continue to grow downward into what is called secondary ice.

2.1.3. Secondary ice

The granular ice sheet forms a barrier between the cold air and the sea water at freezing temperature. The heat of the water can only escape trough the ice layer and therefore the growth rate of the secondary ice is determined by the temperature gradient in the ice layer (Weeks and Ackley, 1986). Secondary ice can roughly be divided into two separate layers; the transition zone below the primary ice and the columnar zone below the transition zone. Both will be discussed here briefly.

Transition zone

Since the sea water is covered with a layer of ice, the ice crystals have lost a growth degree of freedom; the ice can only grow downwards. As the crystals will grow faster in the direction of the basal plane, geometric selection will take place. When the downward growth starts, the more favorable oriented crystals will rapidly grow ahead of the less favorable oriented crystals.

Figure 2.4 illustrates a side view of the ice layer where the horizontally growing crystals are being ‘wedged out’ by the more vertically growing crystals. The added layer below the primary ice is called the transition layer and is completed after a growing distance of 5 to 10 cm.

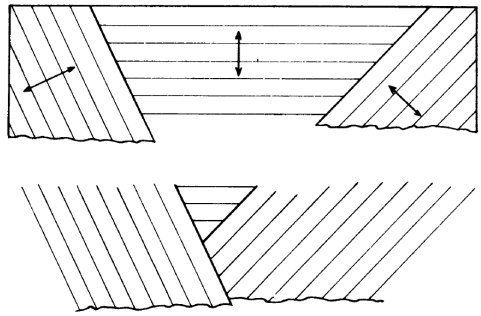

Figure 2.4: Shematic drawing showing the process of geometric selection. The arrows indicate the direction of the c-axis (Weeks and Ackley, 1986)

Columnar zone

Eventually, all crystals will be orientated approximately parallel to each other with their basal planes in the vertical direction. The ice sheet will grow downwards into what is called the columnar zone. The crystals will grow practically vertical, forming long columns. Due to these vertical columns the ice layer will have anisotropic properties, and will be granular in the horizontal direction. Figure 2.5 shows a top view of a horizontal slice of the columnar zone of sea ice. The diameter of the crystals will determine the grain size which is usually around 1 cm (Weeks and Ackley, 1986).

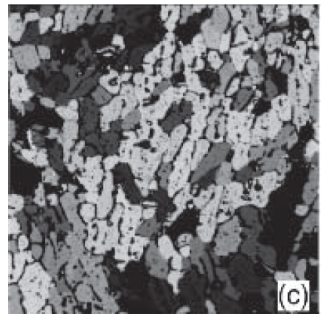

Figure 2.5: Horizontal slice of columnar ice in top view (Petrich and Eicken, 2010)

2.1.4. Brine

After reading the previous section one could ask him or herself the very intelligent question: where did all the salt go? The salt ions did not fit inside the ice crystals and was therefore expelled during the growing process. Part of the salt, together with air, got entrapped

between the columns forming a highly saline solution called brine (Weeks and Ackley, 1986). The brine accumulates in brine pockets between the crystals and moves downwards trough the ice sheet creating brine channels. An elaboration on this process can be read in Petrich and Eicken (2010). For now, it only has to be mentioned that due to these pockets and channels the ice is a porous material. Furthermore, the porosity is dependent on the salinity of the sea water and the temperature of the ice.

2.1.5. Overview of a first year ice sheet

To give an overview of a regular sea ice sheet, a cross-section is show in Figure 2.6. From top to bottom the ice sheet consists of a layer of snow covering the primary ice sheet. The primary ice sheet is granular and isotropic. Below the primary ice secondary ice exists consisting of a transition zone and a columnar zone.

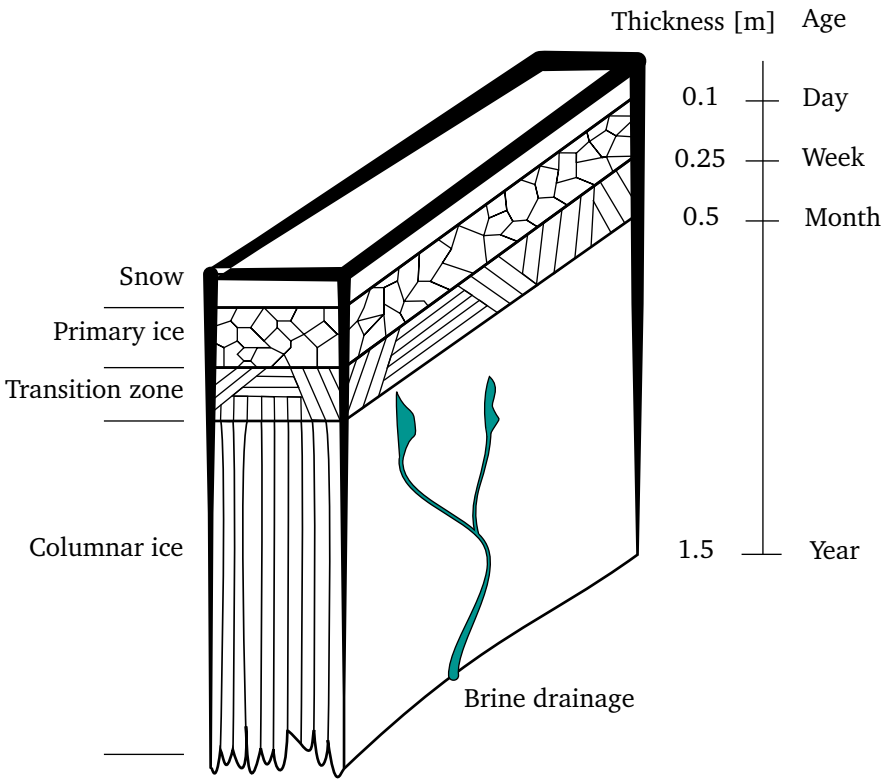

Figure 2.6: Schematic cross-section of ice sheet

2.2. The strength of ice

As described in the previous section, sea ice is a complex material composed of solid ice, gas, and highly saline water. Depending on its formation process, sea ice has an isotropic granular layer on top and an anisotropic columnar layer below. One could summarize the above described ice structure with four physical properties that influence strength of ice.

1. Crystallography
2. Temperature
3. Salinity
4. Porosity

Many measurements in the lab as well as in the field have been done to understand these properties. As complete understanding of the material does not yet exist, empirical relations were derived to approximate values for these properties. Timco and Weeks (2010) show many relations to estimate these properties from in field data. For engineering purposes the more interesting properties like strength are often measured directly. An example of such a measurement, from the author's own experience, is shown in Figure 2.7.

Figure 2.7: Uni-axial compression test on sea ice near Svea, Svalbard

The focus of this section is to show the relation between these properties and the strength of the ice. First the strength profile over the depth of the ice is discussed, followed by an elaboration on the effect of the physical properties on the direction of the strength.

2.2.1. Strength profile

The strength of a material is defined as the stress at which the material fails or plastically deforms. This influence of the physical properties on the strength of ice are discussed here one by one.

Crystallography

The orientation of the crystals differs from top to bottom as shown in Figure 2.6. Due to the random orientation of the crystals in primary ice it is relatively stronger and isotropic compared to the anisotropic columnar zone. Younger ice, or ice composed of multiple layers can have different crystallography profiles. However, in general the top is considered to have the strongest crystallography. As the columnar zone grows over time, a one year old ice sheet consists mainly out of columnar ice and the granular primary ice can therefore be neglected when looking at its strength (Weeks and Ackley, 1986).

Porosity

The porosity of the ice is determined by the volume of the ice sheet that consists of something else than frozen ice. Other materials like brine and gas form pockets inside the ice sheet and make the ice a porous material. Each pocket is a weakness in the ice sheet as no stress is able to flow trough, increasing the stress elsewhere. The size of these pockets depends on the temperature and the salinity of the ice as discussed in subsection 2.1.4.

Temperature

The influence of temperature on the strength of an ice sheet is twofold. Firstly, a lower temperature results in a higher density making the ice stronger. Secondly a higher temperature results in larger brine pockets. Subsequently, larger brine pockets result in a higher porosity and make the ice weaker. Temperature varies over the thickness almost linearly. The temperature at the surface is equal to the air temperature and the temperature at the bottom, in contact with the sea water, is equal to the melting temperature as shown in Figure 2.8.

Salinity

A higher salinity of the sea water results in more brine inside the ice during the growth process. Subsequently, a higher concentration of brine results in larger brine pockets. Measurements of salinity profiles over ice depth are therefore directly related to the concentration of brine pockets. Figure 2.9 shows how the salinity profile varies over the thickness in a C-shape for young ice and changes over time. This change is caused by brine drainage and results in a lower porosity and thus stronger ice as it grows older.

2.2.2. Strength directions

From the previous it can be concluded that in general the strength of ice varies from top to bottom as from strong to weak. Moreover, the strength of ice is highly dependent on the type and direction of loading. This subsection elaborates on the differences in strength for the loading in different directions. Empirical relations for first-year ice described by Timco and Weeks (2010) are shown to give the reader some insight in the proportion between

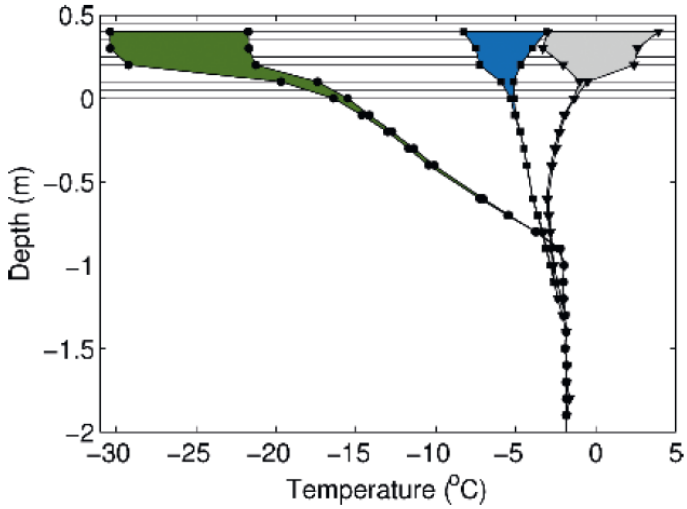

Figure 2.8: Temperature profile over ice depth measured in February (circles) and May (squeares an triangles). Negative depths are sea ice and ocean (Petrich and Eicken, 2010)

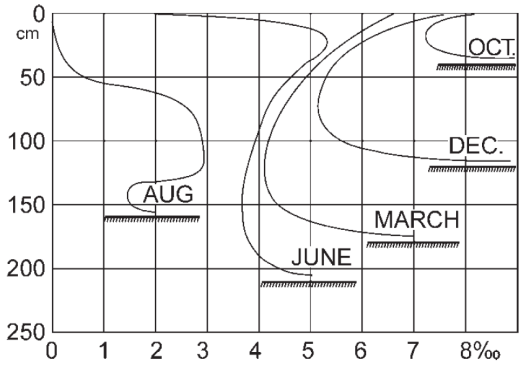

Figure 2.9: Evolution of sea-ice salinity profiles (from Malmgren, 1927). The y-axis shows the depth of the ice an the x-axis shows the salinity in parts per thousand. (Petrich and Eicken, 2010)

the directional strengths and their dependency on the physical properties discussed above. The relations are based on experiments done with first-year ice, at temperatures close to melting.

Compressive strength

For obvious reasons, the compressive strength is of most importance to ice-structure interaction with vertical structures. Due to the crystallography of the ice sheet a difference exists in vertical and horizontal compressive strength. Both share a dependence on porosity η when looking at their empirical relations for uni-axial compressive strength below.

$$\sigma_c^H = 37\dot{\epsilon}^{0.22}\left(1-\sqrt{\frac{\eta}{0.27}}\right) \tag{2.1}$$

$$\sigma_c^V = 160\dot{\epsilon}^{0.22}\left(1-\sqrt{\frac{\eta}{0.2}}\right) \tag{2.2}$$

Here, σ_c^H is the compressive strength in horizontal direction, and σ_c^V is the compressive strength in vertical direction. The observant reader notices that the uni-axial compressive strength also depends on the strain rate $\dot{\epsilon}$. This dependency is caused by the ductile behavior of the ice and will be explained in section 2.3. It must be emphasized that these relations only hold for tests at relatively slow strain rates. At higher strain rates the ice will fail in a brittle manner. For now, it is sufficient to keep in mind that a relation between compressive strength and strain rate exists.

Tensile strength

The tensile strength defines the maximum tensile stress the ice can sustain before failure. It is the strength that is related to the formation of cracks or fracture. It causes open leads in sea ice, enabling large ice floes to separate from land-fast ice and gain velocity e.g. in the direction of a newly built wind farm.

$$\sigma_t = 4.278 \cdot \eta^{-0.6455} \tag{2.3}$$

Due the nature of tensile failure, tests on tensile strength are relatively difficult and time costly. As a consequence not many were reported. However, the tests that have been done show that tensile strength is mainly dependent on the porosity of the ice. Timco and Weeks (2010) show this dependency as Equation 2.3.

Flexural strength

In bending an ice sheet will fail in tension at the location of the highest tensile stress. This is a result from the fact that the tensile strength is lower compared to the compressive strength. For a homogeneous, perfectly elastic beam, one would assume that the flexural strength is equal to the tensile strength. Although this is true for some materials, it is most certainly not the case for ice.

$$\sigma_f = 1.76 \cdot e^{-5.88\sqrt{V_b}} \tag{2.4}$$

Measurements are often done by cutting a beam in the ice sheet, leaving one side attached. By applying a load on the other end of the beam it will fail in bending failure at its root. From these measurements an empirical relation is found relating the downward bending stress to the brine volume fraction V_b shown in Equation 2.4. Since the ice sheet is stronger at the top compared to the bottom, a difference in upward and downward bending strength exists (Timco and Weeks, 2010).

Shear strength

An ice sheet interacting with a structure often encounters biaxial stress involving a combination of tensile and compressive stress or shear stress. Shear stress is usually assumed to occur in a plane of failure. However, in most shear strength experiments also normal stress occurs. This makes performing and the interpretation of the measurements relatively difficult. Although it is one of the least understood properties of ice an empirical relation was found based on the porosity.

$$\tau = 1.5 \left(1 - \sqrt{\frac{\eta}{3.9}}\right) \tag{2.5}$$

It should be noted that the shear strength is not used explicitly when it comes to engineering practice. This is because ice tends to fail in tension before shear failure can occur.

2.3. The mechanical behavior of ice

Up to this point the physical properties and their relation to the failure strength of ice were discussed. However, before the ice fails, deformation takes place. The combination of deformation and eventual failure is referred to as mechanical behavior. This section focuses on the mechanical behavior of ice as it was measured in many research campaigns. The mechanical behavior can be divided in three types; ductile behavior, transitional behavior, and brittle behavior. All three types will be discussed here in that order.

2.3.1. Ductile behavior

A material ideally deforms elastically when it is loaded. After loading it completely recovers into its original form. From this elastic deformation Hooke's law was derived assigning a typical elastic resistance to each material known as the Young's modulus:

$$\epsilon_e = \frac{\sigma}{E} \tag{2.6}$$

Where σ is the applied stress, and E is the Young's modulus. However, for polycrystalline materials like ice, the deformation is divided into different stages. These stages include elastic as well as viscous and plastic behavior. Research on this behavior at low strain rates is oftenly done using so called creep tests. Where creep refers to the creep

failure mode occurring at very low loading rates, discussed in the next chapter. Creep-tests have shown that at relatively high ice temperatures the total strain can be described by a summation of three types of strain and are summed in Equation 2.7 (Sinha, 1983).

$$\epsilon_{tot} = \epsilon_e + \epsilon_{ve} + \epsilon_{vp} \tag{2.7}$$

Where ϵ_e is the elastic strain, ϵ_{ve} is the visco-elastic strain, and ϵ_{vp} is the visco-plastic strain. Under compressive loading with a constant strain rate, the ice will keep deforming in a visco-plastic manner after elastic and visco-elastic behavior have occurred. This visco-plastic behavior is referred to as ductile failure and is related to the creep failure mode. Figure 2.10 illustrates the behavior of the different stages for a creep test. The different stages are described next.

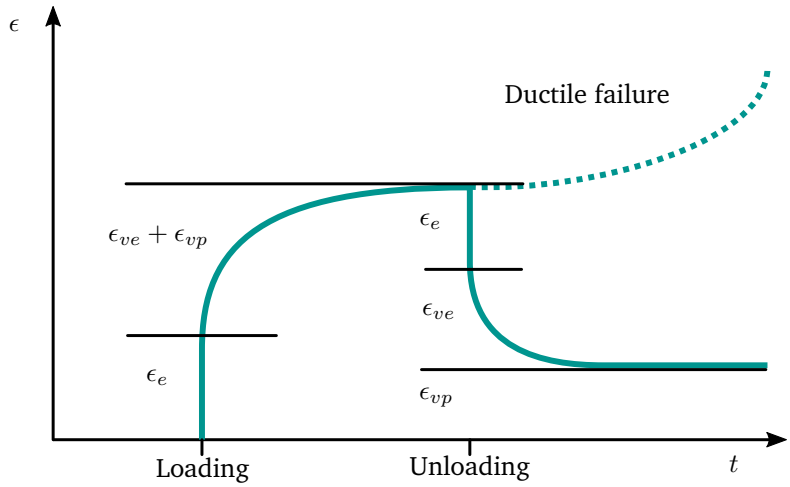

Figure 2.10: Strain versus time curve for a typical creep-test with constant loading Løset et al. (1998)

Elastic behavior

According to Equation 2.6 the ice sample will deform instantaneously when loaded. This represents fully elastic deformation and is therefore fully recoverable. The elastic strain is believed to be caused by the elastic deformation of the crystal lattice due to the applied stress. Using the measurements done by Dantl (1969) and equations proposed by Markham (1969) as was done by Løset et al. (1998) the Young's-modulus in horizontal direction E for columnar ice can be determined as follows:

$$E(T) = 9.39 + 1.3 \cdot 10^{-2} \cdot (T_m - T) \tag{2.8}$$

Where T is the ice temperature, and T_m is the melting temperature in Kelvin. The melting temperature is dependent on the salinity, and the ice temperature is a linear function through the thickness of the ice as discussed in section 2.2. From the above, one could conclude that the elasticity is a linear function through the ice thickness as well.

Visco-elastic behavior

The second deformation is the delayed elastic strain ϵ_{ve}. This deformation is visco-elastic, which means that it is recoverable but time dependent. The delayed elastic strain represents the effect of grain boundaries sliding along each other (Sinha, 1983).

Visco-plastic behavior

Finally, the viscous permanent strain ϵ_{vp} corresponds to the movement of dislocations inside the crystals. Figure 2.11 shows how a movement of a dislocation may look like in a hypothetical crystal structure. The movement of the dislocations is permanent and time dependent. Therefore, it can be described as visco-plastic behavior and results in strain-rate hardening. The latter meaning that the ice strength increases for higher strain rates.

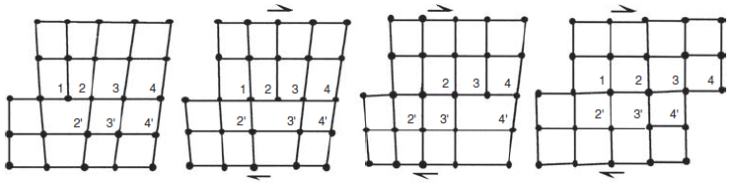

Figure 2.11: Movement of dislocation in a hypothetical cubic crystal Schulson and Duval (2009)

Furthermore, at relatively higher strain rates within the ductile behavior regime, micro cracks arise at the grain boundaries resulting in plastic deformations as well. During the formation of the micro cracks small amounts of stress are released causing an opposite effect known as strain-rate softening (Schulson and Duval, 2009). The formation of these cracks is an important role in the explanation of the phenomenological model used in this thesis.

2.3.2. Ductile to brittle transition

In the results of many creep tests, Sinha shows that his theory only fits until a maximal stress is reached. The maximal stress at which ductile behavior can occur is referred to as the terminal failure stress. When the stress in the ice exceed the terminal failure stress, hence at higher strain rates, the ice will fail in a violent manner by cracking. This behavior is referred to as brittle failure. Figure 2.12 shows stress-strain curves for varying strain rates, where the brittle failure of the ice is denoted with x.

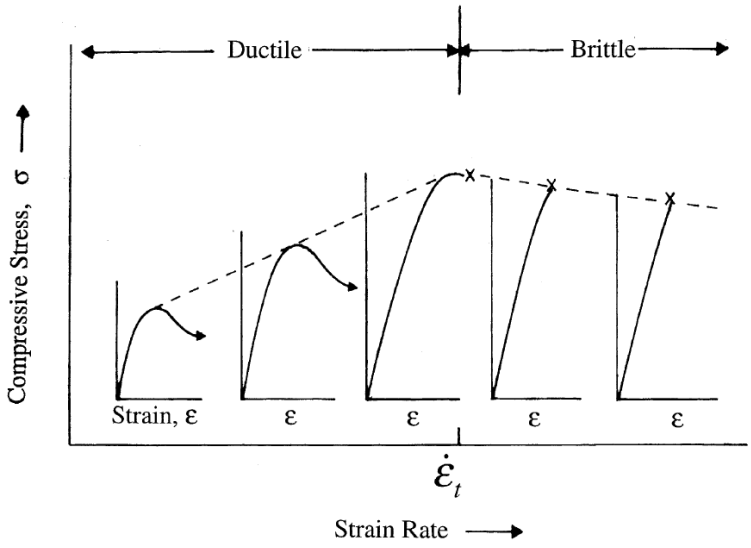

Figure 2.12: Influence of strain-rate on stress-strain curve Schulson and Duval (2009)

The transition from ductile to brittle occurs in a gradual manner rather than abrupt. This gradual transition is caused by the formation of micro cracks in the ice during the transition from ductile to brittle failure as discussed before. Where the movement of dislocations induces strain-rate hardening, the micro cracks induce strain-rate softening. The latter can be explained by the proportion of micro cracks increasing for higher strain rates, hence causing a smooth transition Schulson and Duval (2009).

2.3.3. Brittle behavior

Due to the smoothness in the transition from ductile to brittle behavior, it exists in a range of strain rates. For strain rates higher than this range no ductile failure will occur. The stress-strain curve will be characterized by a pseudo-linear rise in stress, followed by a sudden drop due to the development of a mechanical instability (Figure 2.12). The curves in the brittle regime in Figure 2.12 also exhibit load drops and small negative curvature after it reaches about $1/3$ of the terminal failure stress. These load drops and negative curvature are related to the same creation and growth of micro cracks along the grain boundaries. From the fact that this curvature only occurs after $1/3$ of the terminal failure stress one could conclude that these cracks need a certain activation stress to start forming.

Strain-rate softening

In addition to these effects, strain-rate softening has been described from uni-axial compression tests. A consequence of the combination of strain-rate hardening for ductile be-

havior, and strain-rate softening for brittle behavior, may be that the maximum compressive strength is measured at the transition strain rate as shown in Figure 2.13. However, the existence of strain rate softening is debated in literature. Schulson and Duval (2009) report multiple experiments which seem to indicate this behavior. Timco and Weeks (2010) question the quality of such experiments, as high quality uni-axial laboratory tests show an increasing strength up to very high strain rates as well.

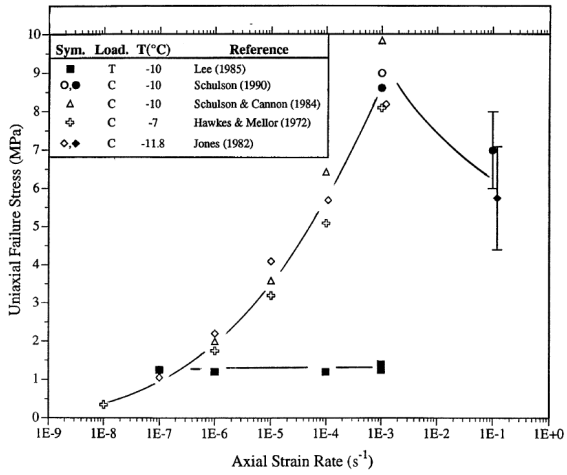

Figure 2.13: Uniaxial failure stress measured at varying strain-ratesSchulson and Duval (2009)

The discussion on strain-rate softening limits the physical approach of the mechanical behavior of ice. As the reader will notice in the next chapter, the decrease in ice strength for brittle behavior is an important property during the interaction between ice and structures. Since there is no unanimous physical explanation for this behavior, the approach in the following chapters will be from a phenomenological perspective. Although links with physical properties do appear, they cannot be proven at this point. The used parameters will be purely related to the phenomena that are observed in laboratories and the field.

2.4. Chapter summary

To understand the phenomena modeled in this thesis, the reader requires some basic knowledge on the properties of sea ice. Ice has a hexagonal crystal structure which enables it to float on rivers and on seas. The crystals are anisotropic and grow faster in one direction compared to the other. Together with environmental factors this results in a complex, porous ice sheet.

The strength of the ice sheet is larger close to the surface and varies in direction. The

compressive strength of ice even varies with rate at which the ice is deformed, know as the strain rate.

- At low strain rates ice behaves in a ductile manner, meaning that the ice will eventually fail by vsco-plastic deformation. As the strain rate increases, the stress at which ductile failure occurs increases as well.
- At higher strain rates the ice behaves in a brittle manner, meaning that the ice will fail by fracturing.
- The transition from ductile to brittle behavior occurs smoothly due to the formation of micro cracks. The highest velocity at which ductile behavior occurs is referred to as the transition velocity.

The stress at which brittle failure occurs seems to decrease with increasing strain rate. However, since this is debated in literature, a phenomenological approach is used in the following chapters.

The concepts in this chapter are considered as the physical concepts:

- Behavior
  - Deformation
    - Elastic deformation
    - Viscous deformation
    - Plastic deformation
  - Failure
    - Ductile failure
    - Brittle failure

Chapter 3
Dynamic ice-structure interaction

The focus of this chapter is on the behavior of an actual ice sheet as it interacts with a structure. Phenomena observed in small-scale measurements will be used to clarify some of the phenomena observed during full-scale experiments. However, these explanations have not been proven yet, henze a phenomenological approach is used to model the phenomena.

First, a description is given on some of the most important failure behavior observed during the interaction with rigid structures. The phenomena are referred to as 'failure modes' and described in section 3.1. Next, an elaboration is given on the failure phenomena observed for compliant structures in section 3.2. These are referred to as ice-induced vibrations (IIV). Finally, in section 3.3 an overview is given of the phenomenological models that are used in industry concluding with the concept behind the model by Hendrikse and Metrikine, used later in this thesis.

3.1. Failure modes during interaction with a rigid structure

The most important phenomena that have been observed during ice-structure interaction are the failure modes. In this section failure against a rigid structure is considered. Starting with creep failure for ice velocities below the transition velocity, followed by crushing failure for higher ice velocities. Finally, a description of buckling failure is given. The section is concluded with an overview of the failure modes.

3.1.1. Creep

When observing creep failure while holding the fast forward button of your video player, one would see the ice flowing plastically around the structure. A schematic representation is given in Figure 3.1. The ice sheet will be in full contact with the structure over the

complete ice thickness and structure width. In a physical sense creep is related to ductile failure as discussed in section 2.3.

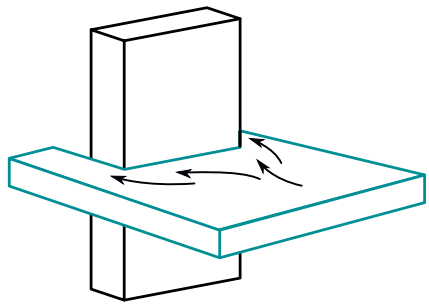

Figure 3.1: Schematic representation of creep failure

Despite the observations of micro cracks, creep is considered as pure ductile failure under compression. It only occurs at relatively low ice velocities and has the characteristics of ductile behavior. The latter meaning that deformation requires time to develop and that the global ice load will increase for higher ice velocities.

The maximum velocity at which creep occurs is called the transition velocity and is estimated at 1 mm/s for saline ice (Schulson and Duval, 2009). It resembles the velocity at which the transition from ductile failure to brittle failure occurs. In the vicinity of this velocity, also the maximum global ice load is expected. This is however only in the case of low aspect ratios, since buckling is expected otherwise. Here, the aspect ratio is defined by b/h. Where b is the structure width and h is the ice thickness. In practice for sea-ice, creep mainly occurs for ice with decreasing velocity or during thermal expansion.

3.1.2. Crushing failure

When an ice sheet is pushed against a structure at velocities higher than the transition velocity the ice will not fail in a flowing ductile manner. The load rises until a maximum and drops suddenly. It will fail in a jerky manner while fragments of many sizes are ejected from the contact zone. The ice in front of the structure will be pulverized to small particles typically 0.5-2.0 cm in size (Timco, 1991).

The relation between global ice load and ice velocity here is different than for creep. Where the global ice load will increase with the ice velocity during creep, it will decrease during crushing. Furthermore, the violent failure of the ice during crushing results in a rough ice edge, which is not in full contact with the structure. Together with the pulverizing crushing failure, spalling and radial cracking can occur. The latter two will be described next.

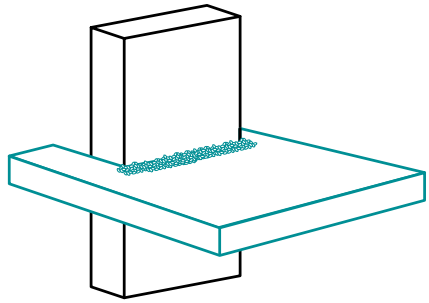

Figure 3.2: Schematic representation of crushing failure

Spalling

As discussed, during crushing failure the ice sheet thickness is not in full contact with the structure. Next to pulvarization, large pieces of ice will cleave from the ice sheet in vertical direction as illustrated in Figure 3.3. This failure mode is called spalling and results in the extrusion of disc shaped plates at the top and bottom of the ice sheet. They are formed by out-of-plane tensile and shear failure across the columnar ice. Experiments show that spalling occurs for aspect ratios $b/h \leq 3$. Schulson and Duval (2009) explain that this is related to the confinement of the ice. However, this is outside of the scope of this thesis. Spalling is considered as a brittle failure mode and happens at all ice velocities where crushing occurs as well.

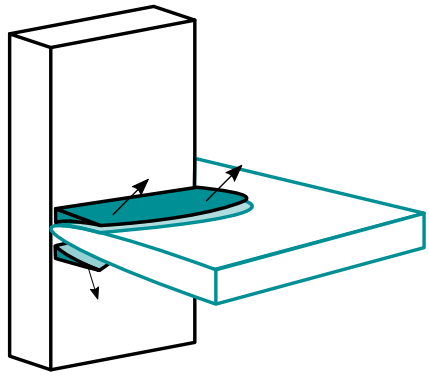

Figure 3.3: Schematic representation of spalling failure

Radial cracks

Radial cracks form ahead of the structure with a length of a few structure widths. They are caused by in-plane tensile and shear failure and therefore are formed in the direction of

the loading. This means that for flat structures the cracks form in the direction of the ice velocity, and for cylindrical structures the cracks will form normal to the structure's outer diameter. If a free boundary is nearby, the crack will propagate to that boundary, reducing the ice load.

Radial cracking occurs simultaneously to ice crushing, and like spalling, for all velocities where ice crushing occurs. However, experiments have shown that radial cracks occur at relatively higher aspect ratios, for the same confinement reasons as discussed for spalling.

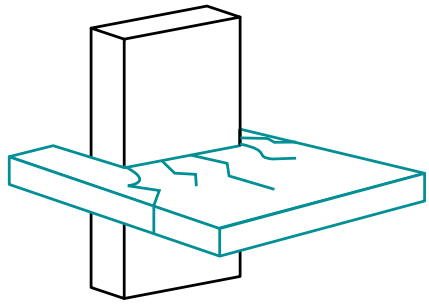

Figure 3.4: Schematic representation of the formation of radial cracks

3.1.3. Buckling failure

Buckling failure is defined by out-of-plane bending failure as a result of the compressive stress. Compressive stress reduces the flexural rigidity of the ice sheet until it approaches zero and the ice sheet becomes unstable. As the flexural rigidity of the ice sheet scales with h^3, buckling failure is limited to relatively high aspect ratio's. When the ice sheet deforms by buckling, it will ultimately fail with a circumferential crack at the location where the flexural strength is exceeded as illustrated in Figure 3.5.

The observant reader may have noticed that both buckling failure and the formation of radial cracks occur at relatively high aspect ratios. As a consequence, radial cracks occur during buckling as well. Kerr (1978) suggests that due to the combination of these failure modes, buckling may be described by the compressive loading of a wedge-shaped floating beam supported by a Winkler elastic foundation. Figure 3.6 shows a top view of the wedges formed during the crushing failure mode.

3.1.4. Failure mode map

For convenience reasons the above described failure modes are reduced to four separate categories:

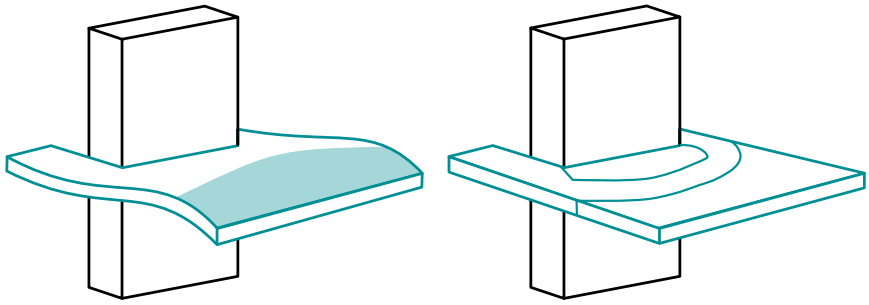

(a) Buckling **(b)** Formation of circumferential cracks

Figure 3.5: Schematic representation of buckling failure

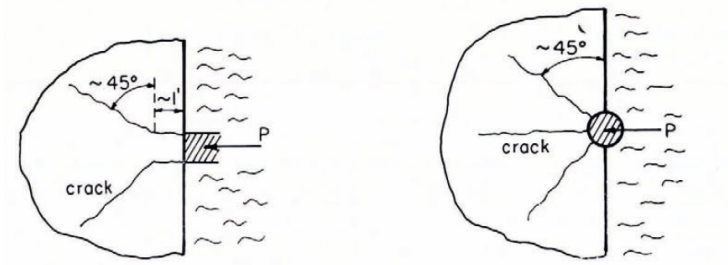

Figure 3.6: Top view of wedges formed due to the formation of radial cracks Kerr (1978)

- Creep failure
- Crushing failure
- Mixed buckling-crushing failure
- Buckling failure

Timco (1991) conducted a large number of laboratory experiments to determine the relation between the failure mode and the ice thickness, structure width, and ice velocity. He created a graph which is referred to as the 'failure mode map' and depicted in Figure 3.7. The experiments were done for fresh-water ice on a small scale. However, based on studies by among others Sodhi (1998) it is believed that Timco's map applies qualitatively to large scale sea water ice as well. Therefore, this map will be used to verify the phenomenological model used in this thesis in a qualitative sense. Figure 3.7 shows a clear deviation between the failure modes. If one would look at Timco's failure map for a single structure width, the following could be concluded:

1. Ductile failure (creep) occurs below the transition velocity.

2. Buckling occurs at intermediate ice velocities and small ice thicknesses.
3. Mixed buckling-crushing occurs as a transition between pure buckling and crushing.
4. Crushing occurs at ice velocities above the transition velocity and for relatively large ice thicknesses

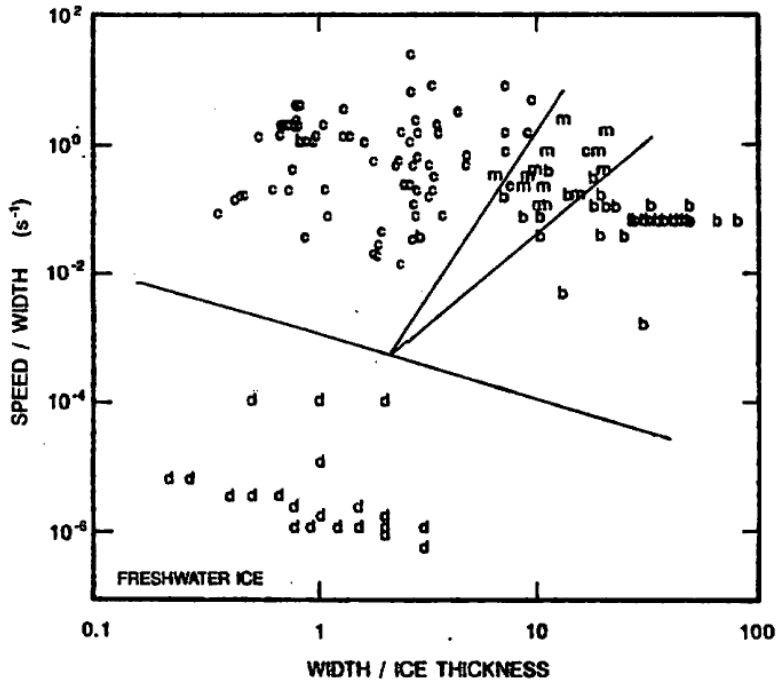

Figure 3.7: Failure mode map based on laboratory experiments on fresh-water ice. In this map b = buckling; c = crushing; d = creep (ductile failure); and m = mixed buckling-crushing. Timco (1991)

3.2. Ice-induced vibrations

Where the previous section only considered rigid structures, this section considers the dynamic phenomena that occur during interaction with compliant structures. Full-scale measurements, e.g. in the Bohai Sea, show three distinctive types of ice-induced vibrations occurring during crushing. These types are referred to as intermittent crushing, frequency lock-in (FLI), and continuous brittle crushing.

The definitions for these 'crushing regimes' vary throughout literature and therefore the definitions used in this thesis are given here.

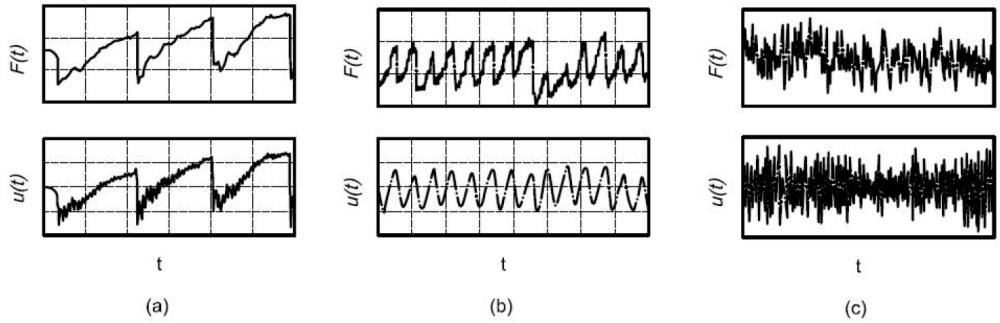

Figure 3.8: Typical IIV regimes load signals (top), and structural displacement signals (bottom). From left to right: Intermittent crushing, frequency lock-in, and continuous brittle crushing ISO 19906 (2010)

Intermittent crushing

Intermittent crushing, as shown in Figure 3.8 (a), occurs at relatively low ice velocities. It consists of a loading and an unloading phase. During the loading phase, ductile behavior occurs since the relative velocity is below the transition velocity. Here, the relative velocity is the difference between the velocity of the structure and the ice velocity. At low relative velocity the global ice load gradually increases until maximum deflection is reached and the unloading phase starts. During the unloading phase, the structure moves in the opposite direction of the ice velocity, in brittle crushing failure. After maximum deflection in the direction opposite to the ice velocity is reached, relaxation vibrations follow in the structure's natural frequency. As the vibrations decay originating from damping in the structure and interaction with the ice, a new loading phase starts.

Frequency lock-in

Frequency lock-in, as shown in Figure 3.8 (b), can occur at intermediate ice crushing velocities. During a full cycle, the structure is loaded in ductile behavior at a low relative velocity. During this period of loading, enough energy is transferred to the structure to accelerate it to a velocity higher than the ice velocity i.e. the relative velocity becomes negative. This results in elastic relaxation in the ice or even loss of contact. As the structure approaches its maximum deflection, the relative velocity increases and an unloading phase follows. During the unloading phase, the structure moves in the opposite direction of the ice velocity in brittle failure and at high relative velocity. The relative velocity will decrease, and after the structure reached maximum deflection on the other side, a new ductile loading phase

starts. The frequency of this cycle occurs near one of the lower natural frequencies of the structure.

Continuous brittle crushing

Continuous brittle crushing, as shown in Figure 3.8 (c), occurs at relatively high ice velocities. Since the relative velocity is continuously high, no ductile behavior occurs. The loading can be considered as aperiodic, resulting in an aperiodic structural response.

3.3. Phenomenological models

Models for ice-induced vibration exist since first ice-structure interaction with oil platforms was encountered in the 1960s. As the physical meaning of ice behavior not yet is well understood, phenomenological models are used to reproduce and predict the IIV regimes. A wide variety of models exists in industry ranging from simplistic loading patterns to sophisticated coupled models.

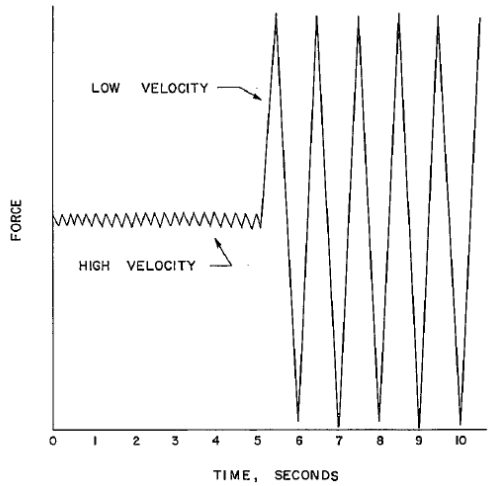

Figure 3.9: Schematic representation of the phenomena observed by Peyton at Cook InletPeyton (1968)

In the early days of IIV research Peyton (1968) performed measurements on vertical test piles in Cook Inlet. Figure 3.9 shows a schematic representation of his findings implying two main phenomena; for decreasing ice velocities during crushing failure:

1. The amplitude of the load increases
2. The loading frequency decreases

These two phenomena from the bases for many phenomenological models, of which some examples are discussed next.

3.3.1. Models based on failure frequency

Matlock et al. (1969) presents a model that includes one of these phenomena by loading a structure in a distinct frequency, while using the maximum load as the amplitude. By increasing the frequency for higher ice velocities, an attempt was made to cover the phenomena described by Peyton. Furthermore, resonance behavior, occurs if the frequency approaches the natural frequency of the structure. Matlock's model results in a saw-tooth shaped load signal which is a method that is still used in current practice. The proposed method to compute structural response for FLI behavior in the international standards code for arctic offshore structures, ISO19906, uses this saw-tooth pattern as well ISO 19906 (2010). It must be emphasized that while this method is widely applied, the ISO method can be considered as a simplified version of Matlock's model and does not include any nonlinear or coupled behavior observed in the field.

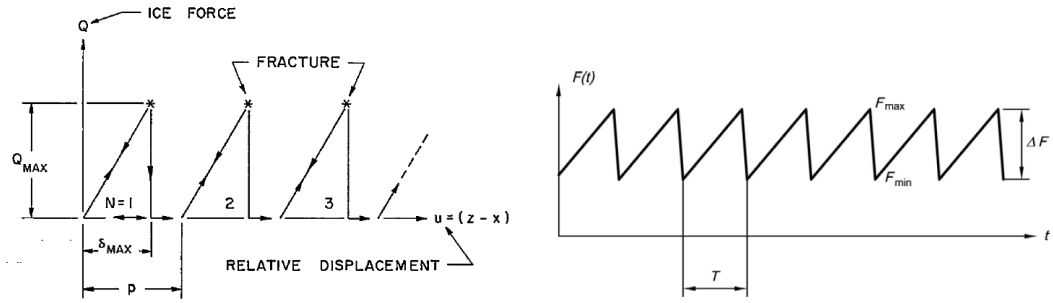

(a) Approach by Matlock et al. (1969) **(b)** Approach from ISO 19906 (2010)

Figure 3.10: Models to predict FLI based on failure frequency

3.3.2. Models including negative ice load gradient

Based on the same measurements done by Peyton (1968), Blenkarn (1970) created a model based on a negative gradient in the compressive strength with increasing loading rate (Figure 3.11). This gradient implies that a the relation exists between ice strength and loading rate. The curve shows that it is negative and nonlinear.

In the physical reasoning behind this relation, references are made to the observed negative gradient in uni-axial compressive strength with increasing strain rate, during small-scale experiments (Michel and Toussaint, 2000). The relation between compressive strength and strain rate was discussed in subsection 2.3.3 and is considered as debated in literature.

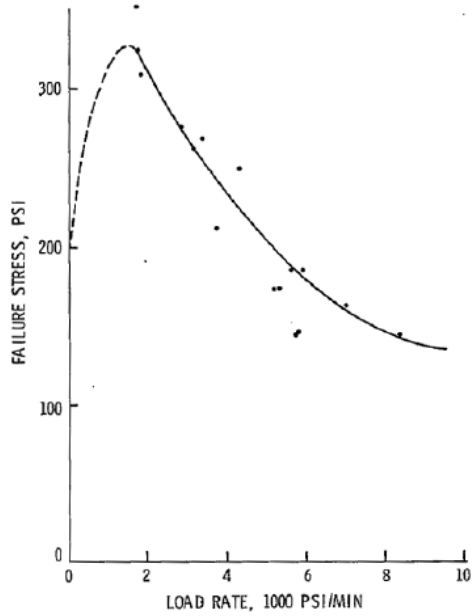

Figure 3.11: Negative gradient in ice strength observed by PeytonBlenkarn (1970)

The curve shown in Figure 3.11 is a result of measurements on global ice load over varying ice velocities. The gradient can therefore also be interpreted as a decrease in ice load over increasing relative velocity. The latter results in a negative damping effect which is the backbone in many models that are currently used to explain intermittent crushing and FLI behavior. E.g. Määttänen (1978) bases his model on a polynomial fit of the curve described in Figure 3.11. Moreover, Huang and Liu (2009) extended Matlock's model with this nonlinear relation defined as two separate power laws divided by the transition velocity.

Karna et al. (1999) introduced a model based on a linearized version of the gradient and introduced stochastic parameters to match full-scale measurements. An important characteristic of Karna's model is that the velocities at which the gradient occurs can be adjusted to obtain good predictions for structures with different degrees of compliance. This makes the ice properties dependent on the structure, which is believed to be a nonphysical consequence of the model assumptions.

3.3.3. Simultaneous and non-simultaneous failure

Originationg from the irregularity of the ice edge, as a results of the violent crushing failure, the global ice load is defined by the sum of local force components Takeuchi and Sakai

(2001). These local forces correspond to the parts of the ice that are in contact with the structure as illustrated in Figure 3.12.

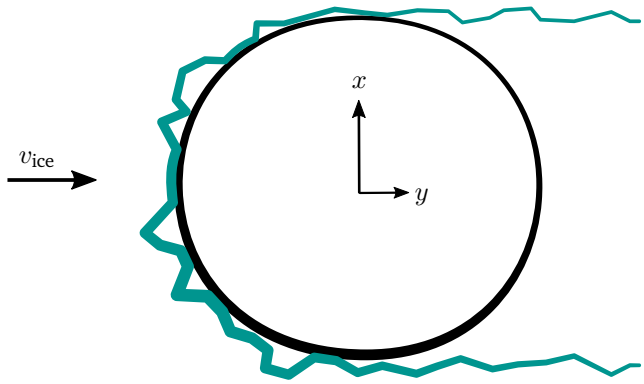

Figure 3.12: Schematic representation of how the ice is in contact with the structure only locally during brittle failure. The structure is drawn in top view and the ice edges is drawn in green.

(Karna et al., 1999) modeled these contact zones by dividing the ice sheet in a certain number of elements over the width of the structure. The elements do not correspond to the actual contact zones. However, they capture the statistics of simultaneous and non-simultaneous failure phenomena which are defined as follows:

- Simultaneous failure is the failure of all ice in contact with the structure at the same time. This occurs when a high correlation between the local loads exists, also referred to as synchronization. Synchronization occurs at low relative velocities, typically when ice fails in a ductile manner.

- Non-simultaneous failure is the random local failure of specific zones in contact with the structure. It occurs at high relative velocities and is characterized by its random global ice load.

Despite it's nonphysical characteristics, Karna's model is considered as one of the most advanced models currently available in industry. As discussed in chapter 1, the sensitivity of it's parameters raise questions on the reliability of it's application at Siemens. Therefore, in this thesis a recently published phenomenological model by Hendrikse and Metrikine (2015a), is used to model the dynamic ice-structure interaction. The most important difference with Karna's model is that the ice parameters are not depending on the structural properties. The ice parameters can be determined from reference measurements and scaled to the interaction area. The basic principles of this model are discussed next.

3.3.4. Variation of contact area

Experiments with pressure sensors at the ice-structure interface have shown a relation between the contact area and the global ice load. This variation of contact area forms the basis of the phenomenological model used in this thesis. Experiments done by Takeuchi and Sakai (2001) show the behavior of contact area variation for three regimes of ice-structure interaction on rigid structures. The regimes are defined as the ductile regime, transitional regime, and brittle regime, not to be confused with the IIV regimes as defined in section 3.2.

- At low velocities, i.e. in **the ductile regime**, the ice pressure is distributed over the full width of the structure.
- At intermediate velocities, i.e. in the **transitional regime** between ductile and brittle, the contact area decreases. Spalling forms the ice edge into a wedge, forming a line-like contact area (Jordaan, 2000). In this contact area high pressure zones occur as illustrated in Figure 3.13.
- Takeuchi and Sakai (2001) show that at high ice velocities, i.e. in **the brittle regime**, contact area decreases even further. For these velocities the majority of the ice load originates from high pressure zones.

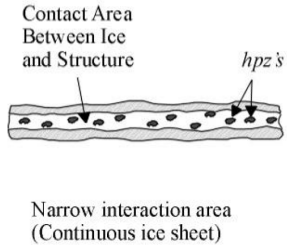

Figure 3.13: Schematic representation of high pressure zones (hpz's) at a line-like contact area of a spalled ice edge Jordaan (2000)

Hendrikse and Metrikine (2015a) explain these phenomena with the occurrence of ductile behavior in the ductile and transitional regime. In a physical sense, it is suggested that the ductile behavior originates from the formation of micro-cracks. The ductile behavior delays local brittle failure, consequently allowing for more ice to reach the structure. Subsequently, the contact area increases and hence the ice load increases as well.

To demonstrate the effect of variation of contact area on a compliant structure, Hendrikse and Metrikine (2015b) performed forced vibration experiments at the HSVA model ice basin in Hamburg. An oscillating indentor, equipped with a tactile sensor, was moved

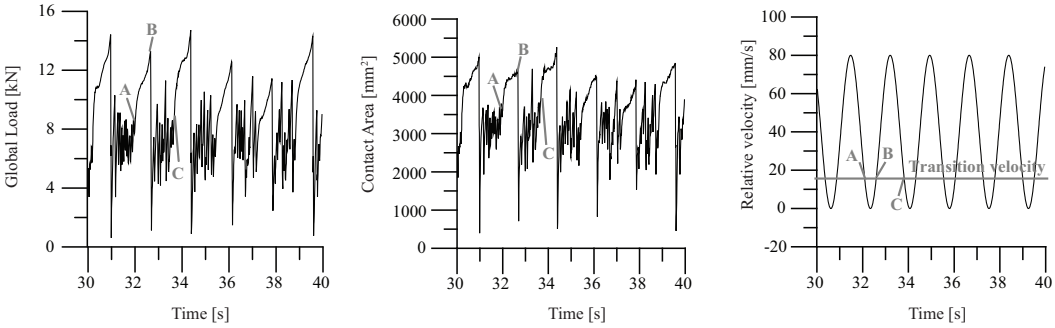

Figure 3.14: Variation of contact area during a forced vibration experiment (Hendrikse and Metrikine, 2015a)

through an ice sheet with a constant ice velocity. Figure 3.14 shows a comparison between the global ice load, contact area, and relative velocity, which were measured during the forced vibration experiment. Between points 'A' and 'B' ductile behavior occurs, since the relative velocity is below the transition velocity. Snapshots of the pressure distribution are given in Figure 3.15. The snapshots demonstrate that the contact area has increased during ductile behavior. Furthermore, in 'A' the main contribution to the global ice load seems to originate from local high pressure zones, while in 'B' the pressure seems to be more equally distributed.

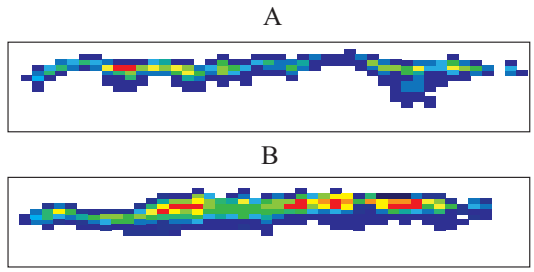

Figure 3.15: Contact pressure measured at time instance 'A' and 'B', as shown in Figure 3.14 (Hendrikse and Metrikine, 2015a)

Hendrikse and Metrikine (2015a) suggest that the increase in global load, that is observed at low relative velocity, can be explained by the increase in contact area. The increase in contact area is the result of a delay in local brittle failure, which in its turn is caused by plastic deformation. The increase in global ice load, with decreasing relative velocity, is the governing phenomenon behind ice-induced vibrations. Hence, the ice needs time to deform in a ductile manner, for IIV to occur. This could explain why frequency lock-in is almost never observed at high frequencies.

3.4. Chapter summary

A phenomenological approach was used to describe dynamic ice-structure interaction. The phenomena are related to the aspect ratio b/h and the ice velocity v_{ice}. For relatively small aspect ratios, and ice velocities below the transition velocity, a failure mode called 'creep' occurs. Creep is related to ductile failure.

For equal aspect ratios and ice velocities above the transition velocity, 'crushing' occurs and is related to brittle failure. Furthermore, for relatively large aspect ratios buckling is the governing failure mode. The crushing failure mode is accompanied by spalling and the formation of radial cracks. Moreover, buckling and crushing can occur at the same ice velocity. The latter results radial cracks dividing the ice sheet into a floating wedge.

During the interaction between ice and a compliant structure, three ice-induced vibration regimes occur: Intermittent crushing at low ice velocities, frequency lock-in at intermediate ice velocities, and continuous brittle crushing at high ice velocities.

The IIV are often modeled in a phenomenological manner since the physics behind the phenomena are not well understood. A recently published phenomenological model by Hendrikse and Metrikine (2015a) is based on the variation of contact area at the interaction surface between the ice and the structure. The contact area is statistically modeled by a certain number of ice elements which have the ability to deform plastically, as well as in in a elastic manner.

The concepts in this chapter are considered as the phenomenological concepts:

- Failure modes
  - Creep
  - Crushing
  - Spalling
  - Radial cracking
  - Buckling
- IIV regimes
  - Intermittent crushing
  - Frequency lock-in
  - Continuous brittle crushing
- Failure regimes
  - Ductile regime
  - Transitional regime
  - Brittle regime

Chapter 4
Phenomenological model for dynamice ice-structure interaction

The previous chapter elaborates on the phenomena observed during full-scale ice-structure interaction. The concepts behind phenomenological models to predict and replicate these phenomena were explained. In this chapter a phenomenological model proposed by Hendrikse and Metrikine (2015a) is implemented and extended to include all four categories of failure modes as discussed in subsection 3.1.4, i.e. creep, crushing, mixed crushing and buckling and pure buckling. Furthermore, all three IIV crushing regimes are included; intermittent crushing, frequency lock-in, and continuous brittle crushing.

The chapter starts in section 4.1 with an explanation of the kinematic element that is used to capture creep and crushing behavior, including IIV. The kinematic element proposed by Hendrikse and Metrikine (2015a) is explained first, followed by extensions to cover the creep failure mode. Thereafter, the definitions of the input parameters are given in section 4.2 and the extension to model buckling behavior is explained in section 4.3.

4.1. Modeling creep and crushing

To describe the phenomena of intermittent crushing, frequency lock-in, and continuous brittle crushing a model proposed by Hendrikse and Metrikine (2015a) is used. The model is constructed out of N kinematic elements to simulate the stochastic effect of contact area variation. Each element represents the elastic-visco-plastic behavior of ice. This inelastic behavior is used to model the increase of contact area as discussed before.

This section contains a detailed description of the kinematic element. First, the element capable of describing crushing is explained, henceforth denoted as the crushing element. Thereafter an extension is made to a kinematic element that is capable of describing crushing and creep, henceforth denoted as the creep-crushing element. The implementation of

the element is discussed and applied to a rigid structure. Finally, a compliant structure is used and the phenomenon of contact variation is included.

4.1.1. The crushing element

At relatively high velocities, ice is observed to fail in brittle crushing as discussed in section 3.1. This failure mode is related to pure elastic behavior and therefore modeled by a spring. At lower ice velocities also inelastic deformation occurs. In the transitional regime, the behavior of ice seems to be elastic-visco-plastic. The left hand side of the element in Figure 4.1 describes the elastic-visco-plastic properties and the right hand side corresponds to the pure elastic properties.

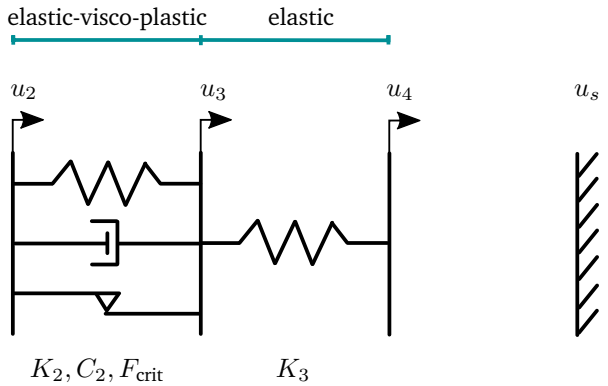

Figure 4.1: Degrees of freedom of the crushing element

As described in section 3.3, the inelastic behavior is related to the formation of micro-cracks and thus requires a certain activation stress. Therefore, a certain load should be required to activate the elastic-visco-plastic deformation in the element. To model both conditions, the element is constructed from the following components.

The inelastic part contains a spring with stiffness K_2, a dashpot with coefficient C_2, and a dry-friction element with critical activation force F_{crit}. Due to this dry-friction element, the mechanism can either be in 'stick' or in 'slip'. Both situations are related to their own equation of motion. Furthermore, the elastic part consists of a single spring with stiffness K_3, defining the stiffness of the crushing element during 'stick'. Taking into account the above, the behavior of the element can be represented by the following equations of motion:

$$u_2(t) = v_{ice} \cdot t \tag{4.1}$$

$$\dot{u}_3(t) = \begin{cases} v_{\text{ice}} & \text{stick} \\ v_{\text{ice}} + \frac{K_3}{C_2}(u_4 - u_3) - \frac{K_2}{C_2}(u_3 - u_2) - \frac{F_{\text{crit}}}{C_2} & \text{slip} \end{cases} \tag{4.2}$$

$$u_4(t) = \begin{cases} u_3 & \text{no contact} \\ u_s & \text{contact} \end{cases} \tag{4.3}$$

Where u_2, u_3, and u_4 are the displacements of the element, and u_s is the displacement of the structure (zero for the rigid structure in Figure 4.1). The element is set to fail when a maximum internal load $K_3 \cdot \delta_{\text{crit}}$ is reached. This failure load is related to the terminal failure stress mentioned in section 2.3. Hence, the internal load in the spring with stiffness K_3 is limited by the critical displacement δ_{crit}.

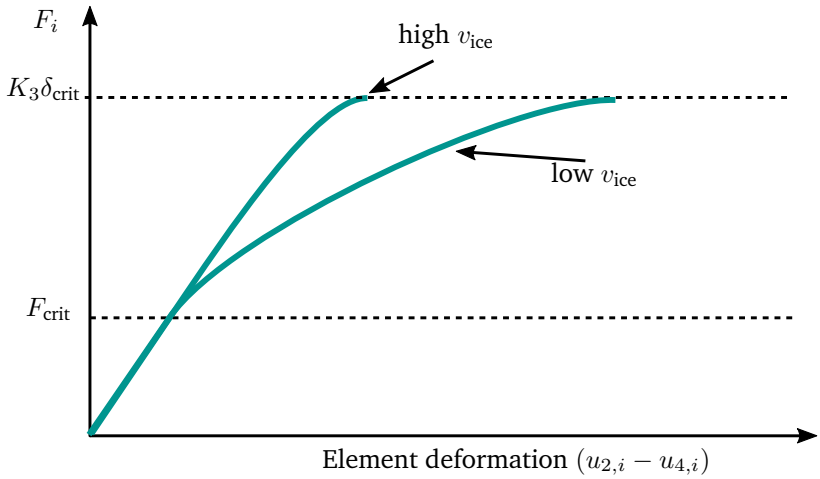

Figure 4.2: Load-deformation curve of the kinematic element behavior

Due to the elastic-visco-plastic part of the crushing element, it's behavior depends on the ice velocity $\dot{u}_2 = v_{\text{ice}}$. For relatively high ice velocities the element will behave mainly elastic, since inelastic deformation has no time to develop. Slip occurs, however for only a very short time. For relatively lower velocities the element behaves elastic until the critical slip load F_{crit} is reached. From instance in time, the element behaves elastic-visco-plastic as shown in Figure 4.2.

4.1.2. The creep-crushing element

The crushing element is capable of describing the phenomena of intermittent crushing, frequency lock-in, and continuous brittle crushing. However, to describe the complete ice

velocity spectrum ,also creep failure should be included. This extension is performed by adding a dashpot in series with the crushing element. The dashpot will introduce a viscosity that will limit the element from reaching it's failure load below a certain ice velocity. This velocity is chosen to be the transition velocity and depicts the transition from ductile to transitional behavior.

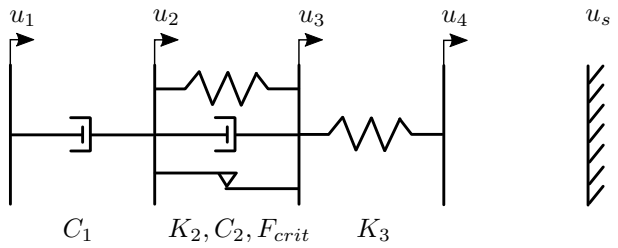

Figure 4.3: Degrees of freedom of the creep-crushing element

The behavior of the creep-crushing element is illustrated in Figure 4.4. The coefficient C_1 is chosen such that at high ice velocities the behavior of the element can be considered as elastic. At intermediate velocities the element will behave elastic-visco-plastic. Below the transition velocity the behavior can be divided in two parts: For the relatively high velocities below the transition velocity, the element will behave elastic, then elastic-visco-plastic and finally remain viscous. At relatively low velocities below the transition speed, the element will behave elastic, and then stay viscous.

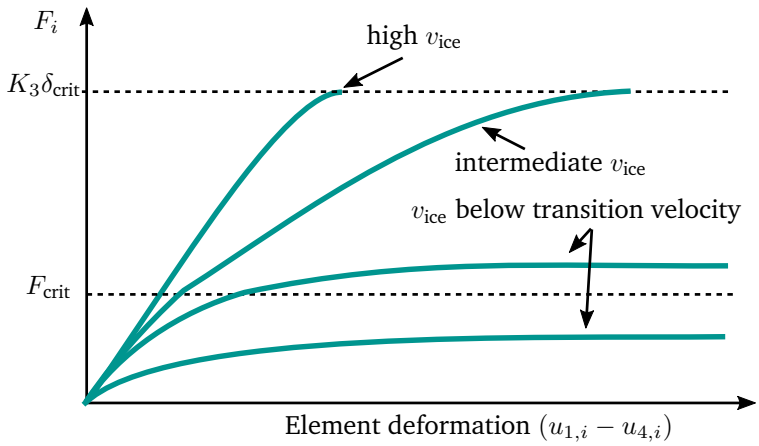

Figure 4.4: Load-deformation curve of the creep-crushing element behavior

The equations of motion now become:

$$u_1(t) = v_{\text{ice}} \cdot t \tag{4.4}$$

$$\dot{u}_2(t) = \begin{cases} v_{\text{ice}} & \text{no contact} \\ v_{\text{ice}} + \frac{K_3}{C_1}(u_4 - u_3) & \text{contact} \end{cases} \tag{4.5}$$

$$\dot{u}_3(t) = \begin{cases} v_{\text{ice}} & \text{no contact} \\ v_{\text{ice}} + \frac{K_3}{C_1}(u_4 - u_3) & \text{contact-stick} \\ v_{\text{ice}} + \frac{K_3}{C_1}(u_4 - u_3) + \frac{K_3}{C_2}(u_4 - u_3) - \frac{K_2}{C_2}(u_3 - u_2) - \frac{F_{\text{crit}}}{C_2} & \text{contact-slip} \end{cases} \tag{4.6}$$

$$u_4(t) = \begin{cases} u_3 & \text{no contact} \\ u_s & \text{contact} \end{cases} \tag{4.7}$$

The element is given an initial condition where the distance to the structure is defined by a uniform distribution $U(0, r_{\text{max}})$. Where r_{max} is the maximum offset in meters. Furthermore, the back end of the element u_1 is given a constant velocity equal to the ice velocity $\dot{u}_1 = v_{\text{ice}}$.

4.1.3. Discontinuities

The above results in the introduction of the following discontinuities to the equations of motion:

1. Switching between contact and no contact, between ice and structure
2. Switching between stick and slip
3. Failure of the element

To create a phenomenological model of the ice crushing phenomena, these discontinuities should be included in the model. For computational reasons it was chosen to use a monolithic system of equations to describe the ice-structure interaction. To enable this approach the model is by described by its equilibrium equations. These equations can be used in numerical solvers to find a solution where the equilibrium is satisfied. This results in the following:

$$\boldsymbol{M}\ddot{\boldsymbol{u}}(t) + \boldsymbol{C}\dot{\boldsymbol{u}}(t) + \boldsymbol{K}\boldsymbol{u}(t) = \boldsymbol{g}(t) \tag{4.8}$$

Where $\boldsymbol{M}$ is the mass matrix, $\boldsymbol{C}$ is the damping matrix, $\boldsymbol{K}$ is the stiffness matrix of the complete system of equations. Furthermore, $\boldsymbol{g}(t)$ is the external load vector. As shown in equations 4.4 to 4.7 the kinematic element can exist in three different states. It can either not be in contact, in contact and in stick, or in contact and in slip. This gives three systems of equations. To reduce this number of systems to 1, the discontinuities were tackled in the following ways.

Contact

To model the switch between contact and no contact, the displacement $u_{i,4}$ is equal to the displacement of the structure as illustrated in Figure 4.5. Furthermore, a nonlinear stiffness $K_3(u_3, u_s)$ is introduced, where the stiffness is zero when the ice element is not in contact with the structure.

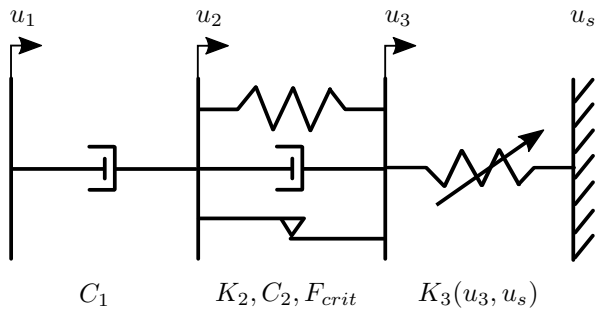

Figure 4.5: The creep-crushing element for a monolithic approach

Furthermore, a definition for contact and no contact should be defined. Since the ice can only exert a force to the structure if it actually is in contact with the structure, the spring K_3 is defined by the relative displacement between the ice and the structure $u_s - u_3$:

$$K_{3,i} = \begin{cases} 0 & (u_s - u_3) > 0 \\ K_3 & (u_s - u_3) \leq 0 \end{cases} \tag{4.9}$$

This makes the stiffness $K_{3,i}$ of element i continuous to the zeroth order, however non-linear. A plot of the force in the spring with stiffness $K_{3,i}$ to the relative displacement $u_s - u_3$ is shown in figure Figure 4.6.

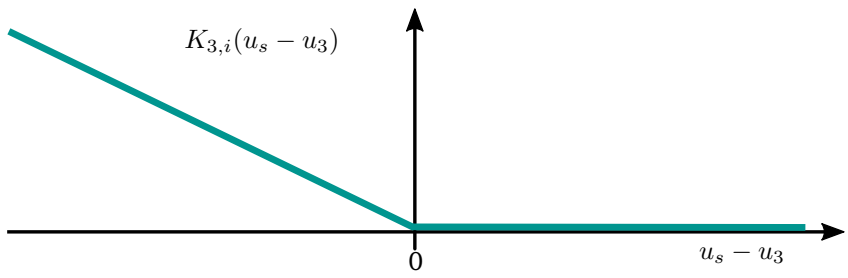

Figure 4.6

The observant reader might notice that the derivative of the force is still discontinuous. Since a Newton-Raphson scheme is used to solve the non-linear problem, this might result

in a non converging solution. However, since the transition occurs at a relative displacement of $u_s - u_3 = 0$, the force in the spring will be zero for both $K_{3,i} = K_3$ and $K_{3,i} = 0$. Hence, the transition occurs smoothly.

Stick-slip

When the element is in contact with the structure, the dry-friction element has the property of being either in stick or in slip. To model the dry-friction element in a single equation of motion, the friction force in the element is defined as F_{fric}. If the element is not activated, the friction force may vary between 0 and a threshold force at which the element starts sliding, i.e. slip occurs. When it slips, the friction force is assumed equal to the threshold force, denoted as the critical friction force F_{crit}. Here, the critical friction force F_{crit} is an input parameter of the model. To find the friction force the equilibrium in the node with displacement u_3 is used:

$$K_2(u_3 - u_2) + C_2(\dot{u}_3 - \dot{u}_2) + F_{\text{fric}} = K_3(u_s - u_3) \tag{4.10}$$

During slip, the friction force is equal to the critical force. When the element sticks, the relative velocity between u_2 and u_3 is equal to zero. As a consequence during stick mode:

$$\dot{u}_3 - \dot{u}_2 = 0 \tag{4.11}$$

The force in the dashpot with coefficient C_2 must be equal to zero as well, i.e.:

$$C_2(\dot{u}_3 - \dot{u}_2) = 0 \tag{4.12}$$

Consequently from Equation 4.12 it is found that the friction force during slip can be found by evaluating the equilibrium in the node with displacement u_3 as:

$$F_{\text{fric}} = K_3(u_s - u_3) - K_2(u_3 - u_2) \quad \text{slip} \tag{4.13}$$

Therefore, it can be concluded that the force in the dry-friction element can be found as follows:

$$F_{\text{fric}} = \begin{cases} K_3(u_s - u_3) - K_2(u_3 - u_2) & \text{slip} \\ F_{\text{crit}} & \text{stick} \end{cases} \tag{4.14}$$

Appendix B elaborates on determination of the occurrance of stick and slip. The conclusion of this appendix is given here.

$$\begin{array}{rl} \text{stick occurs if:} & K_3(u_s - u_3) - K_2(u_3 - u_2) \leq F_{\text{crit}} \\ \text{slip occurs if:} & K_3(u_s - u_3) - K_2(u_3 - u_2) > F_{\text{crit}} \end{array} \tag{4.15}$$

Failure of the element

During brittle failure of ice, a piece breaks off and is ejected out of the contact zone. This results in a load drop and loss of contact at the location of failure. The failure of an element is modeled as an event during a single step in time in the simulation. As discussed earlier in this section, the kinetic element is set to fail when a maximum internal load $K_3 \cdot \delta_{\text{crit}}$ is reached. The loss of contact is modeled by a 'new' element taking the place of the failed element. This new element is simulated by setting the failed element to a new initial position. The new position is defined as a distance from the structural deflection u_s, drawn from a uniform distribution $U(0, r_{\text{max}})$.

4.1.4. Equations of motion

The creep-crushing element is defined such that it can be solved in a monolithic way as shown in Figure 4.5. It can be described by the following equations of motion:

$$C_1(\dot{u}_2 - v_{ice}) = K_2(u_3 - u_2) + C_2(\dot{u}_3 - \dot{u}_2) + F_{\text{fric}} \tag{4.16}$$

$$K_2(u_3 - u_2) + C_2(\dot{u}_3 - \dot{u}_2) + F_{\text{fric}} = K_3(u_s - u_3) \tag{4.17}$$

Where K_3 is a function described by Equation 4.30 and F_{fric} is a function described by Equation 4.15. Equations 4.16 and 4.17 can be rewritten in the form of Equation 4.8 as follows:

$$\begin{bmatrix} C_2 & -C_2 \\ -C_2 & C_1 + C_2 \end{bmatrix} \begin{bmatrix} \dot{u}_3 \\ \dot{u}_2 \end{bmatrix} + \begin{bmatrix} K_2 + K_3 & -K_2 \\ -K_2 & K_2 \end{bmatrix} \begin{bmatrix} u_3 \\ u_2 \end{bmatrix} = \begin{bmatrix} K_3 u_s - F_{\text{fric}} \\ C_1 v_{\text{ice}} + F_{\text{fric}} \end{bmatrix} \tag{4.18}$$

Equation 4.18 will be used throughout the following section and the next chapter to describe the system as it will be extended.

4.1.5. Compliant structures

Next, a closer look is taken at the interaction of the kinematic element with a compliant structure. For simplicity a single element is illustrated next to a single degree of freedom mass-spring-damper system, representing the structure with mass M_s, damping C_s, and stiffness K_s.

The equations of motion of the total system as previously described in Equation 4.18 can now be extended to Equation 4.19.

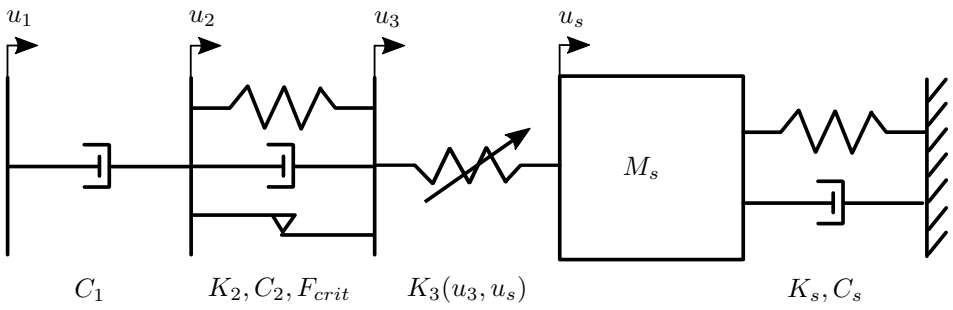

Figure 4.7: The creep-crushing element coupled to a compliant structure

$$\begin{bmatrix} M_s & 0 & 0 \\ 0 & 0 & 0 \\ 0 & 0 & 0 \end{bmatrix} \begin{bmatrix} \ddot{u}_s \\ \ddot{u}_3 \\ \ddot{u}_2 \end{bmatrix} + \begin{bmatrix} C_s & 0 & 0 \\ 0 & C_2 & -C_2 \\ 0 & -C_2 & C_1 + C_2 \end{bmatrix} \begin{bmatrix} \dot{u}_s \\ \dot{u}_3 \\ \dot{u}_2 \end{bmatrix} + \begin{bmatrix} K_s + K_3 & -K_3 & 0 \\ -K_3 & K_2 + K_3 & -K_2 \\ 0 & -K_2 & K_2 \end{bmatrix} \begin{bmatrix} u_s \\ u_3 \\ u_2 \end{bmatrix} = \begin{bmatrix} 0 \\ -F_{\text{fric}} \\ C_1 v_{\text{ice}} + F_{\text{fric}} \end{bmatrix} \tag{4.19}$$

This new system forms the basis of the creep-crushing model. However, the contact area variation effect has not been included yet. This will be discussed next.

4.1.6. Contact area variation

To describe the contact area variation as discussed in section 3.2, multiple elements are used during the simulation. It was not the aim to model the exact contact area between the ice and the structure. However, the main characteristics of the effect; the mean, maximum, and standard deviation of the load, should be captured. The ice sheet is split up into N zones as shown in Figure 4.8.

The N elements are implemented by inserting their degrees of freedom to the system of equations. Figure 4.9 shows an example of a compliant structure in contact with 2 elements. Its system of equations is given in Equation 4.20.

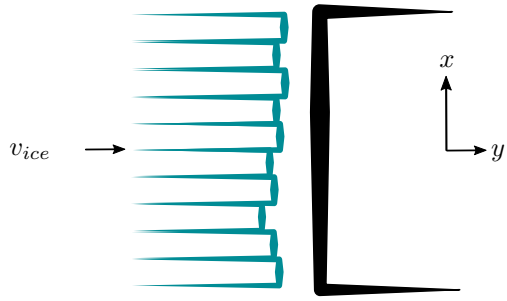

Figure 4.8: Top view of a schematic representation of 10 creep-crushing elements approaching a rectangular structure. Here, the y-direction is the direction of the ice velocity and the x-direction is the lateral direction.

Figure 4.9

$$\begin{bmatrix} M_s & 0 & 0 & 0 & 0 \\ 0 & 0 & 0 & 0 & 0 \\ 0 & 0 & 0 & 0 & 0 \\ 0 & 0 & 0 & 0 & 0 \\ 0 & 0 & 0 & 0 & 0 \end{bmatrix} \begin{bmatrix} \ddot{u}_s \\ \ddot{u}_{3,1} \\ \ddot{u}_{2,1} \\ \ddot{u}_{3,2} \\ \ddot{u}_{2,2} \end{bmatrix} + \begin{bmatrix} C_s & 0 & 0 & 0 & 0 \\ 0 & C_2 & -C_2 & 0 & 0 \\ 0 & -C_2 & C_1+C_2 & 0 & 0 \\ 0 & 0 & 0 & C_2 & -C_2 \\ 0 & 0 & 0 & -C_2 & C_1+C_2 \end{bmatrix} \begin{bmatrix} \dot{u}_s \\ \dot{u}_{3,1} \\ \dot{u}_{2,1} \\ \dot{u}_{3,2} \\ \dot{u}_{2,2} \end{bmatrix} +$$
$$\begin{bmatrix} K_s+K_{3,1}+K_{3,2} & -K_{3,1} & 0 & -K_{3,2} & 0 \\ -K_{3,1} & K_2+K_{3,1} & -K_2 & 0 & 0 \\ 0 & -K_2 & K_2 & 0 & 0 \\ -K_{3,2} & 0 & 0 & K_2+K_{3,2} & -K_2 \\ 0 & 0 & 0 & -K_2 & K_2 \end{bmatrix} \begin{bmatrix} u_s \\ u_{3,1} \\ u_{2,1} \\ u_{3,2} \\ u_{2,2} \end{bmatrix} = \begin{bmatrix} 0 \\ -F_{\text{fric},1} \\ C_1 v_{ice} + F_{\text{fric},1} \\ -F_{fric,2} \\ C_1 v_{\text{ice}} + F_{\text{fric},2} \end{bmatrix} \tag{4.20}$$

Equation 4.20 shows how Equation 4.19 is extended with a second element. This same extension is used to add N creep-crushing elements to the system. It must be emphasized that the elements are not coupled directly. Only an indirect coupling through the structure exists.

4.2. Parameters of the phenomenological model

The creep-crushing elements are defined by the input parameters C_1, K_2, C_2, F_{crit}, K_3, r_{max}, and δ_{crit}. Furthermore, the number of elements N is required. The definition of these parameters has not been published at the time of writing. However, preliminary definitions by Hendrikse (2017) are presented in this section.

Since definition of these parameters from physical properties is not possible yet, they must be derived from relations with already existing measurement data. It is therefore assumed that the deformation and failure behavior of the ice does not change with changes to the structural properties and ice thickness.

The modeled phenomena are highly dependent on the relation between the global ice load and the ice velocity, as was discussed in section 3.3. Therefore, the model parameters can be deducted from reference measurements on certain properties of the curve illustrated in Figure 4.10. The reference data used for the research in this thesis is discussed in section 5.2. The current section solely elaborates on how this data is translated to the input parameters.

4.2.1. Reference parameters

The reference parameters are taken at three distinctive velocities on the curve shown in Figure 4.10. These velocities are the transition velocity v_{trans}, 2 times the transition velocity $2v_{\text{trans}}$, and a reference velocity in the brittle regime v_{ref}.

It must be noted that the reference parameters will be determined for a certain reference ice thickness and reference structure diameter, h_{ref} and $b_{s,ref}$ respectively. Furthermore, the reference data should be chosen such that the aspect ratio $\frac{h_{\text{ref}}}{b_{s,\text{ref}}}$ is low enough to reflect crushing failure and not buckling(see section 3.1).

The maximum global ice load occurs at the transition velocity. As this is an important value to the curve it should be taken as one of the reference parameters and is defined as F_{trans}. At $2 \cdot v_{\text{trans}}$, the mean load defined as F_{2vtrans}, is required to determine the slope of the curve. Here, it is assumed that the transition velocity does not change for different structure diameters b_s and ice thickness h. Finally, the time required to reach maximum loading at the transition velocity is defined as t_{peak}.

At an arbitrary reference velocity in the brittle crushing range, the mean ice load and its standard deviations are required and defined as F_{mean} and F_{std}. At this velocity also the peak frequency f_{peak} has to be determined. An overview of the required reference parameters is given in Table 4.1.

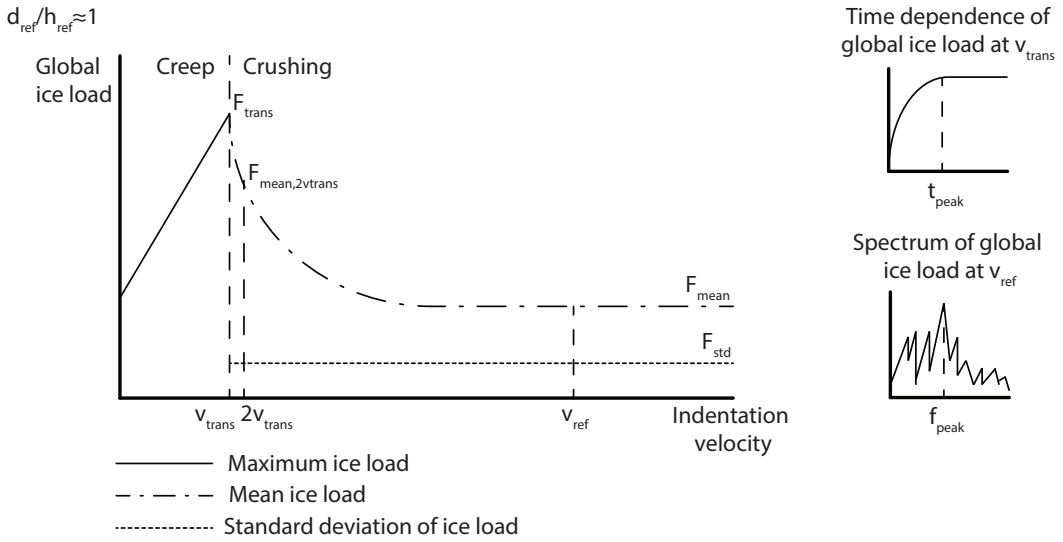

Figure 4.10: Illustration of the input curve containing the reference parameters required to obtain the input parameters (Hendrikse, 2017)

Table 4.1: Overview of reference parameters

Parameter	**Symbol**	**Unit**
Reference structure width	$b_{s,ref}$	m
Reference ice thickness	h_{ref}	m
Transition velocity	v_{trans}	m/s
Maximum load at v_{trans}	F_{trans}	kN
Mean load at $2v_{\text{trans}}$	F_{2vtrans}	kN
Time until maximum load at v_{trans}	t_{peak}	s
Reference velocity in pure brittle regime	v_{ref}	m/s
Mean load at v_{ref}	F_{mean}	kN
Standard deviation of load at v_{ref}	F_{std}	kN
Peak frequency of the load at v_{ref}	f_{peak}	Hz

4.2.2. Input parameters

The input parameters are defined such that the model reproduces the values of the reference parameters. Hence, the curve in Figure 4.10 can be reproduced by simulations with a rigid structure, as will be done later in this thesis to verify the model. In this subsection the input parameters are divided into three categories and will be described separately. An overview of the parameters is given in Table 4.2.

Table 4.2: Overview of input parameters

Parameter	Symbol	Unit
Maximum offset	$r_{\max}$	m
Critical deformation	δ_{crit}	m
Number of reference elements	N_{ref}	#
Number of model elements	N	#
elastic deformation stiffness	K_3	kN/m
creep deformation viscosity	C_1	kNs/m
inelastic deformation activation force	F_{crit}	kN
inelastic deformation stiffness	K_2	kN/m
inelastic deformation viscosity	C_2	kNs/m

First, relations are found for pure elastic failure. Pure elastic failure is expected at high ice velocities, in the brittle crushing regime. It is assumed that at an ice velocity v_{ref}, the solely the elastic part of the creep-crushing elements is contributing to the ice load. The mean global load in the model at v_{ref} is therefore given by the sum of the expected values of individual creep-crushing elements.

$$F_{\text{mean}}(v_{\text{ref}}) = \mathrm{E}[F(v_{\text{ref}})] = N \frac{K_3 \int_0^{t_{\text{fail}}} u_3 \mathrm{d}t}{\frac{\mathrm{E}[r]}{v_{\text{ref}}} + t_{\text{fail}}} \tag{4.21}$$

Where $E[r]$ is the expected value of the initial gap between the ice element and the structure and t_{fail} is the time at which the individual element fails. Since only the elastic part contributes, $u_3(t)$ is linear and given by $t \cdot v_{\text{ref}}$. The standard deviation of the load at an ice velocity of v_{ref} is computed from the sum of the variances of individual creep-crushing elements:

$$F_{\text{std}}(v_{\text{ref}}) = \sqrt{N \cdot (\mathrm{E}[F(v_{\text{ref}})^2] - \mathrm{E}[F(v_{\text{ref}})]^2)} \tag{4.22}$$

$$= \sqrt{N \left(\frac{K_3^2 \int_0^{t_{\text{fail}}} u_3^2 \mathrm{d}t}{\frac{\mathrm{E}[r]}{v_{\text{ref}}} + t_{\text{fail}}} - F_{mean}^2(v_{\text{ref}}) \right)} \tag{4.23}$$

The peak frequency at v_{ref} in the load spectrum generated by the model, is derived from the failure of single creep-crushing elements. As it is assumed that the behavior is purely elastic, the peak frequency can be determined as follows:

$$f_{\text{peak}}(v_{\text{ref}}) = \frac{\mathrm{E}[r] + \delta_{\text{crit}}}{v_{\text{ref}}} \tag{4.24}$$

Finally, the maximum load occurs when all elements are in contact with the structure, at their maximum internal load before failure. This maximum load should be equal to the maximum load at transition velocity:

$$F_{\text{trans}} = \frac{h_{\text{ref}}}{h} \cdot N_{\text{ref}} \cdot K_3 \cdot \delta_{\text{crit}} \tag{4.25}$$

Where it is assumed that the maximum load scales linearly with the ice thickness h. These relations are now used to determine the input parameters.

Failure parameters

The failure parameters are defined as r_{max} and δ_{crit} and are independent of ice thickness and structure diameter. Their definitions are given first:

- **The maximum offset** r_{max} is the maximum local 'gap' that can occur between the ice and the structure after failure of an element.
- **The critical deformation** δ_{crit} is the maximum purely elastic deformation that can occur before local failure.

From Equation 4.21 to Equation 4.25 the following definitions for the parameters δ_{crit} and r_{max} can be derived:

$$\delta_{\text{crit}} = 2\frac{F_{\text{mean}}}{F_{\text{trans}}}\frac{v_{\text{ref}}}{f_{\text{peak}}} \tag{4.26}$$

$$r_{\text{max}} = \frac{v_{\text{ref}}}{f_{\text{peak}}}\left(2 - 4\frac{F_{\text{mean}}}{F_{\text{trans}}}\right) \tag{4.27}$$

Number of elements

The number of elements is an important factor to the stochastic behavior described by the model.

- N_{ref} is the number of elements required to reproduce the statistics of the reference loads;
- N is the number of elements scaled to the structure width.

The definitions for the number of elements can be found from Equation 4.21 to 4.25:

$$N_{\text{ref}} = \frac{2}{3}\frac{F_{\text{trans}}F_{\text{mean}} - F_{\text{mean}}^2}{F_{\text{std}}^2} \tag{4.28}$$

It is assumed that the size of the contact zones does not change with increasing structure width. The number of elements in the model is therefore given as:

$$N = \frac{b_s}{b_{\text{ref}}}N_{\text{ref}} \tag{4.29}$$

Kinematic element parameters

The parameter K_3 determines the elastic behavior of the creep-crushing element. Furthermore, it is assumed that the maximum load scales with the ice thickness. The definition for K_3 can therefore be derived from Equation 4.25:

$$K_3 = \frac{h}{h_{\text{ref}}} \frac{F_{\text{trans}}}{N_{\text{ref}} \delta_{\text{crit}}} \tag{4.30}$$

The parameter C_1 determines the viscous behavior during creep. It should prevent the element from failing below the transition velocity v_{trans} and is therefore related to the failure load.

$$C_1 = K_3 \frac{\delta_{\text{crit}}}{v_{\text{trans}}} \tag{4.31}$$

It is assumed that the ice behaves elastically up to a certain load. This limit is defined by the load at which the first micro cracks start to form. Schulson and Duval (2009) and Nakazawa and Sodhi (1990) have shown that this load can be estimated at $1/3$ of the failure load which was discussed before in section 2.3. After the activation load has been reached, the sliding element is switches from stick to slip. Therefore, the critical load in the sliding element is defined by Equation 4.32, where γ is equal to 0.3.

$$F_{\text{crit}} = \gamma K_3 \delta_{\text{crit}} \tag{4.32}$$

Finally, the elastic-visco-plastic behavior during slip is determined by C_2 and K_3. These parameters are functions of the stiffness K_3 and the damping coefficient C_1 respectively.

$$C_2 = \alpha K_3 \frac{\delta_{\text{crit}}}{v_{\text{trans}}} \tag{4.33}$$

$$K_2 = \beta K_3 \tag{4.34}$$

Where α and β are coefficients that can be found iteratively. This iterative process is based on the equations for t_{peak} and $F_{2\text{vtrans}}$. Where t_{peak} is defined as the time at which maximum load is reached in a creep failue, on a rigid structure, at v_{trans}. Furthermore, $\frac{1}{2} r_{\text{max}}$ is taken as the expected value of the uniformly distributed value for the offset r.

$$t_{\text{peak}} = \frac{\frac{1}{2} r_{\text{max}}}{v_{\text{trans}}} + t_{f1} \tag{4.35}$$

Where t_{f1} is the time until a factor $f_1 = 0.98$ of the maximum deformation δ_{crit} is reached, from the moment of first contact between the ice element and the structure. Therefore, the following equation, depending on the coefficients α and β must be satisfied:

$$u_3(t_{f1}, v_{\text{trans}}) = f_1 \cdot \delta_{\text{crit}} \tag{4.36}$$

The equation for the mean load at $2 \cdot v_{\text{trans}}$, $F_{2\text{vtrans}}$ also must be satisfied for α and β.

$$F_{2\text{vtrans}} = N_{\text{ref}} \frac{K_3 \int_0^{t_{\text{fail}}} u_3(t, 2v_{\text{trans}})dt}{\frac{\frac{1}{2}r_{\max}}{v_{\text{trans}}} + t_{\text{fail}}(2v_{\text{trans}})} \tag{4.37}$$

Where t_{fail} at 2 times the transition velocity can be found by satisfying Equation 4.38, which states that the elastic deflection of an element at t_{fail} and ice velocity $2v_{\text{trans}}$ should be equal to the maximum elastic deflection.

$$u_3(t_{\text{fail}}, 2v_{\text{trans}}) = \delta_{\text{crit}} \tag{4.38}$$

It must be noted that $u_3(t, v_{\text{ice}})$ in these equations is the solution for the deformation of the ice given an ice velocity v_{ice} from the moment of first contact.

4.3. Modeling buckling

To limit the crushing model from producing results in the range of large aspect ratios b/h, where crushing does not occur, the failure mechanism of buckling is included. Buckling is modeled in an uncoupled manner as the dynamic ice effects are already included in the creep-crushing part of the model. The modeling of buckling failure is done according to the buckling of wedges theory by Kerr (1978) as discussed in section 3.1.

4.3.1. Elastic buckling

Kerr (1978) describes elastic buckling of a floating wedge by the following differential equation for vertical deflection w:

$$\left[D(b_0 + y\phi^*) \frac{\mathrm{d}^2 w}{\mathrm{d}y^2} \right] \frac{\mathrm{d}^2}{\mathrm{d}y^2} + P \frac{\mathrm{d}^2 w}{\mathrm{d}y^2} + \gamma_{\text{w}}(b_0 + y\phi^*) = 0 \tag{4.39}$$

Where:

$$D = \frac{Eh^3}{12(I - \nu^2)} \tag{4.40}$$

$$\phi^* = 2 \tan\left(\frac{\phi_{\text{rc}}}{2}\right) \tag{4.41}$$

$$\tag{4.42}$$

And where $\gamma_{\text{w}} = g\rho_w$ is the specific weight of water, D is the flexural stiffness of the wedge, and P is the load applied to the wedge. Furthermore, ϕ_{rc} is the angle at which the radial crack occurs, assumed to be equal to $\frac{\pi}{4}$. The definition of the limiting load depends on the boundary conditions. To determine these conditions the following is considered:

- The ice is able to bend freely, far away from the contact zone with structure;
- At the contact zone with the structure, rubble ice can block the sheet from moving in vertical direction due to its weight and buoyancy;
- Friction between the ice and the structure can prevent or reduce vertical motion.

Sodhi et al. (1983) shows that the boundary conditions at the ice-structure interface can be expected to be somewhere between theoretically free and simply supported. Considering the above, it was chosen to assume the ice to be simply supported. Furthermore, it is assumed that the wedge is long enough to reduce vertical deflection at the far end of the wedge to zero, due to the geometry of the wedge.

4.3.2. Dynamic buckling

A major disadvantage of pure elastic buckling is that it also occurs during very short peaks in the global ice load, since inertia is neglected. As these peaks occur relatively often in ice loading, buckling is modeled in a dynamic manner. In the dynamic ice-structure interaction model used in this thesis, buckling is implemented using a finite element model of a floating wedge. The method used to create the finite element model is described by Rixen (2012) and Gavin (2014). Here only the discretization of the ice sheet is explained which should be sufficient to the reader in understanding the concept.

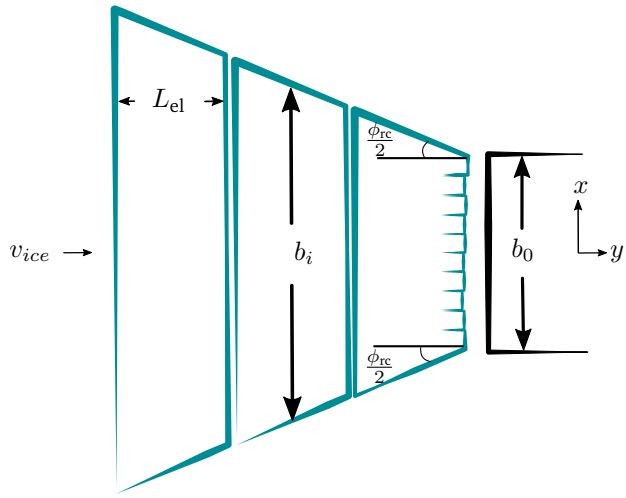

Figure 4.11: Schematic representation of the discretized buckling wedge (top view)

The wedge is divided into N_b Timoshenko beam elements of equal length L_{el}. A schematic representation of the descretization of the Timoshenko beam elements is given in Figure 4.11. The average width of element i can be determined as follows:

$$b_i = b_0 + L_{\text{el}} \left(i - \frac{1}{2} \right) \cdot 2 \cdot \tan \left(\frac{\phi_{\text{rc}}}{2} \right) \tag{4.43}$$

Where b_i is the average width of element i. For a constant ice thickness h_i, the area A_i of the element can easily be found as:

$$A_i = b_i \cdot h \tag{4.44}$$

Finally, the second moment of inertia for each element is found as:

$$I_i = \frac{h^3 b_i}{12} \tag{4.45}$$

Since these properties are obtained for all elements a matrix can be created for the mass, stiffness, and geometric stiffness of the element. The geometric stiffness is depending on the normal load, which is equal to the global ice load.

The stiffness matrix does not yet include the elastic Winkler foundation. The Winkler foundation is defined as a distributed stiffness γ_{w} over the surface area of the wedge. The Winkler stiffness matrix is found by integration over the shape function of the elements. This process is outside the scope of this thesis. It is sufficient to the reader to assume that these matrices have been obtained by subdividing the beam elements into sub elements. For each sub element the shape functions are evaluated and added to find the total element Winkler stiffness matrix. This results in the following equation that must be solved numerically for each time step:

$$\boldsymbol{M}_b \ddot{\boldsymbol{w}} + (\boldsymbol{K}_b + \boldsymbol{K}_W - \boldsymbol{G}_b(P))\boldsymbol{w} = \boldsymbol{F}(P) \tag{4.46}$$

Where $\boldsymbol{M}_b$ is the global mass matrix, $\boldsymbol{K}_b$ is the global stiffness matrix, $\boldsymbol{K}_W$ is the Winkler stiffness matrix, and $\boldsymbol{G}_b(P)$ is the global geometric stiffness matrix. $\boldsymbol{w}$ is the deflection vector including all degrees of freedom in the beam and $\boldsymbol{F}$ is a vector containing the global ice load applied P at the degree of freedom in the direction of the ice velocity, at the node that is in contact with the structure.

The failure load, and location of the failure L_{bf} is determined by the node at which the bending stress exceeds the flexural strength of the ice (Figure 4.12). After failure due to buckling of the wedge, the creep-crushing elements are reset to the location of the node at which failure occurred. New creep-crushing elements are therefore created at a distance of $L_{bf} + U(0, r_{\text{max}})$ from the structure.

Damping

Since the normal load varies over time, peaks exist that will induce propagating waves in the modeled ice sheet. When reaching the far end boundary, the waves are reflected and return in the direction of the structure. These reflected waves are a nonphysical results of

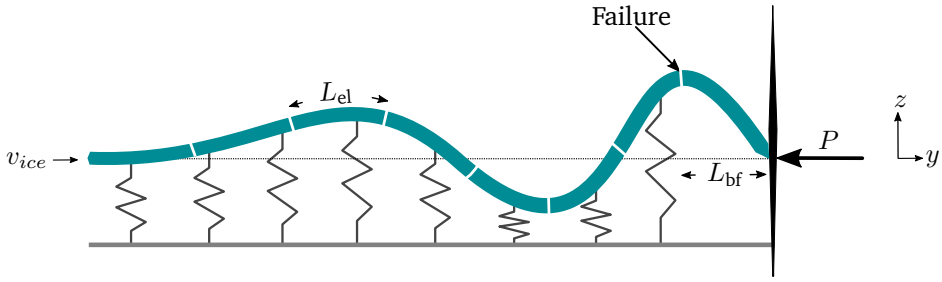

Figure 4.12: Schematic representation of the side view of the buckled wedge

the model but may induce vertical deflections $w(y,t)$ that results in buckling failure.

To mitigate this nonphysical effect, damping is added to the model. This damping is modeled in a simplistic way proportional to the Winkler stiffness matrix. The reason for this is that the damping is expected to be caused by the water beneath the floating wedge. The percentage of damping was chosen such that the reflected waves were unable to reach the structure with significant deflection.

4.4. Chapter summary

The phenomenological model proposed by Hendrikse and Metrikine (2015a) was implemented and extended with creep and buckling. The phenomenon of contact area variation was captured by N elastic-visco-plastic elements that were coupled to a structural model. The elements deform plastically at lower deformation rates, enabling the contact area to increase.

The input parameters of the model were derived from reference data. The required reference data is defined by reference parameters for three different ice velocities representing the ductile, transitional, and brittle regimes.

Buckling was included to the model, by the implementation of a finite element model. The ice sheet in the buckling model was represented by a wedge beam on an elastic Winkler foundation.

Chapter 5
Implementation of the phenomenological model for dynamic ice-structure interaction

In the previous chapter the phenomenological concepts behind the model for dynamic ice-structure interaction were discussed. This chapter continues on the implementation and the verification of these concepts. First, an overview is given of the numerical procedures of the model. This is done by describing the steps of a simulation.

The second part of this chapter, section 5.2, holds the reference data used to determine the input parameters of the model. Finally, a single degree of freedom structure is used in a verification study on the failure modes in section 5.3. This chapter concludes the part on the extension and implementation of the phenomenological model for dynamic ice-structure interaction.

5.1. Simulation framework for the phenomenological model

The phenomenological model described in the previous chapter is implemented into a Matlab tool, to simulate ice-structure interaction in the time domain. The flowchart in Figure 5.1 shows a high level overview of the procedures. The first procedure creates a class containing all simulation properties. This class uses the simulation options, the ice model, the structural model, and a wind model as input. The wind model will be used in the second part of this thesis. However, its implementation is described here to give a complete picture of the tool.

Depending on the simulation input, the model is assembled and the initial conditions are set. This process is described in detail in subsection 5.1.1. A Newmark numerical integration scheme for nonlinear dynamics is used to determine the solution for each time

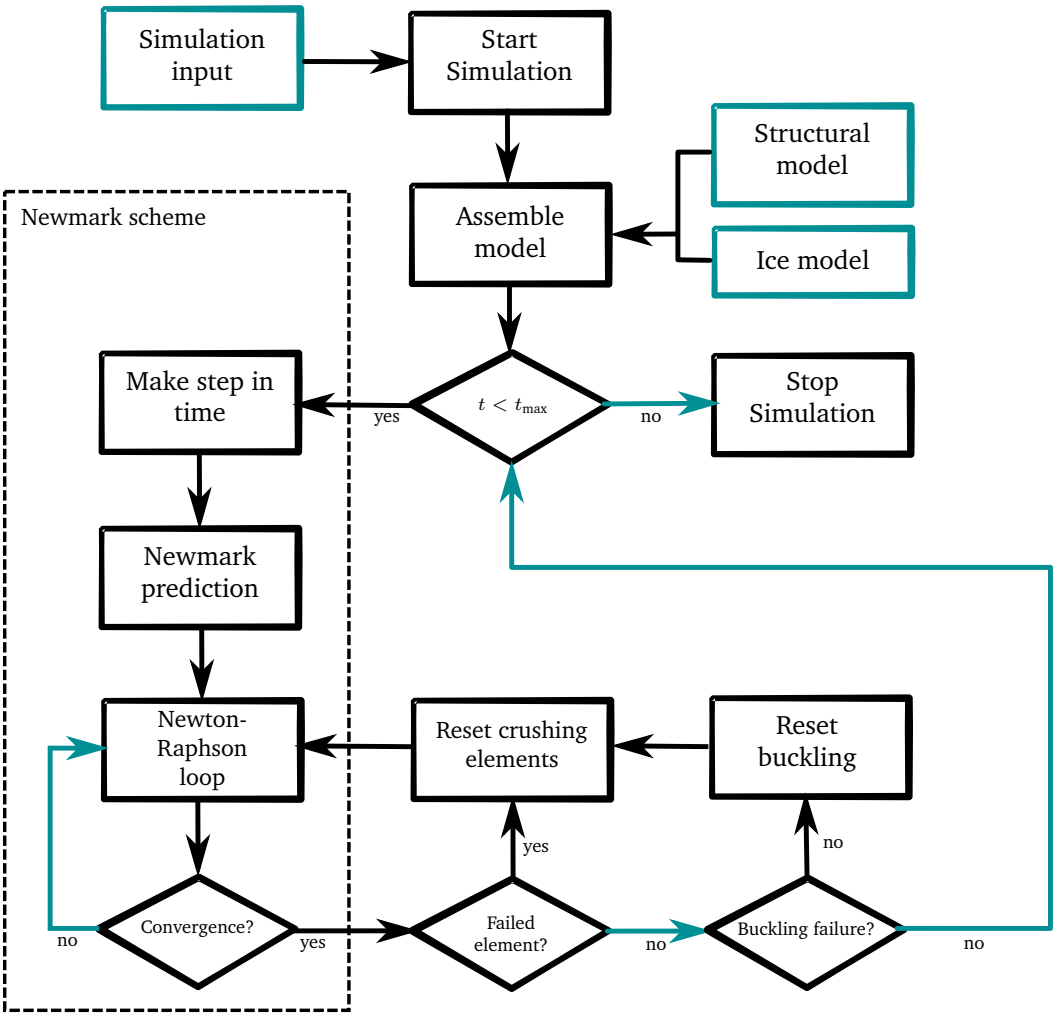

Figure 5.1: High level overview flowchart of model procedures

step. A discussion on the numerical details of this scheme can be found in Appendix A and an overview of the steps is described in subsection 5.1.2.

When a solution for the current time step t is found, the interaction forces are computed. It is checked if a maximum is exceeded, which would result in failure of the ice. If crushing or buckling failure occurs, the corresponding creep-crushing elements are given a new location as described in section 4.1 and section 4.3. This procedure is referred to as 'resetting of the ice elements'. After resetting is performed, a new solution is found using

the Newton-Raphson scheme. When no failure occurs, it is checked if the maximum simulation time is reached and the simulation continues to the next time step $t + \Delta t$ if this is not the case.

5.1.1. Initializing the simulation

Before the first time step of a simulation, the simulation input parameters are assembled into a mass, damping, and stiffness matrix and the initial conditions are set. The required input parameters for the model described in this part of this thesis are:

- The ice thickness;
- The ice velocity;
- The reference parameters (discussed in section 5.2);
- The structural parameters, i.e. mass, damping, and stiffness;
- The maximum simulation time $t_{\max}$;
- The time step size Δt.

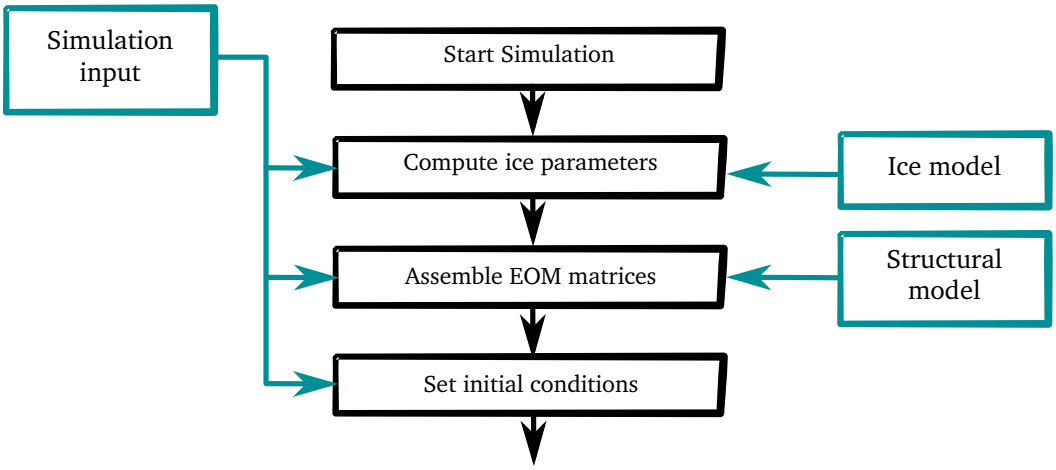

Figure 5.2: Flowchart of initialization procedure

Figure 5.2 shows the flowchart of the processes before the first time step:

1. The first step is to determine the ice model parameters, from the reference set, for the input ice thickness. The output of the ice model consists of the properties as described in section 4.2 and the matrices of the FE-model for buckling.

2. The mass, damping, and stiffness matrices of the structural model are used to assemble the system into three matrices. It must be noted that the total stiffness matrix depends on the deflections and therefore will be updated during the simulation.

3. The initial conditions for the ice crushing elements, floating wedge, and the structure are set and assembled into a deflection, velocity, and acceleration vector.

The results of these steps are the mass matrix $\boldsymbol{M}$, the damping matrix $\boldsymbol{C}$, the stiffness matrix $\boldsymbol{K}$, and the initial conditions for the assembled system. This data is then passed on to the numerical time integration solver.

5.1.2. Numerical time stepping

The first part of the numerical time stepping loop consists of a Newmark scheme in conjunction with a Newton-Raphson scheme, to find a solution for the following problem:

$$\boldsymbol{r}(\boldsymbol{u}_n) = \boldsymbol{M}\ddot{\boldsymbol{u}}_n + \boldsymbol{C}\dot{\boldsymbol{u}}_n + \boldsymbol{K}(\boldsymbol{u}_n)\boldsymbol{u}_n - \boldsymbol{g}(\boldsymbol{u}_n) = 0 \tag{5.1}$$

Here, $\boldsymbol{r}$ is the residual, and $\boldsymbol{g}$ is the external load vector. As discussed in the previous chapter, the stiffness matrix and the external load vector are dependent on the displacement vector. The Newton-Raphson loop linearizes the problem and iterates the residual to a value below a certain tolerance, i.e. close to zero. This process is explained in detail in Appendix A. For now, it is sufficient to mention that for each step in time, the integration scheme starts with a prediction of the solution. The stiffness matrix and the external load vector are updated for each iteration, since they are dependent on the solution itself. The Newmark scheme concludes with a correction step, which is repeated until a converged solution is found.

The input for this part of the simulation consists of the mass matrix, the damping matrix, the stiffness matrix, and the (initial) conditions for the complete system. The following steps are made and illustrated in Figure 5.3:

1. A step in time is made according to the chosen time step size Δt.

2. The displacement of the far end of each ice element $u_{1,i}$ is increased by $v_{\text{ice}} \cdot \Delta t$.

3. A prediction is made for the solution to Equation 5.1, according to the Newmark scheme.

4. The stiffness matrix and the external load vector are updated. Furthermore, the applied normal load to the floating wedge is calculated.

5. The residual is computed to determine the corrections that are to be made.

6. Eventually the Newton-Raphson loop converges the residual to a value below the tolerance.

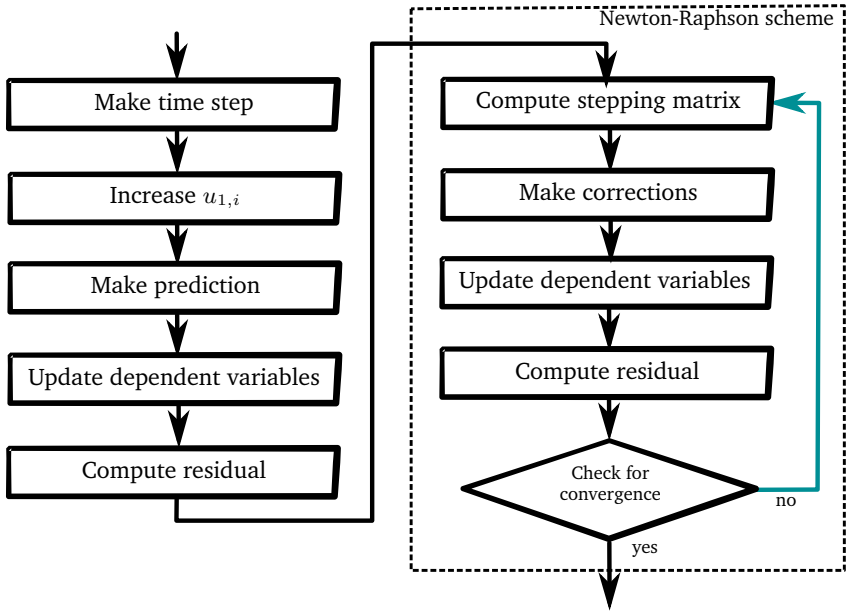

Figure 5.3: Flowchart of numerical time stepping procedures

(a) The stepping matrix is computed.

(b) The corrections are computed and applied to the deflection, velocity, and acceleration vectors.

(c) The stiffness matrix, the load vector, and the applied buckling load are updated for the new conditions.

(d) The residual is computed again.

(e) And finally, a check is done to determine if the solution has converged. If the solution is not converged, the Newton-Raphson loop continues iteratively until convergence is reached.

Eventually, a converged solution for the current time step is found. The output of this part of the simulation are the converged deflection, velocity, and acceleration vector.

5.1.3. Modeling ice failure

The second part of the time stepping loop checks if failure has occurred during the previous time step. This is done by calculating the force in each creep-crushing element. Furthermore, the bending stress in the wedge beam is computed. Failure occurs when these internal forces exceed the respective maximum values. If exceedance occurs, the resetting

procedure is started. Figure 5.4 shows a flowchart op the procedures and a detailed explanation follows below.

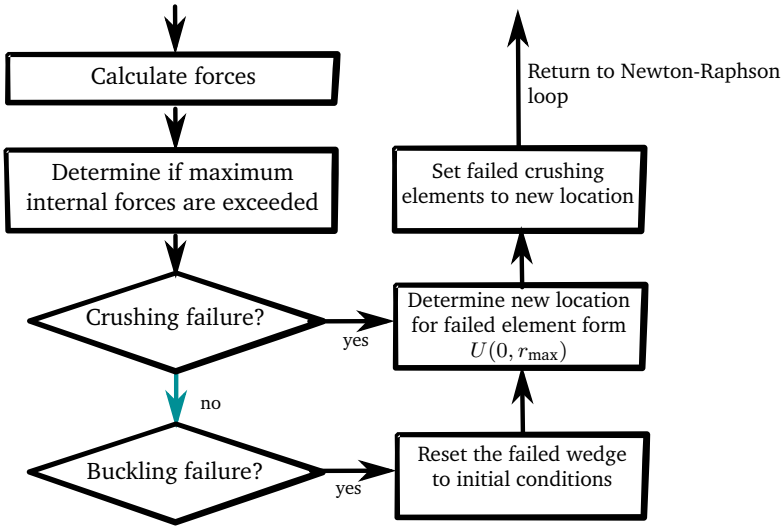

Figure 5.4: Flowchart of creep-crushing element- and buckling failure procedures

The inputs to this part of the simulation loop are the conditions following from the solution found by the numerical time integration solver.

1. The forces in the creep crushing elements are calculated from $K_{3,i}(u_{3,i} - u_{2,i})$. Where $K_{3,i}$ is the elastic stiffness of element i depending on the contact condition of the creep-crushing element.

2. It is determined if the maximum load of $K_3\delta_{\text{crit}}$ is exceeded. Where K_3 and δ_{crit} are input parameters of the ice model.

3. A check is done if a creep-crushing element has failed.

   (a) If one or more creep-crushing elements have failed, a new location is determined as a distance to the structure from $U(0, r_{\max})$.

   (b) The failed elements are given a new location.

   (c) The simulation returns to the start of the Newton-Raphson loop to find a solution for the new conditions.

4. If no creep-crushing elements have failed, the internal bending stress of the floating wedge is calculated.

5. It is checked if the flexural strength is exceeded and thus if buckling failure has occurred.
   (a) If buckling failure has occurred, the floating wedge is reset to its initial conditions.
   (b) The creep-crushing elements are reset to a new location defined as a distance from the structure: $L_{bf} + U(0, r_{max})$.
   (c) After resetting the creep-crushing elements, the simulation continues to the start of the Newton-Raphson loop to find a solution for the new conditions.
6. If no buckling failure occurs, the simulation continues to check if the maximum time has been reached and stops the simulation if that is the case.
7. If the maximum time has not been reached yet, the simulation continues to the start of the Newmark integration loop and makes a step in time.

5.1.4. Variable time stepping

An important question to ask oneself before pressing the enter button is what time step size Δt to use. A brief sensitivity study was done on the variation of time step sizes of which the conclusions are described here.

Due to the nature of checking for failure after a time step has been made, it is only checked if an element has failed before the new instance time. Although this sounds obvious, it has the unfortunate consequence that resetting always occurs too late. This results in the fact that the global ice load is overestimated for this particular situation. However, this should not impose a significant error if the time step size is chosen small enough.

The same problem arises for other discrete events. Therefore, a variable time stepping algorithm was created to approach a minimal time step near these events with a minimum time step size Δt_{min}.

Figure 5.5 shows the flowchart of the algorithm used. It is similar to the flowchart of Figure 5.1 with a few adjustments. The initialization procedure and the numerical time stepping procedures remain equal. After a solution is found it is checked if one of the following events has occurred:

- A crushing element has failed
- The buckling wedge has failed
- A switch between contact and no contact was made
- A switch between stick and slip was made

The procedure of variable time stepping is as follows:

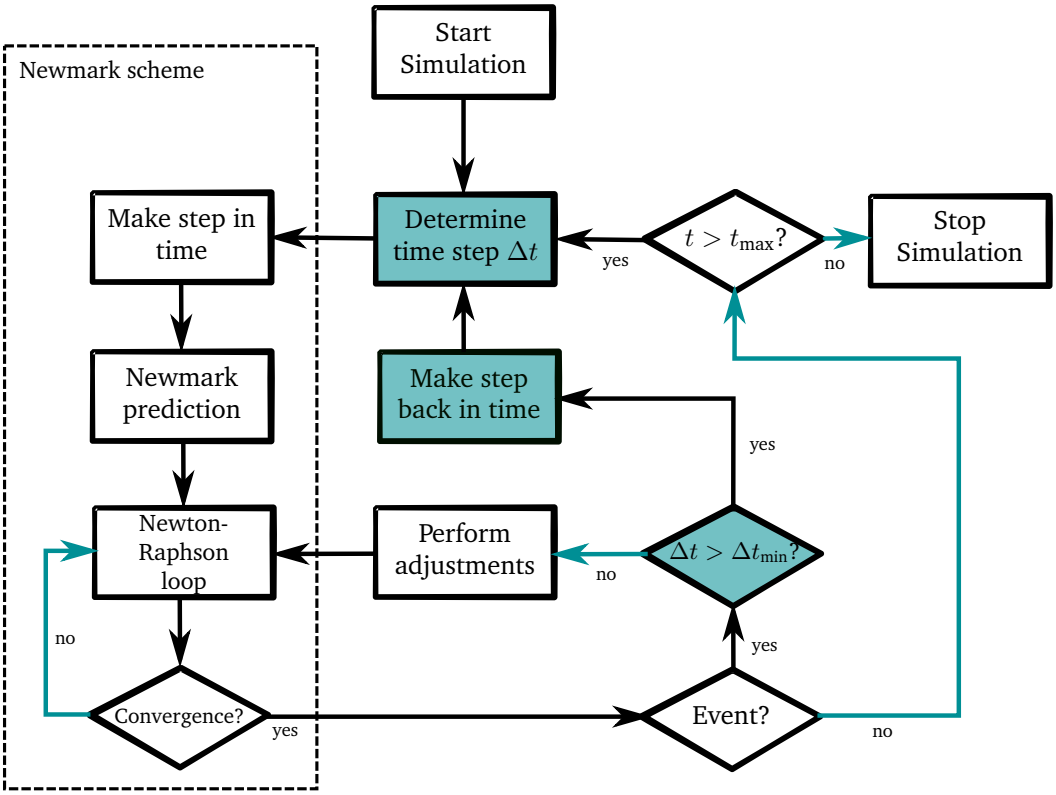

Figure 5.5: Flowchart of variable time stepping adjustments

1. If one of the above listed events occurred during the current time step, a check is made if the current time step size Δt is larger than the minimum time step size Δt_{min}.
2. If this is the case, a step back in time ($t - \Delta t$) is made disregarding the solution that was found.
3. A smaller time step size Δt is chosen and a new solution is found.
4. The smaller time step size is used until an event has occurred. Moreover, the time step size is decreased until the minimum Δt_{min} is reached.
5. When Δt_{min} is reached, adjustments are made in case of buckling failure or failure of crushing elements. A new solution is found and the time step size Δt is set back to its maximum value for the next step.

From this point onward the simulation procedures are equal to the discussed procedures in this section. As a consequence, the results generated by such a model, e.g, loads and

responses, will have a higher accuracy in comparison to a model that uses a constant time step size. However, this algorithm drastically increases the computational time, especially in case of a large number of ice elements N.

5.2. Determination of the reference parameters

Since the model input parameters are based on reference data as discussed in section 4.2, measurement data is required to setup the model. A choice was made to use data from full-scale measurement to avoid scaling effects during the comparison study in the second part of this thesis. In other words, in this section measurement data is acquired and translated into the reference parameters of section 4.2. Firstly, a range of ice thicknesses is chosen followed by the reference parameters. The reference parameters are divided over the parameters for the brittle, ductile, and transitional regime.

5.2.1. Ice thickness

A range for the ice thicknesses in the Baltic Sea is described by Fransson and Lundqvist (2006). In the Gulf of Bothnia large landfast ice sheets loosen from the coast and drift out to sea. The sheets will grow to a thickness of approximately 10-40 cm. As the ice gradually grows thicker over winter, maximum ice thicknesses of 40-60 cm are reached in the North and 20-40cm in the South of the Baltic Sea. Since the OWT used for the case study in this thesis is located in the Southern part of the Baltic Sea, a choice was made to limit the ice thickness as given in Table 5.1.

Table 5.1: Values used for ice thickness range

Parameter	Symbol	Value	Unit
Ice thickness	h	$0.1 - 0.4$	m

5.2.2. Reference parameters for the brittle regime

Next, the reference parameters required to determine the input parameters are discussed. To the author's knowledge, the LOLEIF campaign is one of the most reliable full scale data sets at the time of writing. Nine load sensors were used to measure the load of the ice during interaction with the Norstromsgrund lighthouse as illustrated in Figure 5.6a. Fransson and Lundqvist (2006) give a stochastic approach to the data sets with extreme loading. Their findings on the mean pressure per panel, for brittle crushing at high ice velocities, are shown in Figure 5.6b.

The average mean pressure during continuous brittle crushing is estimated as 0.5 MPa for all panels. However, the required reference parameter is the mean global ice load in the

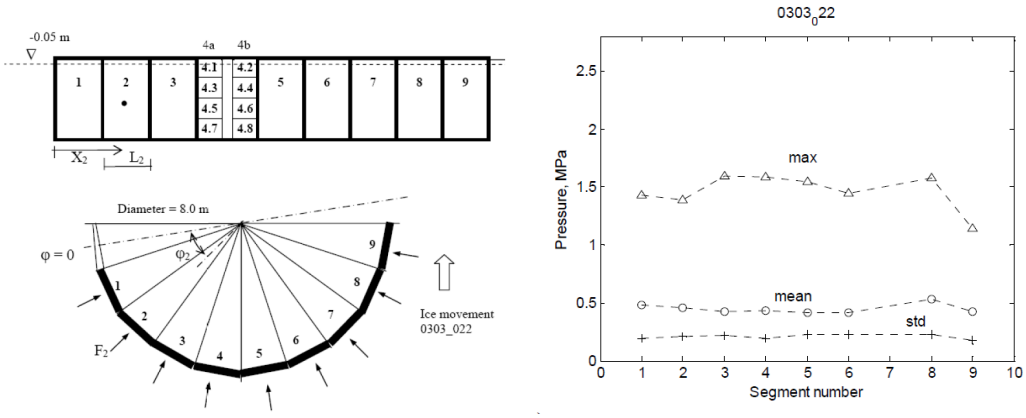

(a) Lay-out of pressure panels used in the Norstromsgrund campaign Fransson and Lundqvist (2006)

(b) Average pressure per panel measured during continuous brittle crushingFransson and Lundqvist (2006)

Figure 5.6

direction of the ice velocity. As the pressure is only measured in the direction normal to the panels, F_{mean} is calculated by integrating the mean load in the direction of the ice velocity. Assuming the pressure P_{mean} is applied to half a circle, the mean load can be found by multiplying the pressure with the ice thickness and the structure diameter. The used values to compute this mean load are given in Table 5.2.

$$F_{\text{mean}} = P_{\text{mean}} \cdot h_{\text{ref}} \cdot b_{\text{ref}} \tag{5.2}$$

Table 5.2: Values used to compute the mean load in the brittle regime (Fransson and Lundqvist, 2006)

Parameter	Symbol	Value	Unit
Mean pressure	P_{mean}	0.5	MPa
Reference ice velocity	v_{ref}	0.2	m/s
Reference ice thickness	h_{ref}	0.26	m
Reference structure diameter	b_{ref}	7.6	m
Mean load	F_{mean}	988	kN

The total standard deviation given by Fransson and Lundqvist (2006) was calculated from the sum of variances as:

$$F_{\text{std}} = \frac{\sqrt{9 \cdot (P_{\text{std}} \cdot h_{\text{ref}} \cdot b_{\text{ref}})^2}}{9} \tag{5.3}$$

For P_{std} = 0.25 MPa this gives a F_{std} of 167kN. This is considered a rather high value, since the number of creep-crushing elements N becomes too low during calculations with this value. Since Fransson and Lundqvist (2006) did not show the full time signal, it could be explained by other failure modes besides continuous brittle crushing occurring during the measurement, increasing the standard deviation. A second opinion was found from a full time signal, that was taken during similar measurements on the Norstromsgrund Lighthouse. To correctly implement the value of the time signal, it was assumed that the standard deviation of the load scales linearly with the ice thickness. The values used to compute and scale the standard deviation of this load are given in Table 5.3.

Table 5.3: Values used to compute the standard deviation in the brittle regime

Parameter	Symbol	Value	Unit
Ice velocity	v_{std}	0.35	m/s
Ice thickness	h_{std}	0.55	m
Standard deviation load	$F_{\text{std,unscaled}}$	216	kN
Standard deviation scaled to reference case	F_{std}	102	kN

The remaining reference parameter at brittle crushing velocities is the peak frequency. The load time series used for the standard deviation does not show an apparent peak frequency. Therefore, another approach was taken to find the remaining parameter.

Takeuchi and Sakai (2001) performed measurements on the roughness of the ice edge during crushing. From this research the critical deflection upon failure δ_{crit} was directly determined. From this value the failure frequency was calculated, using the equations in section 4.2. The parameters and their values are given in Table 5.4.

Table 5.4: Value for critical deflection by Takeuchi and Sakai (2001) and peak frequency derived from this value

Parameter	Symbol	Value	Unit
Critical deflection	δ_{crit}	9.7	mm
Peak frequency	f_{peak}	12.3	Hz

5.2.3. Reference parameters for the ductile regime

To obtain the global ice load at transition velocity, the results of full scale creep tests are required. However, usable results of creep tests at the Norstromsgrund Lighthouse are not

available to the author. Therefore, measurement data by Takeuchi and Sakai (2001) is used.

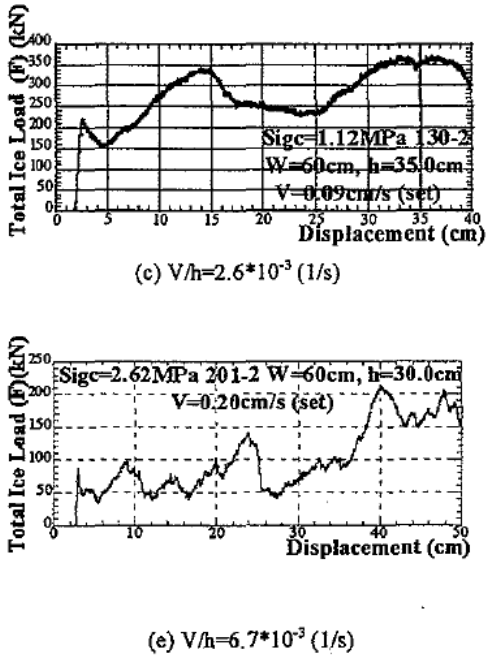

Figure 5.7: Full scale creep test measurements Takeuchi and Sakai (2001)

Figure 5.7 show ice load-time series for low ice velocities in Lake Notoro in Hokkaido, Japan, as part of the JOIA project. Lake Notoro is a salt water lake connected to the ocean and therefore expected to have similar properties as the Baltic Sea. The values for the reference parameters obtained from these measurements are given in Table 5.5.

Table 5.5: Values used to find global ice load at transition velocity

Parameter	**Symbol**	**Value**	**Unit**
Time to maximum load	t_{peak}	150	s
Measured ice velocity	v_{trans}	0.9	mm/s
Measured pressure	P_{trans}	1.67	MPa
Load at transition velocity scaled to reference case	F_{trans}	3.29	MN

The maximum load in the top graph of Figure 5.7, is interpreted as the highest load before the first drop. This occurs at a displacement of 15 cm, which is equal to 150 s after first loading. It is assumed that the pressure at transition velocity is equal for the

reference case. Moreover, Takeuchi's measurements show that transition from creep to crushing occurs around an ice velocity of 1 mm/s. Therefore, this velocity is used as the transition velocity.

5.2.4. Reference parameters for the transitional regime

Takeuchi also shows the result of measurements at two times the transition velocity. However, as crushing is considered here, the mean load should be estimated. It was estimated at 150 kN in Figure 5.7. The width of the structure was 60 cm and the ice thickness was 30 cm during these measurements. To enable usage of the data the measured pressure is obtained, and scaled to the reference case by multiplying the pressure by $b_{\text{ref}} \cdot h_{\text{ref}}$. The values for the parameters are given in Table 5.6

Table 5.6: Values used to find global ice load at transition velocity

Parameter	Symbol	Value	Unit
Measured ice velocity	$2v_{\text{trans}}$	2.0	mm/s
Measured pressure	$P_{2\text{vtrans}}$	0.83	MPa
Mean load at $2 \cdot v_{\text{trans}}$ scaled to reference case	$F_{2\text{vtrans}}$	1.65	MN

5.2.5. Parameters for the ice buckling model

To model buckling a few material properties are required. The parameters used are listed in Table 5.7.

Table 5.7: Values used for buckling parameters

Parameter	Symbol	Value	Unit
Young's modulus	E	4.0	GPa
Shear modulus	G	1.5	GPa
Poisson's ratio	ν_{ice}	0.33	-
Ice density	ρ_{ice}	910	kg/m^3
Sea water density	ρ_{w}	1027	kg/m^3
Flexural strength	σ_{f}	0.4	MPa

5.3. Verification of the phenomenological model

A verification study is performed to demonstrate that the model is qualitatively able to simulate the four failure mode categories discussed in section 3.1. The results are created using

the ice reference data determined in the previous section. This section starts by showing a curve of the relation between ice load and ice velocity as was discussed in section 4.2. An elaboration is made on each of the four categories of failure; creep, buckling, mixed-buckling crushing, and crushing. Where for crushing the three IIV regimes are treated separately. The section is concluded with a failure mode map, showing the distribution of failure modes and IIV regimes over ice velocity and ice thickness.

5.3.1. The load-velocity curve

To verify that the determined reference data is translated to the input parameters in a correct way, a curve for the global ice-load versus ice velocity is created. The curve shows the global ice load per ice velocity as the ice interacts with a rigid structure.

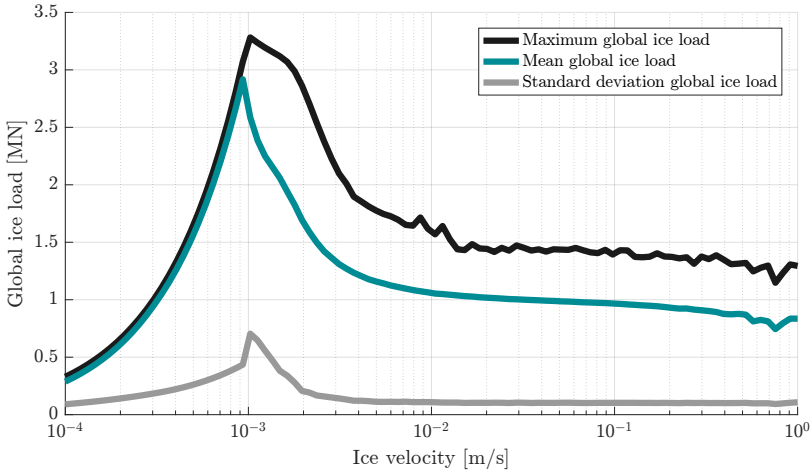

Figure 5.8: Ice-load versus ice velocity curve generated from 100 simulations against a rigid structure

Figure 5.8 shows the maximum, mean, and standard deviation of the global ice load against a rigid structure over ice velocities varying from 0.1 mm/s to 1000 mm/s. The curve was created for ice and structure conditions equal to that of the reference case discussed in the previous section. Therefore, the values must be equal to the chosen reference data. This values in Figure 5.8 are compared with the reference data in section 5.2:

- The maximum load occurs at $v_{\text{trans}} = 1$ mm/s and is equal to $F_{\text{trans}} = 3.29$ MN
- The mean load at two times $v_{\text{trans}} = 2$ mm/s is equal to $F_{2\text{vtrans}} = 1.65$ MN
- The mean load at $v_{\text{ref}} = 0.2$ m/s is equal to $F_{\text{mean}} = 988$ kN
- The standard deviation of the load at $v_{\text{ref}} = 0.2$ m/s is equal to $F_{\text{std}} = 102$ kN

This verifies the correct implementation of the input parameters from the reference parameters. Interaction with a compliant structure is considered next.

5.3.2. Structural model to verify dynamic ice-structure interaction

The interaction with a compliant structure is verified in the following subsections. The structure used for this verification study is a one degree of freedom mass-spring-damper system. The mass, stiffness, and damping coefficient are determined from the order of magnitude of the modal values of the second bending mode of an arbitrary OWT. It should be noted that this gives realistic behavior in a qualitative sense, and that no further conclusions besides verification should be drawn from the figures in this section. The values for the structure are given in Table 5.8.

Table 5.8: Values used for the structure during verification of the numerical model

Parameter	Symbol	Value	Unit
Mass	M_s	1000	ton
Damping	C_s	215	kNs/m
Damping ratio	ζ	1.6	%
Stiffness	K_s	40	MN/m
Natural frequency	f_n	1	Hz
Structure width	b_s	6	m

5.3.3. Verification of creep failure

The expected behavior for creep is a growing, and eventually constant ice loading at very low ice velocities. No brittle failure should occur during a simulation. An example of a creep test was shown in Figure 5.7 and the results of a simulation by the phenomenological model, with of similar ice conditions, is given in Figure 5.9. This graph shows a comparison between structural displacement on the left y-axis, and the global ice load on the right y-axis. All graphs in this section use the same approach and conclusions will be based on these two types of curves. First, the input values for ice thickness and velocity are given in Table 5.9.

Table 5.9: Ice thickness and ice velocity used to verify creep

Parameter	Symbol	Value	Unit
Ice velocity	v_{ice}	0.9	mm/s
Ice thickness	h	400	mm

An obvious difference when comparing Figure 5.9 to Figure 5.7 is the drop of the loading during the test in Figure 5.9. This drop is believed to be caused by strain softening

behavior due to the formation of micro cracks (Schulson and Duval, 2009). This behavior is not modeled as it is expected to have no significant influence on dynamics.

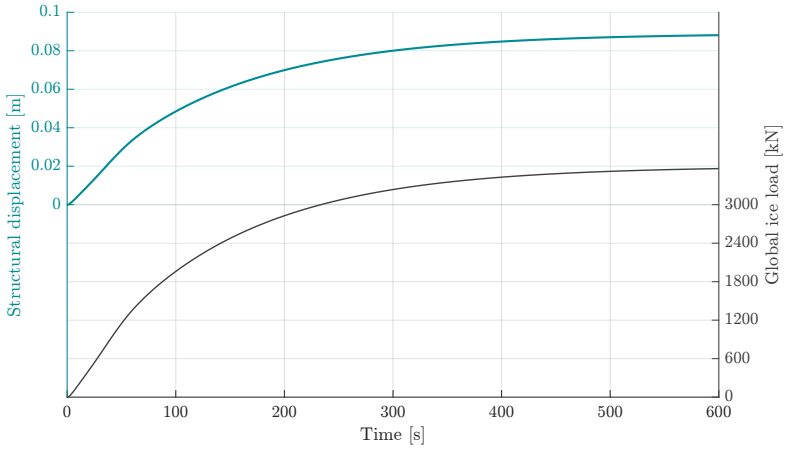

Figure 5.9: Simulation of creep using an ice thickness of 200mm and an ice velocity of 0.9mm/s

The creep simulation in Figure 5.9 shows that the load as well as the displacement increase slowly until they reach a certain maximum. The part where the load increases is related to a slow increase in the contact area until full contact, and thus maximum load is reached. The quasi constant load following this process is related to pure ductile failure. This behavior is expected at the chosen ice velocity since it is below the transition velocity. Furthermore, the behavior covers the modeled characteristics of creep as described in section 3.1.

5.3.4. Verification of buckling failure

Buckling behavior is expected to cause a short loading peak until the flexural strength of the wedge is reached. After buckling failure has occurred the global ice load is expected to be zero until the ice is back in contact with the structure. During the period of zero loading the structure will show free vibration, with a decaying amplitude due to the damping. The values used to simulate pure buckling consist of a relatively thin ice sheet at an intermediate ice velocity and are give in Table 5.10.

Figure 5.10 shows the global ice load and the displacement of the structure during the simulation. It can be concluded that the the ice load as well as the displacement of the structure show the expected behavior as described above.

Table 5.10: Ice thickness and ice velocity used to verify buckling

Parameter	Symbol	Value	Unit
Ice velocity	v_{ice}	50	mm/s
Ice thickness	h	10	mm

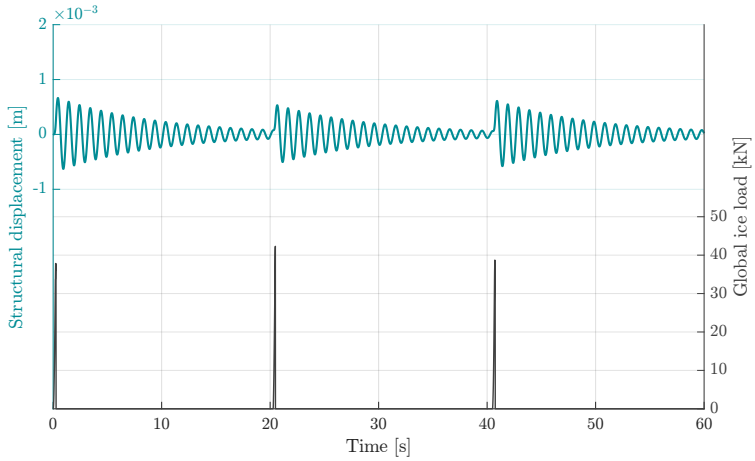

Figure 5.10: Simulation of buckling using an ice thickness of 10 mm and an ice velocity of 50 mm/s

5.3.5. Verification of mixed buckling-crushing failure

At higher velocities compared to the pure buckling mode, also crushing occurs. The global ice load is fluctuating around its mean value with a certain standard deviation and maximum. If the mean global ice load, resulting from the brittle crushing behavior, is in the vicinity of the load that induces buckling failure both failure modes exist. This combination results in periods of crushing alternated with periods of zero loading. During zero loading, the structure is expected show free vibration, with a decaying amplitude over time due to the damping. The values used for the mixed behavior are shown in Table 5.11.

Table 5.11: Ice thickness and ice velocity used to verify mixed buckling-crushing

Parameter	Symbol	Value	Unit
Ice velocity	v_{ice}	200	mm/s
Ice thickness	h	10	mm

Figure 5.11 shows the global ice load and the displacement of the structure during

the mixed buckling-crushing simulation. It can be concluded that the behavior shows the expected behavior as described above.

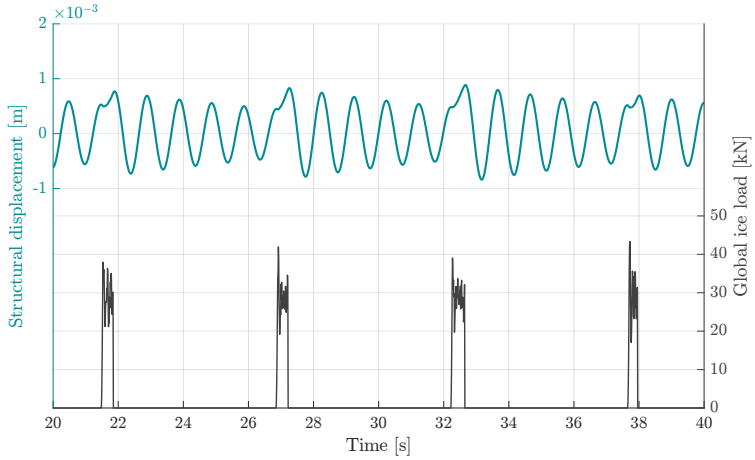

Figure 5.11: Simulation of mixed buckling-crushing using an ice thickness of 10 mm and an ice velocity of 200 mm/s

5.3.6. Verification of intermittent crushing

In the following three subsections, the crushing regimes will be discussed. For low ice velocities above the transition velocity, it is expected that intermittent crushing occurs. This behavior is featured by a distinctive saw tooth pattern due to its loading and unloading phases. At first the structure is loaded by the ice as it moves in the same direction. Due to the low relative velocity ductile behavior occurs; no ice fails in a brittle manner. As the structure reaches a maximum deflection, also a maximum in the load is reached. Next, brittle failure arises while the relative velocity increases as structure starts moving in the opposite direction of the ice. A period of pure brittle crushing occurs until the relative velocity is so low that only ductile behavior remains.

Table 5.12: Ice thickness and ice velocity used to verify intermittent crushing

Parameter	Symbol	Value	Unit
Ice velocity	v_{ice}	10	mm/s
Ice thickness	h	400	mm

Furthermore, as for all crushing regimes, the behavior is expected to occur at relatively higher ice thicknesses, since otherwise the ice will buckle. The values used to simulate intermittent crushing are therefore chosen as given in Table 5.12.

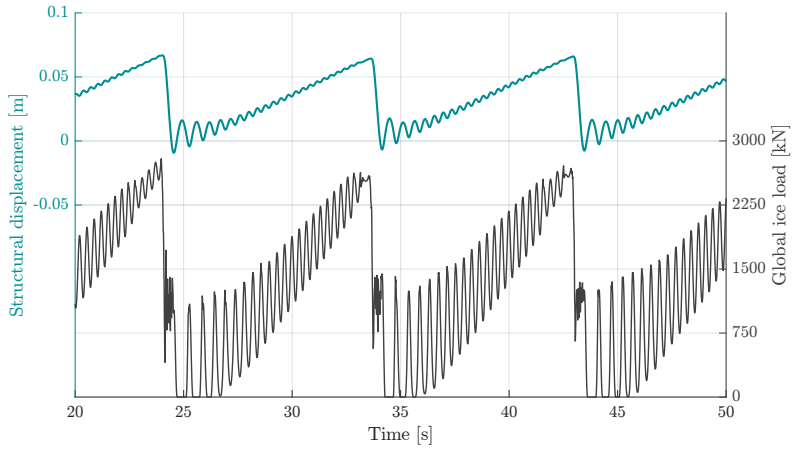

Figure 5.12: Simulation of intermittent crushing using an ice thickness of 400mm and an ice velocity of 10mm/s

Figure 5.12 shows the global ice load and the displacement of the structure during the intermittent crushing simulation. The saw-tooth shape is clearly visible in the displacement of the structure as well as in the ice loading. Furthermore, the phases described above fit the results of the simulation.

5.3.7. Verification of frequency lock-in

Frequency lock-in is expected at intermediate crushing velocities. During a loading cycle the relative velocity remains near the transition velocity for a certain amount of time, referred to as the loading phase. The duration of the loading phase determines if and how much synchronization of the ice, with the structure, is possible. As the ice synchronizes, the contact area and thus the global ice load increases. The behavior is considered as frequency lock-in, if this load is in a range that it will excite the structure to a maximum velocity that is higher than the ice velocity itself and keeps doing so in a frequency close to the natural frequency of the structure. Table 5.14 shows that a higher ice velocity is used to simulate FLI.

Table 5.13: Ice thickness and ice velocity used to verify frequency lock-in

Parameter	Symbol	Value	Unit
Ice velocity	v_{ice}	400	mm/s
Ice thickness	h	400	mm

Figure 5.13 clearly shows the structure vibrating in its natural frequency of 1 Hz. Fur-

thermore, Figure 5.14 shows the relative velocity between the structure and the ice to be negative in each cycle. This indicates that at this instance in time the structure is moving in the same direction as the ice with a velocity higher than the ice velocity, hence FLI occurs.

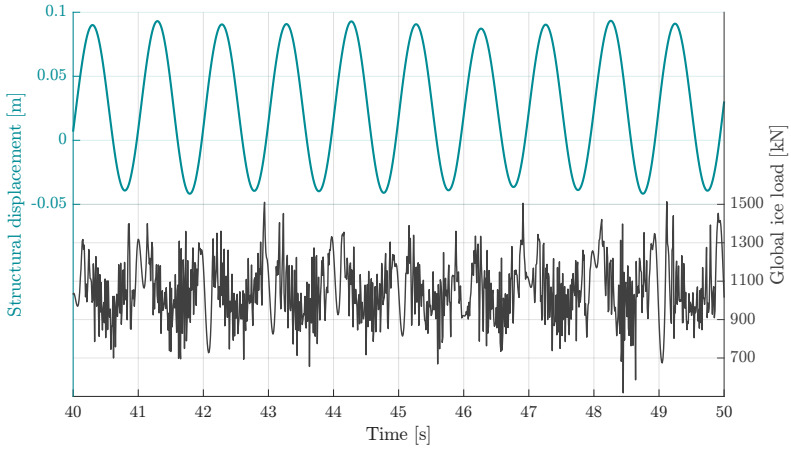

Figure 5.13: Simulation of frequency lock-in using an ice thickness of 400mm and an ice velocity of 400mm/s

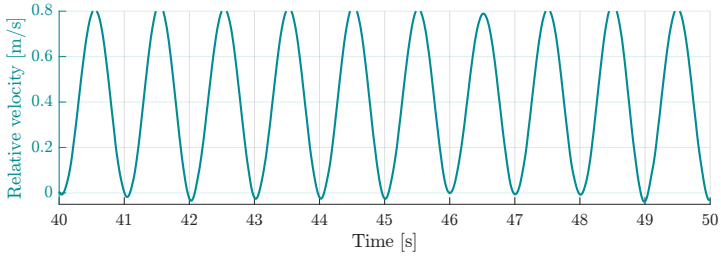

Figure 5.14: Relative velocity during FLI simulation

5.3.8. Verification of continuous brittle crushing

Finally, continuous brittle crushing occurs at ice velocities higher than where frequency lock-in occurs. It is expected that the load signal will show quasi-random loading no synchronization occurs. Furthermore, the response of the structure will be quasi-random as well, with a positive mean value.

Due to the high ice velocity the ice can be assumed to behave purely elastic. This results in a quasi-random load showed in Figure 5.15.

Table 5.14: Ice thickness and ice velocity used to verify continuous brittle crushing

Parameter	Symbol	Value	Unit
Ice velocity	v_{ice}	800	mm/s
Ice thickness	h	400	mm

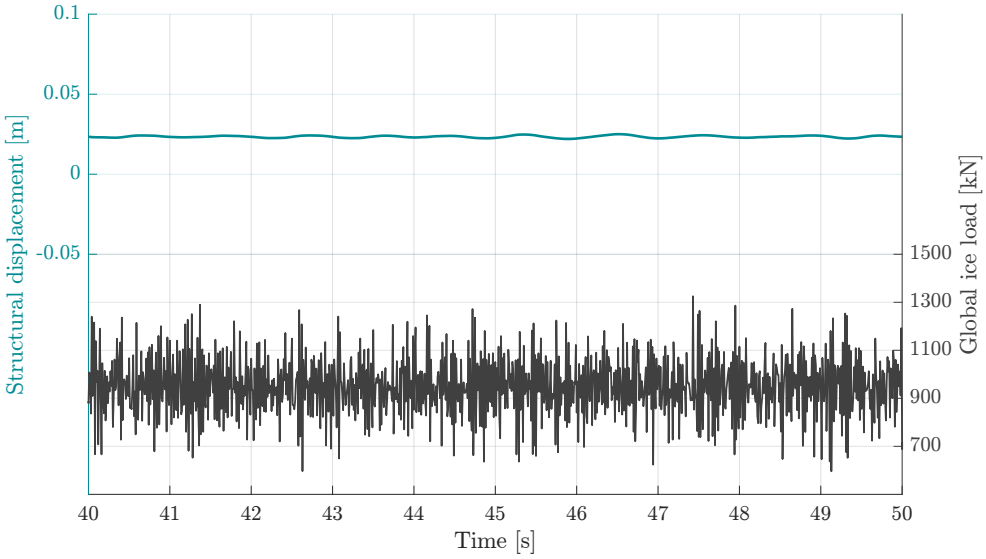

Figure 5.15: Simulation of continues brittle crushing using an ice thickness of 400mm and an ice velocity of 800mm/s

5.3.9. Qualitative verification using the failure mode map

In subsection 3.1.4 the failure mode map by Timco (1991) was discussed. A similar map was made for the phenomenological model used in this thesis. However, the axes were chosen differently since the map is depending on the structure's width.

Figure 5.16 shows the failure map created from the results of the phenomenological model for dynamic ice-structure interaction. To create the map, 625 simulations were run of 600 seconds each. The first 200 seconds were cut off to exclude start-up behavior. For each simulation it was checked if buckling or crushing occurs. If crushing occurs, the governing response frequency and the relative velocity were checked as well. The failure modes and regimes were determined by the criteria given in Table 5.15.

The following conclusions are drawn from the failure map shown in Figure 5.16:

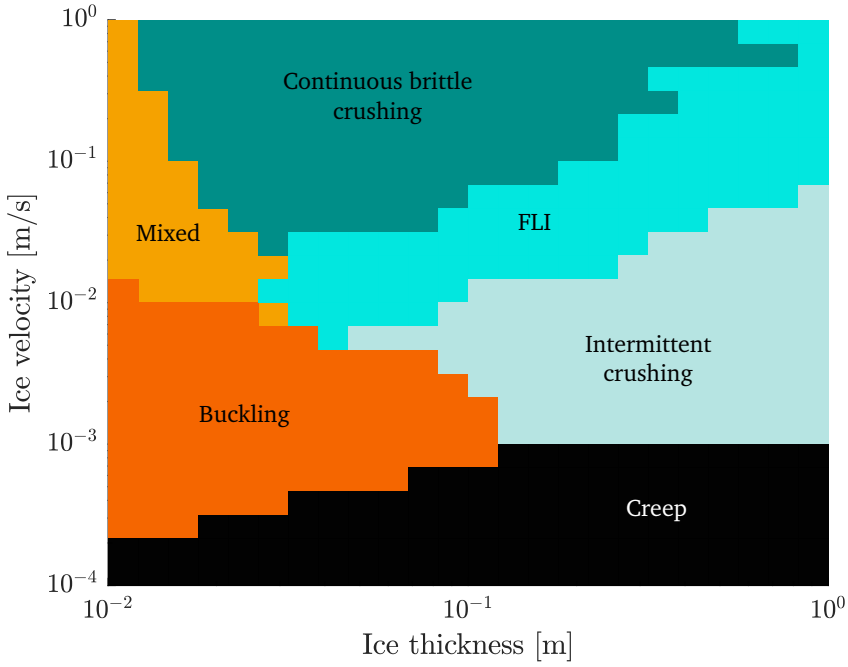

Figure 5.16: Failure map for one degree of freedom structure, $b_s = 6$m

Table 5.15: Criteria for determining failure modes and regimes

Failure mode/regime	**Crushing**	**Buckling**	$f_{\text{response}} = f_{\text{n}}$	Negative v_{rel}
Creep				
Buckling		✓		
Mixed buckling-crushing	✓	✓		
Intermittent crushing	✓			
FLI	✓		✓	✓
Cont. brittle crushing	✓		✓	

- Creep occurs below the transition velocity over all ice thicknesses.
- Buckling occurs at intermediate ice velocities and low ice thicknesses.
- Mixed buckling-crushing occurs as a transition between pure buckling and crushing.
- Intermittent crushing occurs at ice velocities above the transition velocity, and relatively higher ice thicknesses.
- Frequency lock-in occurs at velocities higher than intermittent crushing.

- Continuous brittle crushing occurs at relatively high ice velocities and relatively high ice thicknesses.

Comparing these conclusions with the failure mode map by Timco (1991), as discussed in section 3.1, it is concluded that the behavior of the model qualitatively shows good correspondence to the behavior observed by Timco. This concludes the verification study of the model.

5.4. Chapter summary

The phenomenological model was implemented in a numerical model to simulate dynamic ice-structure interaction in the time domain. The model uses a Newmark scheme for non-linear dynamics to solve the system of equations in time. Moreover, a variable time stepping algorithm was created to approach the events that occur during a simulation.

To set up the phenomenological model, measurement data is required. The measurement data was acquired and translated to the reference parameters. A verification study was performed to demonstrate that the reference parameters were matched. Furthermore, a qualitative verification was successfully performed on the failure mode and IIV regimes using a failure mode map.

Part II
Application of the phenomenological model to an offshore wind turbine

Chapter 6
Application to an offshore wind turbine

Part I started with an introduction to the properties of ice. The phenomenological model for dynamic ice-structure interaction was explained and extended to include creep and buckling. Part II will focus on the application of the model to an offshore wind turbine. For the implementation, some adjustments are made to accommodate the cylindrical shape of the OWT in section 6.1. This includes the ability of lateral loading of the OWT. Next, the structural model of the OWT is discussed in section 6.2. Finally, the chapter is concluded with an elaboration on the application of aerodynamic effects.

6.1. Implementation of cylindrical structures

The phenomenological model described in Part I holds for single degree of freedom structures with a flat interaction surface. However, OWT monopiles and monopiles with many other applications are cylindrical structures. In this section the phenomenological model discussed in Part I, is extended with a cylidrical structure and lateral loading to accommodate the cylindrical cross-section of the OWT. Hence, lateral motion is can occur and is discussed. Firstly, a single degree of freedom cylindrical structure is investigated in subsection 6.1.1. Secondly, the implementation of lateral motion is discussed and a two degree of freedom structure is introduced in subsection 6.1.2. The implementation of buckling on a cylindrical structure is briefly discussed in subsection 6.1.4 and the section is concluded with a failure map of a cylindrical structure in subsection 6.1.5.

6.1.1. Longitudinal motion

Firstly, it is investigated what happens if the flat single DOF system described in the previous section would be circular. A schematic representation of a cylindrical structure in top view is given in Figure 6.1. It must be emphasized that due to the principle of contact area

variation, the contact area for each element must remain constant. The width of each element therefore depends on the angle at which it is in contact with the structure.

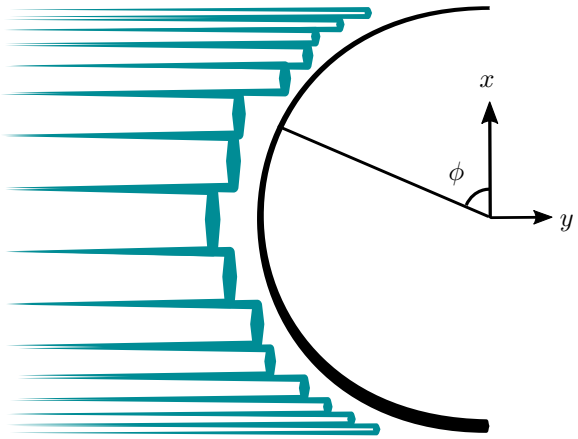

Figure 6.1: Top view drawing of creep-crushing elements approaching a cylindrical structure

To find the response of the structure the problem is simplified to the interaction between the structure and one creep-crushing element illustrated in Figure 6.2. The element approaches the structure and will make contact at a certain angle ϕ along the circumference. As the reaction of the cylindrical structure F_s is always normal to the tangent of the circle, the ice load can be split up in two components F_n and F_t. The components correspond to the normal ice load and the tangential ice load respectively. The normal and tangential component of the ice load can now be described as:

$$F_{n,i} = F_{\text{ice},i} \cdot \sin(\phi_i) \tag{6.1}$$

$$F_{t,i} = F_{\text{ice},i} \cdot \cos(\phi_i) \tag{6.2}$$

Where i denotes the number of the ice element, ϕ_i is the angle at the circumference as defined in Figure 6.1, and $F_{ice,i}$ is the ice force in ice element i. The normal ice load F_n and the reaction force F_s will now be in equilibrium. The tangential ice load suggests that the ice element will slide along the structure's surface. However, the pressure from the surrounding ice will prevent the loaded element from doing so, since a confined ice sheet is considered. Moreover, as the elements represent contact zones, it is assumed that the elements can not move in lateral direction. The reaction force from the surrounding ice F_{con} is therefore defined as equal and opposite to $F_{t,i}$. Friction can be of influence when considering cylindrical structures. However, the effect of friction is not included here and assumed zero.

$$F_{\text{con},i} = F_{t,i} \tag{6.3}$$
$$F_{s,i} = F_{n,i} \tag{6.4}$$

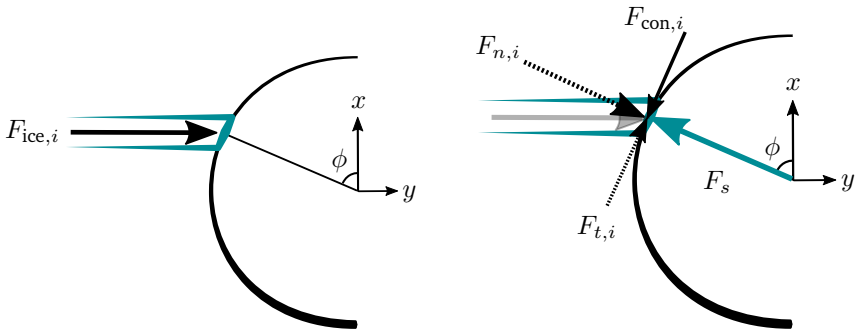

(a) Drawing of a single element interacting with a cylindrical structure

(b) Top view drawing of a decomposition of the local ice load into a normal and tangential component

Figure 6.2

The interaction with a cylindrical structure results in a reduction of the ice load in the direction of the ice velocity. To implement this effect in the numerical model, the reaction force in the Cartesian system as a function of the ice load $F_{ice,i}$ can be derived from Figure 6.2 as:

$$F_{s,x} = F_{\text{ice},i} \cdot \sin(\phi_i)\cos(\phi_i) \tag{6.5}$$
$$F_{s,y} = F_{\text{ice},i} \cdot \sin(\phi_i)^2 \tag{6.6}$$

Directly implementing this in the system of equations discussed in section 4.1 would result in a non-diagonal stiffness matrix, increasing the computational time. Therefore, the equilibrium in the contact point is investigated. All forces and components in the Cartesian system are shown in Figure 6.3. From Figure 6.3 the equilibrium equation in the y-direction can be determined and written as follows:

$$F_{s,y} = F_{\text{ice},i} - F_{\text{con},y} \tag{6.7}$$
$$M_s\ddot{u}_{s,y} + C_s\dot{u}_{s,y} + K_s u_{s,y} = K_3(u_3 - u_{s,y}) - K_3(u_3 - u_{s,y}) \cdot \cos^2(\phi_i) \tag{6.8}$$

Which is equal to Equation 6.6 since $\sin^2(\phi) = 1 - \cos^2(\phi)$. By writing the equilibrium equation as in Equation 6.7, the external reaction force introduced by the confinement of

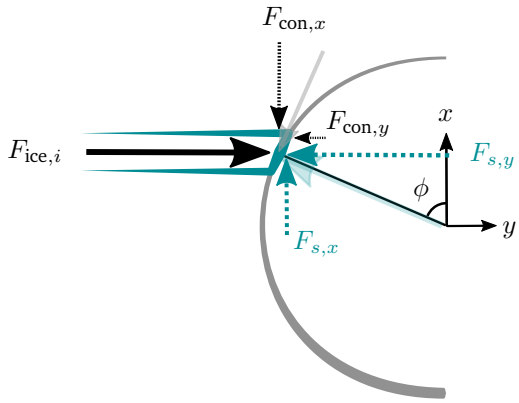

Figure 6.3: Top view drawing of all force components in the Cartesian system

the ice can be written as an external load. The system of equations described by Equation 4.20 can now be written for a cylindrical structure as follows:

$$\begin{bmatrix} M_s & 0 & 0 \\ 0 & 0 & 0 \\ 0 & 0 & 0 \end{bmatrix} \begin{bmatrix} \ddot{u}_{s,y} \\ \ddot{u}_{3,i} \\ \ddot{u}_{2,i} \end{bmatrix} + \begin{bmatrix} C_s & 0 & 0 \\ 0 & C_2 & -C_2 \\ 0 & -C_2 & C_1 + C_2 \end{bmatrix} \begin{bmatrix} \dot{u}_{s,y} \\ \dot{u}_{3,i} \\ \dot{u}_{2,i} \end{bmatrix} + \\ \begin{bmatrix} K_s + \sum_{i=1}^{N} K_{3,i} & -K_{3,i} & 0 \\ -K_{3,i} & K_2 + K_{3,i} & -K_2 \\ 0 & -K_2 & K_2 \end{bmatrix} \begin{bmatrix} u_{s,y} \\ u_{3,i} \\ u_{2,i} \end{bmatrix} = \begin{bmatrix} -\sum_{i=1}^{N} K_{3,i} \cdot (u_{3,i} - u_{s,y}) \cdot \cos^2(\phi_i) \\ -F_{\text{fric},i} \\ C_1 v_{\text{ice}} + F_{\text{fric},i} \end{bmatrix} \tag{6.9}$$

Where i denotes the number of the element and the complete system is assembled as was discussed in section 4.1.

6.1.2. Lateral motion

Due to the randomness of the locations of the creep-crushing elements, the longitudinal loading will not be symmetrical. Figure 6.3 shows that due to the cylindrical structure, a load in the x-direction is introduced. This will result in a lateral motion in the structure, if a degree of freedom in the x-direction would exist. This is a realistic effect of the interaction with a cylindrical structure and is therefore included in the phenomenological model. It must be noted that if the structure would move in lateral direction, the points at which the ice elements interact with the structure would change as well. However, this change is assumed to be small enough to be neglected.

The second degree of freedom of the structure will have the equal mass,damping, and stiffness as the first DoF. The reaction force at this DoF was already described in Equa-

tion 6.5 as $F_{s,x}$. The equilibrium in the x-direction of the interaction with a single element i therefore becomes:

$$M_s\ddot{u}_{s,x} + C_s\dot{u}_{s,x} + K_s u_{s,x} = K_{3,i}(u_{3,i} - u_{s,y}) \cdot \sin(\phi_i)\cos(\phi_i) \tag{6.10}$$

The system of equations described in Equation 6.9 can now be extended to a system that includes lateral motion:

$$\begin{bmatrix} M_s & 0 & 0 & 0 \\ 0 & M_s & 0 & 0 \\ 0 & 0 & 0 & 0 \\ 0 & 0 & 0 & 0 \end{bmatrix} \begin{bmatrix} \ddot{u}_{s,x} \\ \ddot{u}_{s,y} \\ \ddot{u}_{3,i} \\ \ddot{u}_{2,i} \end{bmatrix} + \begin{bmatrix} C_s & 0 & 0 & 0 \\ 0 & C_s & 0 & 0 \\ 0 & 0 & C_2 & -C_2 \\ 0 & 0 & -C_2 & C_1 + C_2 \end{bmatrix} \begin{bmatrix} \dot{u}_{s,x} \\ \dot{u}_{s,y} \\ \dot{u}_{3,i} \\ \dot{u}_{2,i} \end{bmatrix} +$$
$$\begin{bmatrix} K_s + \sum_{i=1}^{N} K_{3,i} & 0 & -K_{3,i} & 0 \\ 0 & K_s & 0 & 0 \\ -K_{3,i} & 0 & K_2 + K_{3,i} & -K_2 \\ 0 & 0 & -K_2 & K_2 \end{bmatrix} \begin{bmatrix} u_{s,x} \\ u_{s,y} \\ u_{3,i} \\ u_{2,i} \end{bmatrix} = \begin{bmatrix} \sum_{i=1}^{N} K_{3,i} \cdot (u_3 - u_{s,x}) \cdot \sin(\phi_i)\cos(\phi_i) \\ \sum_{i=1}^{N} -K_{3,i} \cdot (u_3 - u_{s,x}) \cdot \cos^2(\phi_i) \\ -F_{\text{fric},i} \\ C_1 v_{ice} + F_{\text{fric},i} \end{bmatrix} \tag{6.11}$$

Where i denotes the number of the element and the complete system is assembled as was discussed in section 4.1.

6.1.3. Side elements

When observing actual ice crushing against a structure, one would see that the structure leaves a trace in the ice. It also shows that because of this trace, ice exists along the sides of the structure. Since lateral motion is considered, the fact that ice exists along the side of the structure must be considered as well. The ice on the side limits the lateral motion to a certain extent, since a infinitely large ice sheet is assumed. However, to the author's knowledge there is no literature available on the effect of limited motion due to the ice on the sides.

Henceforth, the ice moving int the positive y-direction is denoted as 'approaching ice'. It is assumed that the ice along the sides of the structure behaves similar to as the approaching ice. With the exception, that the relative velocity is completely determined by the lateral velocity of the structure. This concept is modeled by placing creep-crushing elements, pointing in the positive and negative x-direction, along the sides of the structure. The elements are illustrated Figure 6.4 and denoted as 'side elements'.

The side elements can be divided into two zones. The first zone is the zone where the ice approaches the structure referred to as the 'frontal zone'. The second zone is where the ice leaves the vicinity of the structure, referred to as the 'rear zone'. Both zones will be discussed separately here.

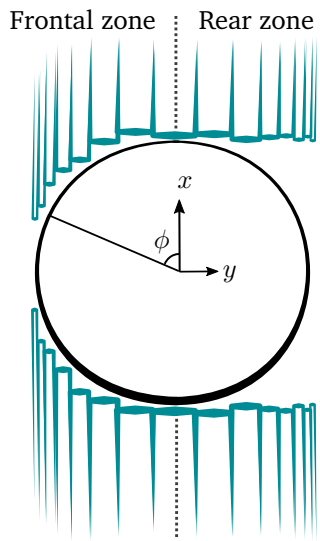

Figure 6.4: Drawing of the placement of side element and the division between the frontal and rear zone

Frontal zone

The major difference between the frontal and rear zone, is that the positions of the elements in the frontal zone depend on the contact between frontal elements and the structure. After all, a side element in the frontal zone cannot be in contact with the structure if its corresponding approaching element is not even in the vicinity. The side elements in the frontal zone are therefore coupled to the approaching elements as shown in Figure 6.5. The frontal and side elements that share a contact area on the structure form pairs using the following conditions:

- If the approaching element is in contact with the structure, its corresponding side element is also in contact and therefore set to the position of the structure.
- If the the approaching element or the side element fails, both elements are considered to fail.

Rear zone

Fortunately, the rear zone is less complicated. There are no frontal elements in the rear zone as they are being crushed on the other side. Furthermore, the side elements should not surround the structure as in reality a wake is formed behind the structure. Therefore, the elements follow a line equal to the diameter of the structure as shown in Figure 6.4.

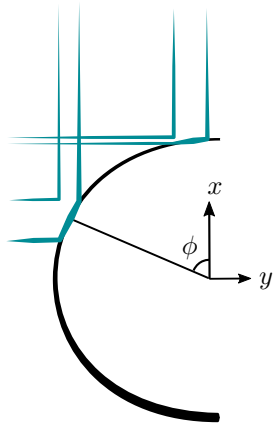

Figure 6.5: Coupling of the approaching and corresponding side element, in top view

Finally, it must be noted the ice moves with a velocity v_{ice} in the y-direction. This means that a side element is actually not staying in the same location. This effect is modeled by resetting the side element for every time step where the structure is moving away from, and is not in contact with the element.

6.1.4. Buckling

Kerr (1978) describes buckling to a cylindrical structure similar to a structure with a flat interaction surface. However, the assumed radial cracks arise in a different manner for cylindrical structures (Figure 3.6). As shown in Figure 6.6 radial cracks exist at $\phi = 0, \frac{\pi}{4}, \frac{\pi}{2}, \frac{3\pi}{4}$, and π.

The wedges on the side are neglected since loads on these wedges are not expected to reach the buckling load during realistic conditions. Therefore, only the two frontal wedges need to be considered for ice buckling against a cylindrical structure. These wedges are modeled in the same manner as is done for the flat structure discussed in section 4.3. However, the width of the ice sheet at interface, b_0, is not equal to the width of the structure and can be found as follows:

$$b_0 = \frac{1}{2} \cdot b \cdot \frac{\sin(\frac{\pi}{4})}{\sin\left(\frac{\pi}{8}\right)} \tag{6.12}$$

It must be noted that the loads on the wedges are not very straight forward to determine. They need to be calculated by summing the forces in the creep-crushing elements that are in contact with the structure at the location of a wedge. From these forces only the correct components should be summed, including the loads of the side elements.

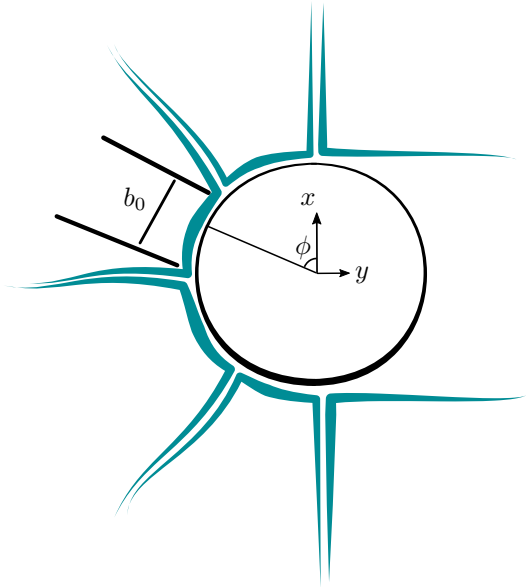

Figure 6.6: Top view of the floating wedges for a cylindrical structure

$$F_{\text{wedge}} = \sum_{j=1}^{N_{\text{wedge}}} F_{\text{ice,front},j} \cdot \cos(\frac{\pi}{8}) + F_{\text{ice,side},j} \cdot \sin(\frac{\pi}{8}) \tag{6.13}$$

Equation 6.13 shows how the total force applied to the wedge in the direction of the wedge, F_{wedge} is found. Here, $F_{\text{ice,front},j}$ is the force in the frontal element j and $F_{\text{ice,side},j}$ is the force in the corresponding side element j. Furthermore, N_{wedge} is the number of frontal elements that are part of the wedge, equal to the number of side elements that are part of the wedge. Since there are two wedges, the applied force must be found for each wedge separately.

6.1.5. Failure map of a cylindrical structure

To demonstrate the difference in behavior between a structure with a flat interaction surface and a cylindrical structure, a failure map is created for the extended model. The failure map is created with the same conditions as for the verification of the phenomenological model in subsection 5.3.9. To enable comparison between the two maps, they are shown together in Figure 6.7. Three major differences are observed and explained here.

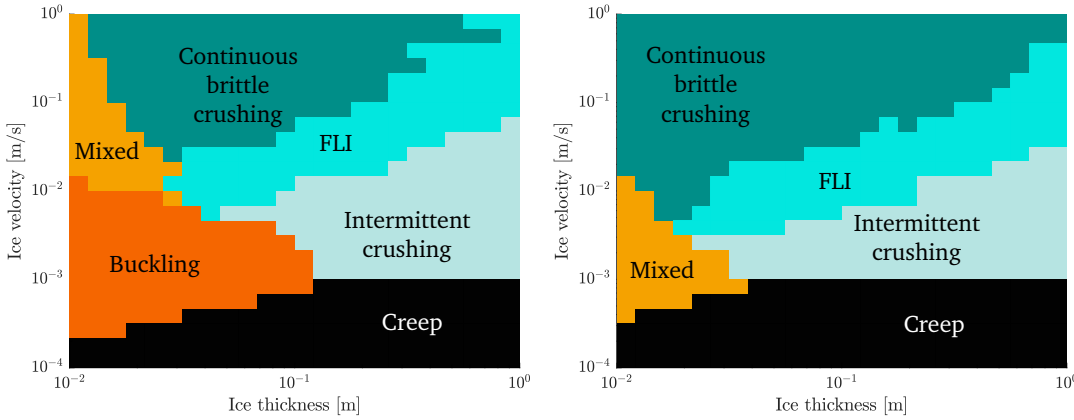

(a) Failure map for a structure with a flat interaction surface

(b) Failure map for a cylindrical structure

Figure 6.7

FLI occurs at lower ice velocities for cylindrical structures

The first observation from the map is that FLI occurs at lower ice velocities. This can easily be explained by the decrease in global ice load in the longitudinal direction due to the cylindrical shape of the structure. To understand this effect one must look at the definition for frequency lock-in.

FLI occurs with a loading and unloading phase. During the loading phase the relative velocity is close to the transition velocity for a certain amount of time. This amount of time is defined by a fraction of the period of a cycle, since it can only occur when the structure is close to it's maximum velocity and moving in the same direction as the ice.

During this time in the ductile regime, the relative velocity is low and thus the contact area increases, subsequently increasing the load. If FLI is to occur, this load needs to be enough to excite the structure into a maximum velocity that is close to the ice velocity. The maximum velocity is depending on the natural frequency of the structure and the ice load. If the frequency remains equal, and the load increases, the maximum velocity increases as well. Thus, if the global ice load is higher in general, FLI will occur at higher velocities and vice versa. This explains why FLI occurs at lower velocities for cylindrical structures.

Buckling occurs only at smaller ice thicknesses for cylindrical structures

The second observation is that buckling only occurs at smaller ice thicknesses. The reasoning behind this can be that for the same ice thickness, the aspect ratio $\frac{b_0}{h}$ has increased.

Since the ice sheet is divided in two wedges, b_0 is significantly smaller. A higher aspect ratio directly results in a higher flexural stiffness, making the wedge less vulnerable to buckling.

Pure buckling does not occur for cylindrical structures

The third observation is that pure buckling does not occur for cylindrical structures. This is considered as an effect of the way the wedges are modeled. When a wedge buckles, only the creep-crushing elements in the area of the wedges are reset. This leaves a number of frontal creep-crushing elements on the far side of the structure. The load generated by these elements is minimal. However, these elements are unable to buckle and thus will fail in crushing.

6.2. Structural model

One of the targets of this thesis is to apply the ice-structure interaction model to an OWT model in a realistic manner. A typical offshore wind turbine can be divided into 3 components:

1. The foundation structure
2. The tower
3. The rotor nacelle assembly (RNA)

Figure 6.8 shows a schematic representation of a typical OWT. In the model, the foundation structure is considered to be a monopile with a diameter of 6 meters at mean sea level. The tower is a compliant structure designed to carry the RNA at a height of approximately 100m above mean sea level (MSL). It must be emphasized that the OWT model is not the focus of this thesis and that the exact values used fore the structural model are confidential. The used model contains many details like appurtenances and therefore the responses created by the model is considered as a realistic representation of the OWT.

6.2.1. Support structure modes

The combination of the monopile and the tower is called the support structure. The support structure is modeled by a three dimensional finite-element model consisting of about 70 cylindrical Timoshenko beam elements with varying lengths, diameters, and wall-thicknesses. Details in the form of e.g. lumped masses are included to model appurtenances like boat landings, ladders, and flanges. Moreover, added mass from surrounding and entrained water are included.

The majority of the response is expected to occur in the first three longitudinal bending modes. To give the reader more insight into the properties of the structure, some important

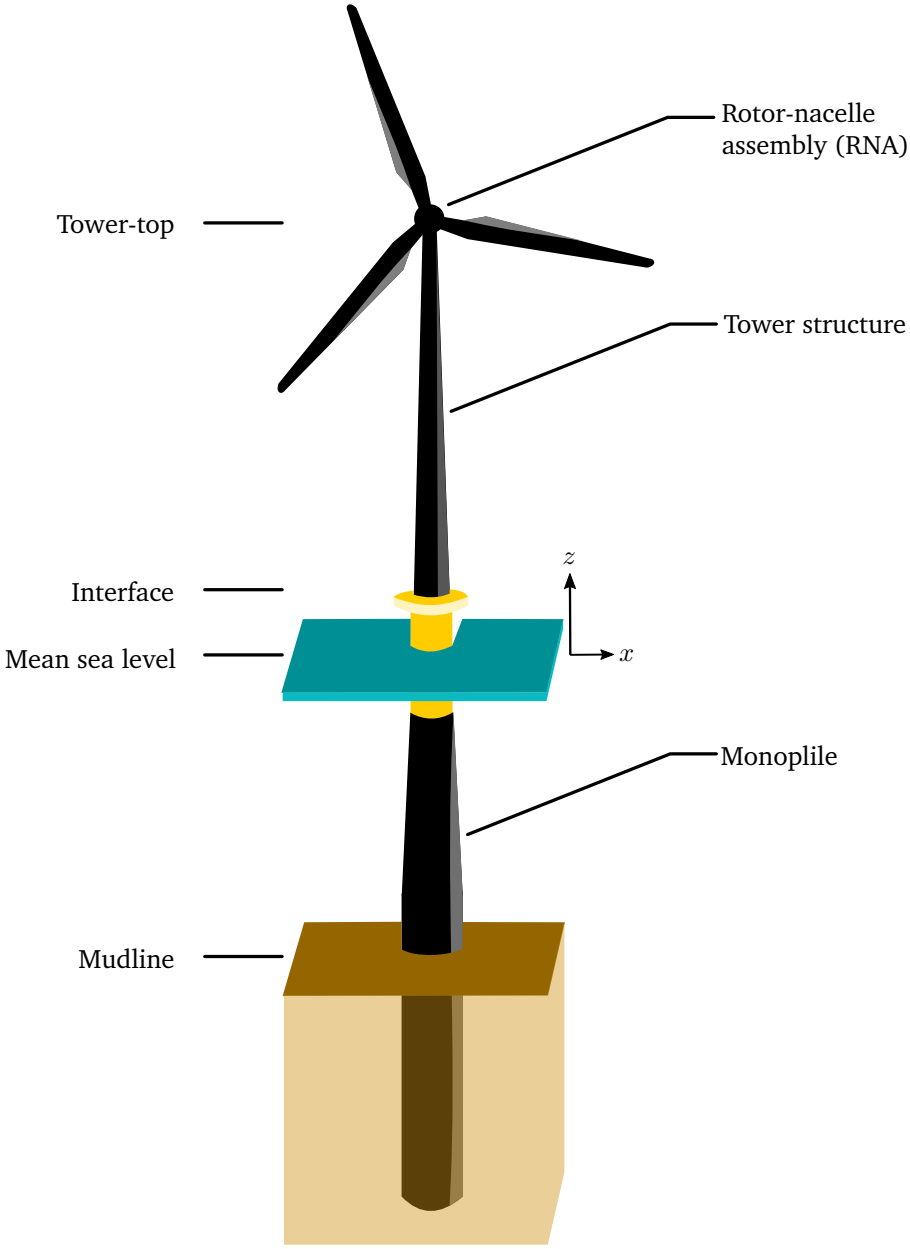

Figure 6.8: Schematic representation of a typical OWT

values on these modes are given here. The mode shapes of the structure are illustrated in Figure 6.9.

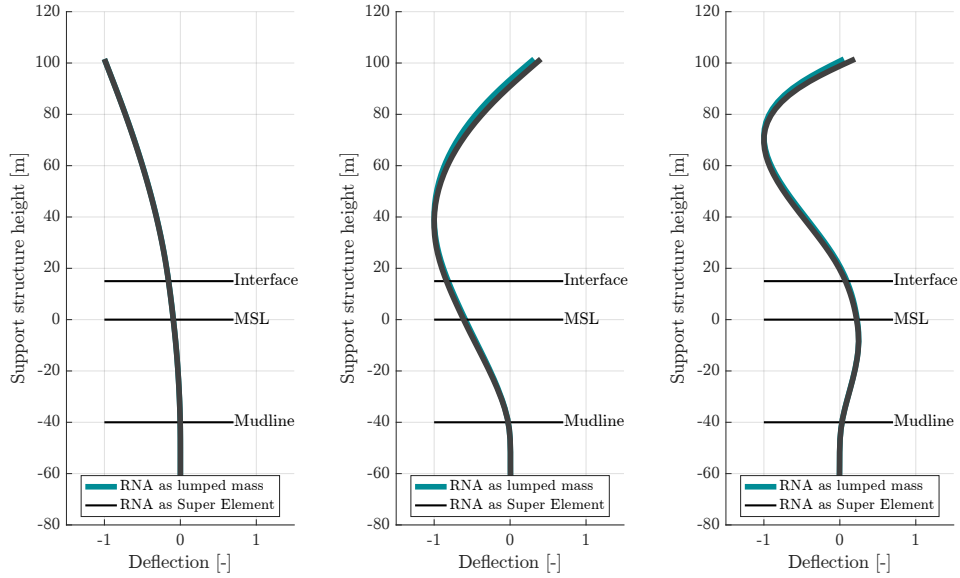

(a) First bending mode **(b)** Second bending mode **(c)** Third bending mode

Figure 6.9: Mode shapes of the first three bending modes, for the model where the RNA is modeled as a lumped mass a model where the RNA is modeled as a super element

The ice interaction takes place at MSL. In Figure 6.9 MSL is situated at $z = 0$. It can be observed that the modal amplitude at this location is different per mode. This means that the arm of an external load at $z = 0$ is different per mode as well and thus dependent on the mode shape amplitude. Table 6.1 shows the major values considering these modes.

6.2.2. RNA

For simplicity the RNA in the structural model is modeled as a lumped mass. This excludes any dynamics of the RNA, e.g. the modes in the blades. To include these RNA properties, the RNA can be modeled as a super element containing blade and nacelle modes. The super element is constructed from a free-floating RNA model based on BHawC. An adapted version of the Craig-Bampton reduction method is used to create a reduction basis. A detailed discussion on this topic is given by Van der valk (2014). This method is out of the scope of

Table 6.1: Values for the first three fore-aft bending modes of the structural model with a lumped mass RNA

Parameter	Symbol	1st mode	2nd mode	3rd mode	Unit
Mode shape amplitude at MSL	ϕ_{MSL}	0.09	0.59	0.23	-
Eigen frequency	f	0.20	0.95	2.1	Hz
Damping ratio	ζ	0.80	0.80	0.80	%
Modal mass	M^*	560	840	460	ton
Modal damping	C^*	11	79	94	kNs/m
Modal stiffness	K^*	0.92	30	76	MN/m

this thesis. However, the application of the super element is discussed here.

An important feature of the super element method is that the free floating RNA model now can be reduced to a smaller system of equations, and still can be applied to the structural model. To enable this, the DoFs of the RNA model are divided into internal DoFs and interface DoFs. Six interface DoFs are retained; three translational, and three rotational DoFs. Furthermore, a certain number N_{m} modes are included to describe the RNA dynamics. This results in the values given in Table 6.2, and the mode shapes illustrated in Figure 6.9.

Table 6.2: Values for the first three fore-aft bending modes of the structural model with the RNA super element

Parameter	Symbol	1st mode	2nd mode	3rd mode	Unit
Mode shape amplitude at MSL	ϕ_{MSL}	0.09	0.59	0.22	
Eigen frequency	f	0.21	0.97	2.1	Hz
Damping ratio	ζ	0.81	0.80	0.76	%
Modal mass	M^*	530	890	550	ton
Modal damping	C^*	11.4	85.1	103	kNs/m
Modal stiffness	K^*	0.92	32	85	MN/m

The difference shown between the structural model with a lumped mass, and the model with a super element as RNA, are caused by the differenct modeling of mass and stiffness in the RNA. From Figure 6.9 and Table 6.2 it can be concluded that the difference between the two models is relatively small.

6.2.3. Soil

The soil is modeled by a distributed stiffness generated from a p-y curve. The p-y curve is a representation of the lateral soil stiffness over the depth of the soil. As softening effects

occur, the p-y curve will change with increasing deflection. However, a detailed discussion is out of the scope of this thesis. Therefore a choice was made to consider the soil as linear over the deflection of the monopile. A single stiffness value is thus used for the entire simulation.

The soil stiffness is applied to the structural model by integrating the distributed stiffnesses over the shape functions of the beam elements. The same method was used to apply the distributed Winkler stiffness to the buckling wedge in section 4.3.

6.3. Aerodynamic effects

During the operation of the OWT, drag and lift forces induce loads on the wind turbine. These loads result in an external load and aerodynamic damping. To model these aerodynamic effects, wind load and aerodynamic damping are discussed separately in this section. First, a look is taken at the application of wind loading via thrust, followed by the implementation of aerodynamic damping.

6.3.1. Wind-induced loading

The OWT has the ability to pitch its blades, increasing or decreasing the lift force generated by the wind. This is done to prevent the rotor from rotating at too high velocities which would cause severe damage. The wind speed experienced by the OWT can therefore be recognized by three important values:

1. Cut-in wind speed: the lowest wind speed at which the OWT produces electricity (around 3m/s).
2. Rated wind speed: the wind speed at which the OWT start pitching its blades to remain at a constant rotation velocity (around 10m/s).
3. Cut-out wind speed: the wind speed at which the OWT stops producing electricity to prevent failure (around 32m/s).

The longitudinal force that results from the dynamic effects is referred to as the Thrust. The thrust is dependent on the pitch of the rotor blades and the rotational velocity, which are directly related to the wind speed. Figure 6.10 shows an example of a thrust curve used to determine the thrust depending on the wind velocity. The thrust curve is defined by Equation 6.14.

$$F_{\mathrm{w}}(V_{\mathrm{w}}) = C_{\mathrm{T}}(V_{\mathrm{w}})\frac{1}{2}\rho_{\mathrm{a}}V_{\mathrm{w}}^2 A \tag{6.14}$$

Here, F_{w} is the load created by the wind during production and C_{T} is the thrust coefficient which is a property of the RNA and a function of the wind velocity V_{w}. In a coupled

model this velocity would be the relative velocity between the wind and the structure. However, aerodynamic coupling is neglected in this model. Furthermore, ρ_a is the density of air and A is the total rotor area. The wind loading is applied at the RNA in the direction of the ice velocity.

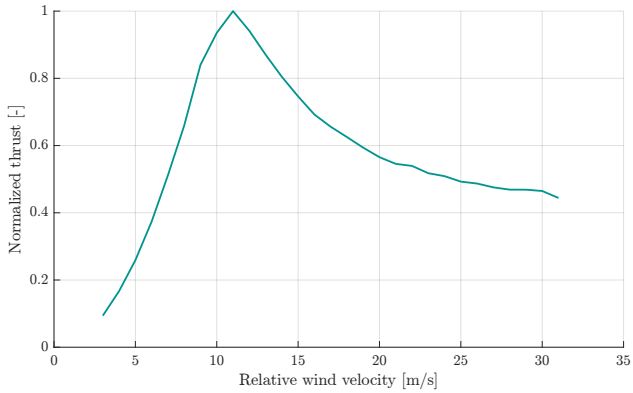

Figure 6.10: Example of thrust curve

The wind velocity applied during the simulations for the study in the next chapter is a time series including turbulence. This is done to include a realistic effect of external wind loading. To give the reader some insight in the proportions of this turbulence an example of a wind velocity time series is given in Figure 6.11

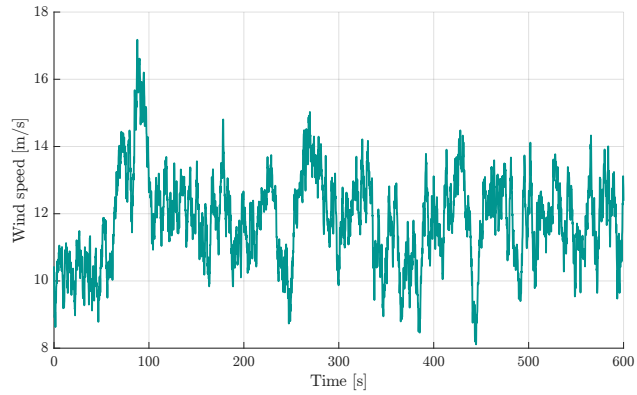

Figure 6.11: Example of wind velocity time series

6.3.2. Aerodynamic damping

Aerodynamic damping is an effect caused by the longitudinal velocity at tower top. The longitudinal motion at tower top results in a change in relative velocity between the rotor blades and the wind. Due to aerodynamic effects, this change in relative velocity results in an increased drag and lift component in the direction opposite to the motion of at tower top. The aerodynamic damping ratios per mode, $\zeta_{\text{aero},i}$, can therefore be plotted over the wind velocity.

Next, the aerodynamic damping matrix is now created from a matrix containing the aerodynamic damping ratios per mode $\boldsymbol{\zeta}_{\text{aero}}$ on its diagonal. First, modal the damping ratios are determined using the mean wind velocity of the simulation. Secondly, the modal mass matrix and the modal stiffness matrix are determined from the structural model. This requires the eigen matrix of the structure and therefore first the eigenvalue problem has to be solved. For an undamped free vibrating structure the following equation of motion holds:

$$\boldsymbol{M}\ddot{\boldsymbol{u}} + \boldsymbol{K}\boldsymbol{u} = \boldsymbol{0} \tag{6.15}$$

Where $\boldsymbol{M}$ is the mass matrix of the structure, $\boldsymbol{K}$ is the stiffness matrix of the structure, and $\boldsymbol{u}$ is the deflection vector. A solution to this problem can be written in a sum of modes:

$$\boldsymbol{u}(t) = \sum_{i=1}^{n} \boldsymbol{\phi}_i \cdot \eta_i(t) \tag{6.16}$$

Here, $\boldsymbol{\phi}_i$ is the eigen vector of mode i and η_i is the corresponding modal amplitude as a function of time. The eigen vector is a solution to the eigenvalue problem below:

$$(-\omega_i^2 \boldsymbol{M} + \boldsymbol{K})\boldsymbol{\phi}_i = \boldsymbol{0} \tag{6.17}$$

Where ω_i is the eigen frequency of mode i. The eigen vectors and eigen frequencies can be found for each mode separately. Equation 6.16 can be rewritten as:

$$\boldsymbol{u}(t) = \boldsymbol{\Phi} \cdot \boldsymbol{\eta}(t) \tag{6.18}$$

Where $\boldsymbol{\Phi}$ is the eigen matrix consisting of all eigen vectors stacked in the columns of the matrix:

$$\boldsymbol{\Phi} = [\boldsymbol{\phi}_1, \boldsymbol{\phi}_2, ...\boldsymbol{\phi}_n] \tag{6.19}$$

And $\boldsymbol{\eta}$ is a vector containing the modal amplitudes of each mode as a function of time. When unit modal mass is assumed it follow that:

$$\boldsymbol{\Phi}^T \boldsymbol{M} \boldsymbol{\Phi} = \boldsymbol{I} \tag{6.20}$$

$$\boldsymbol{\Phi}^T \boldsymbol{K} \boldsymbol{\Phi} = \boldsymbol{\Omega}^2 \tag{6.21}$$

Where, $\boldsymbol{M}$ and $\boldsymbol{K}$ are the mass and stiffness matrix of the structural model respectively. Furthermore, $\boldsymbol{I}$ is the identity matrix and $\boldsymbol{\Omega}$ is a matrix with the eigen frequencies of the model on its diagonal. By pre-multiplying of Equation 6.20 by $\boldsymbol{M\Phi}$ and post-multiplying Equation 6.20 by $\boldsymbol{\Phi}^T\boldsymbol{M}$ two equations are found:

$$\boldsymbol{M\Phi\Phi}^T\boldsymbol{M\Phi} = \boldsymbol{M\Phi} \tag{6.22}$$

$$\boldsymbol{\Phi}^T\boldsymbol{M\Phi\Phi}^T\boldsymbol{M} = \boldsymbol{\Phi}^T\boldsymbol{M} \tag{6.23}$$

From Equation 6.22 and 6.23 it now can be concluded that:

$$\boldsymbol{M\Phi\Phi}^T = \boldsymbol{\Phi\Phi}^T\boldsymbol{M} = \boldsymbol{I} \tag{6.24}$$

Furthermore, the aerodynamic damping matrix $\boldsymbol{C}_{\text{aero}}$ is defined as:

$$\boldsymbol{\Phi}^T\boldsymbol{C}_{\text{aero}}\boldsymbol{\Phi} = 2\boldsymbol{\Omega\zeta}_{\text{aero}} \tag{6.25}$$

By pre-multiplying Equation 6.25 by $\boldsymbol{M\Phi}$ and the post-multiplying it by $\boldsymbol{\Phi}^T\boldsymbol{M}$, it follows that:

$$\boldsymbol{M\Phi\Phi}^T\boldsymbol{C}_{\text{aero}}\boldsymbol{\Phi\Phi}^T\boldsymbol{M} = \boldsymbol{M\Phi}2\boldsymbol{\Omega\zeta}_{\text{aero}}\boldsymbol{\Phi}^T\boldsymbol{M} \tag{6.26}$$

From Equation 6.24 the aerodynamic damping matrix is now found:

$$\boldsymbol{C}_{\text{aero}} = \boldsymbol{M\Phi}2\boldsymbol{\Omega\zeta}_{\text{aero}}\boldsymbol{\Phi}^T\boldsymbol{M} \tag{6.27}$$

Assuming that the aerodynamic damping does not change the mode shapes or eigen frequencies of the model, it can be applied by simply adding the aerodynamic damping matrix to the existing structural damping matrix. It must be noted that $\boldsymbol{C}_{\text{aero}}$ is not diagonal, significantly increasing the computational time.

6.4. Chapter summary

In the second part of this thesis, the phenomenological model was applied to a structural model of an OWT and investigated in a case study. For the implementation of the structural model, firstly the phenomenological model for ice-structure interaction was adjusted for cylindrical structures. The adjustments involved a reduction in the longitudinal ice-load and the introduction of lateral loading. Moreover, lateral dynamics were implemented and a comparison was made to the phenomenological model discussed in Part I.

The structural model was described by a three dimensional finite-element model, consisting of Timoshenko beam elements. Moreover, an RNA super element was used to include

the dynamics of the rotor-nacelle assembly. The model includes multiple appurtenances and added mass from entrained water. The structural model was therefore considered as a realistic representation of an offshore wind turbine.

Aerodynamic damping and thrust have been included to enable simulations of the ice-structure interaction during production. The thrust was found from a wind speed-time series and a thrust curve that is dependent on the wind speed.

Chapter 7
Results of the coupled model

The model described in the previous chapter is put to the test of generating results. The results generated by this model are considered to describe realistic behavior of an offshore wind turbine as it interacts with floating level ice. Therefore, the behavior is identified for a few specific cases in this chapter, to enable a comparison with uncoupled modeling in the next chapter.

First, an evaluation is given on the methods used to visualize the simulation results in section 7.1. The second and third chapter include discussions on the results of two separate cases.

1. The first case considers the ice as the only environmental load in section 7.2;

2. The second case considers both ice and wind loads in section 7.3.

7.1. Visualisation of simulation results

Prior to a discussion of the results of the coupled model, an elaboration is given on the methods that were used to visualize the results. In the following two chapters the simulation results are visualized using three separate approaches. The first approach considers the energy in the OWT. To enable identification of the ice-structure interaction behavior, potential and kinetic energy in the structure are evaluated per mode. It must be noted that this excludes any rotation effects in the rotor. Furthermore, a measure of fatigue damage is used to show the potential effect of coupled and uncoupled modeling. Thirdly, the energy and fatigue damage plots are supported by time signals of specific simulations. To enable the reader to gain a better understanding on the meaning of these plots, the corresponding computation techniques are elaborated here.

7.1.1. Modal contribution

To determine the extent of dynam ics in the response, the ratio between mean potential and mean kinetic energy $\frac{E_p}{E_k}$ is computed. A ratio of 1 means that resonance occurs, since potential and kinetic energy are equally exchanged. Furthermore, to investigate in which structural modes the dynamics occur, the mean kinetic energy E_k is broken down into modal contributions. In order to compute these values over a range of ice and wind velocities, the mean potential and mean kinetic energy are computed for each simulation as follows.

It is assumed that the time signal of the deflections of the structure $\boldsymbol{u}(t)$ is described the structural modes and their corresponding modal amplitudes:

$$\boldsymbol{u}(t) = \Phi \cdot \boldsymbol{\eta}(t) + \boldsymbol{r}(t) \tag{7.1}$$

This process to obtain Φ was discussed earlier in subsection 6.3.2 and is not repeated here. Furthermore, $\boldsymbol{r}$ is the residual since it is assumed that Φ does not contain all mode of the structure. By definition $\boldsymbol{r}$ is orthogonal to the space of the modes:

$$\Phi \cdot \boldsymbol{r}(t) = \boldsymbol{0} \tag{7.2}$$

Hence, by pre-multiplying both side of the equations by Φ^T:

$$\Phi^T \boldsymbol{u}(t) = \Phi^T \Phi \boldsymbol{\eta}(t) \tag{7.3}$$

The next step is to determine the modal amplitude and modal velocity using the pseudo inverse. This is a projection of the modes to the actual response, and there represents the modal amplitude and modal velocity of each mode separately.

$$\boldsymbol{\eta}(t) = (\Phi^T \Phi)^{-1} \cdot \Phi \cdot \boldsymbol{u}(t) \tag{7.4}$$

$$\dot{\boldsymbol{\eta}}(t) = (\Phi^T \Phi)^{-1} \cdot \Phi \cdot \dot{\boldsymbol{u}}(t) \tag{7.5}$$

Where $\boldsymbol{u}$ and $\dot{\boldsymbol{u}}$ are the physical deflection and velocity vectors over time respectively. Furthermore, $\boldsymbol{\eta}$ and $\dot{\boldsymbol{\eta}}$ are an approximation of the modal amplitude and modal velocity vectors respectively, containing the corresponding values for each mode. Furthermore, the modal mass matrix and the modal stiffness matrix are found as:

$$\boldsymbol{M}^* = \Phi^T \boldsymbol{M} \Phi \tag{7.6}$$

$$\boldsymbol{K}^* = \Phi^T \boldsymbol{K} \Phi \tag{7.7}$$

Where $\boldsymbol{M}$ is the mass matrix and $\boldsymbol{K}$ is the stiffness matrix of the structure. The potential and kinetic modal energies can now be found as follows:

$$E_p(t) = \frac{1}{2} \cdot \eta_i(t) \cdot K_i^* \cdot \eta_i(t) \tag{7.8}$$

$$E_k(t) = \frac{1}{2} \cdot \dot{\eta}_i(t) \cdot M_i^* \cdot \dot{\eta}_i(t) \tag{7.9}$$

Where E_{p_i} and E_{k_i} are the potential and kinetic energy of mode i over time respectively. K_i^* and M_i^* are the modal stiffness and modal mass of mode i, and found from the diagonal of the modal mass and modal stiffness matrix. Furthermore, η_i and $\dot{\eta}_i$ are modal amplitude and modal velocity of mode i. The mean value of the energies is used, resulting in the mean potential and mean kinetic energy per mode, per time simulation.

7.1.2. Damage equivalent load (DEL)

The results of simulations are compared over a range of ice, and wind velocities. To visualize the simulations over these ranges, it is convenient to represent a specific simulation at a certain velocity in one data point. It is chosen to represent the simulations by the fatigue load in the structure. This parameter is also convenient since it is a design driving factor in OWT engineering.

Fatigue damage represents the damage gained by repetitive loading of a structure. In fatigue analyses 'S-N curves' are often used to indicate how many cycles N, at a certain stress S, the material can endure before failure. However, the method used here does not make use of the stress in the structure but immediately translates the response to a load value with equivalent fatigue damage. This value is referred to as the Damage Equivalent Load (DEL). The DEL represents the amplitude of the internal bending moment that will result a value for fatigue damage, equal to when the structure is loaded for the number of reference cycles.

Since fatigue damage varies over the height of the support structure one location is chosen to compare the DEL values. The highest bending moments are expected to occur close to the seabed and therefore mudline is chosen for computation of the DEL. The DEL at this location is calculated from the dynamic response. First, the internal bending moment over time is derived from the displacements. Since the structural model consists of beam elements, the internal responses in the structure can be found from the element stiffness matrix.

$$\boldsymbol{F}_{\text{int},i}(t) = \boldsymbol{K}_{\text{el},i} \cdot \boldsymbol{u}_i(t) \tag{7.10}$$

Where $\boldsymbol{F}_{\text{int},i}$ is a 12×1 vector containing the internal static responses of element i. Furthermore, $\boldsymbol{K}_{\text{el},i}$ is the 12×6 element stiffness matrix, and $\boldsymbol{u}_i$ the 12×12 deflection vector of beam element i.

Since uni-directional loading in y-direection is considered, solely the bending moment around the x-axis is required. This response is related to a single DoF in the element and can therefore be extracted from $\boldsymbol{F}_{\text{int},i}$. The data of the internal bending moment $M(t)$ consists of cycles varying in amplitude. This data is then processed to determine the fatigue damage using the rainflow cycle counting method (Matsuiski and Endo, 1969). The details of this method are outside of the scope of this thesis. It sufficient to the reader to understand that the method divides the amplitudes into ranges, and counts the amount of cycles occurring per amplitude range. The total damage can then be found by applying Palmgren-Miners Rule(Freebury and Musial, 2000):

$$D = \sum_{i=1}^{j} \frac{n_i}{N_i} \tag{7.11}$$

Where D is the damage as a fraction of the failure damage, i is the index number of the range and j is the total number of ranges. Furthermore, n_i is the number of load cycles in range i and N_i is the maximum number of cycles before failure, defined by the S-N curve Veldkamp (2006). The damage is then translated to a equivalent bending moment at 1Hz:

$$\text{DEL} = \left(\frac{D}{t_{\text{max}}} \right)^{\frac{1}{m}} \tag{7.12}$$

Where m is the Wohler coefficient determining the slope of the S-N curve, and t_{max} is the simulation time in seconds. It must be emphasized that the DEL is used in this thesis to compare the results between the coupled and the uncoupled model. The DEL will not be used to clarify specific behavior of the ice-structure interaction.

7.2. Results of the coupled model for ice-only

The first case study is based on a model where solely ice interacts with the structure, i.e. no other external load is applied. The dynamic effects induced by the ice are investigated by varying the ice velocity. Furthermore, the RNA super element, as described in section 6.2, is used to model the RNA of the OWT. The simulation conditions are described in Table 7.1.

Table 7.1: Properties used for the assessment of dynamic effects of ice velocity

Parameter	**Symbol**	**Value**	**Unit**
Ice thickness	h	0.4	m
Ice velocity	v_{ice}	1-250	mm/s
Number ice velocities	N_{sim}	59	#
Simulation time	t_{sim}	600	s
Initialization time	t_{ini}	50	s
Time step size	Δt	0.01	s

To exclude the influence of the initial conditions, the first 50 seconds are excluded from each time signal. The focus of this section is to gain a high level insight into the dynamic ice-structure interaction. Therefore, solely the most interesting data is described, of which conceivable clarifications are discussed.

7.2.1. Modal contribution

The ratio between kinetic and potential energy is given in Figure 7.1. Furthermore, the contribution of the first three modes, is visualized in Figure 7.2. The data is observed of which the findings are discussed next.

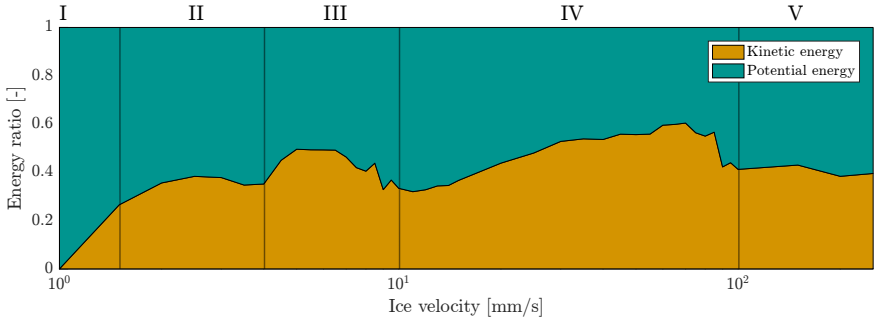

Figure 7.1: Ratio between mean kinetic and potential energy per ice velocity

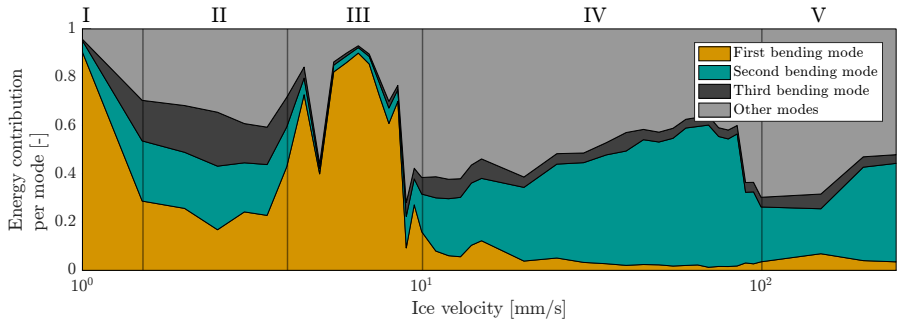

Figure 7.2: Modal contribution to the kinetic energy

I At an ice velocity of **1 mm/s** the contribution of the kinetic energy appears to be close to zero. Furthermore, the first bending mode shows to be dominant. This can be clarified by the fact that creep failure is the expected failure mode at this velocity. Creep at constant ice velocity ultimately results in a quasi-static deflection, forcing the OWT into a shape similar to the mode shape of the first mode.

II At ice velocities from **1.5 mm/s to 4 mm/s** the contribution of the kinetic energy increases. Moreover, the energy appears to be divided over the modes. This indicates that dynamic behavior is apparent in multiple frequencies. The observations can be clarified by the occurrence of intermittent crushing in this range of ice velocities. The reader is reminded that intermittent crushing is characterized by a loading and a unloading phase. After the rapid unloading, the structure is able to vibrate in its natural frequencies. In this case it seems that this vibration is covered by the first three bending modes, for about 65%.

III At ice velocities from **5 mm/s to 10 mm/s** the ratio between kinetic and potential energy is close to 1:1. This indicates resonance, since potential and kinetic energy are equally exchanged. Furthermore, a clear peak in the kinetic energy contribution of the first bending mode is observed. From the combination of these observations it can be concluded that resonance is apparent in the first bending mode. To determine if this resonance relates to FLI, the time signal of the simulation at 5 mm/s is investigated next.

To gain a better understanding of the actual ice-structure interaction, the deflection time signal at MSL is compared to the global ice load and the relative velocity between the ice and the structure in Figure 7.3.

A qualitative observation of the signal suggests that intermittent crushing occurs; a loading phase until a maximum is reached followed by a sudden drop. When comparing this to the global ice load signal, the same can be observed. To confirm that FLI is not the reason for the resonance, the phase diagram of the time series in Figure 7.3 is shown in Figure 7.4(a).

Despite the fact that resonance is clearly observed in Figure 7.1, Figure 7.4(a) confirms the absence of FLI, since there is no dynamic equilibrium at MSL. An explanation for this phenomenon is that the mode shape amplitude of the first bending mode at MSL is so small, the motion of this mode is not significantly noticeable in the velocity at MSL. Therefore, the first bending mode hardly affects the relative velocity. The apparent regime remains to be intermittent crushing, while the structure is loaded in the eigen frequency of the first bending mode. The latter results in resonance.

IV From **10 mm/s to 100 mm/s** the ratio between kinetic and potential energy seems to increase to 0.5, after a small drop. The contribution of the first bending mode has drastically decreased and the contribution of second bending seems to have taken over. The second bending mode remains dominant until a peak is reached at about 85 mm/s. Since the energy ratio is close to 1:1, resonance is expected, which is further investigated using a plot of the time series.

Figure 7.5 shows the full time series at an ice velocity of 85 mm/s. From this, it can be concluded that the resonance behavior does not have a constant amplitude. In this particu-

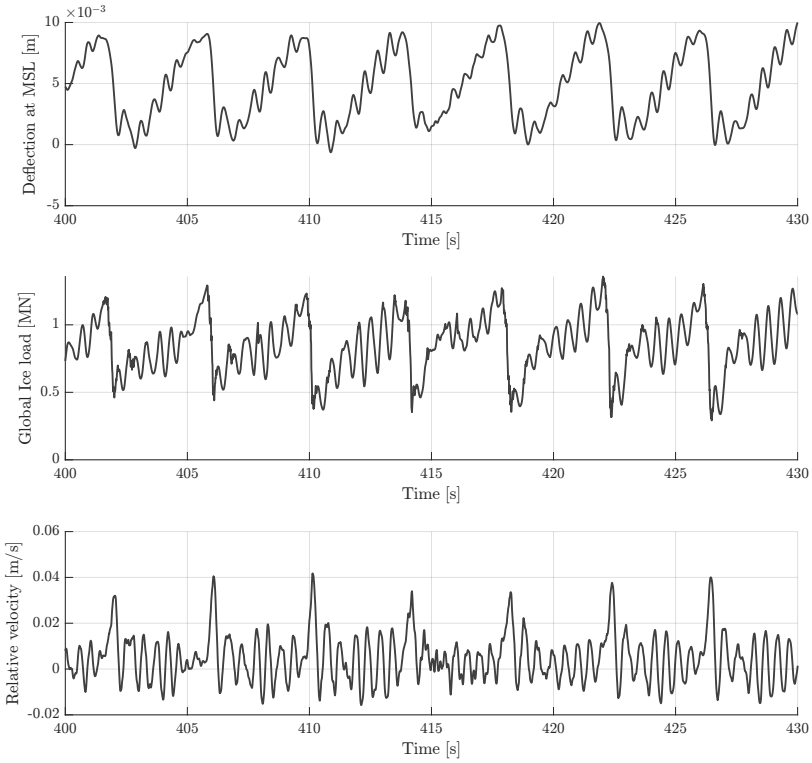

Figure 7.3: From top to bottom: Structural deflection at MSL, global ice load, and relative velocity between the ice and the structure. The ice velocity is equal to 5 mm/s

lar case an event concentrates around $t = 300s$ and lasts for nearly a minute. This event is investigated by comparing the deflection time signal at MSL to the global ice load and the relative velocity in Figure 7.6.

In Figure 7.6 the deflection at MSL shows harmonic behavior at a single frequency. It is also shown that the relative velocity becomes negative during the cycles. This suggest that FLI occurs, hence the phase diagram for the time series at 85 mm/s is shown in Figure 7.4(b).

The phase diagram cleary shows that a dynamic equilibrium has been reached at MSL. From these observations, Figure 7.1, and Figure 7.2, it is therefore concluded that FLI occurs in the second bending mode during an event in the simulation at 85 mm/s.

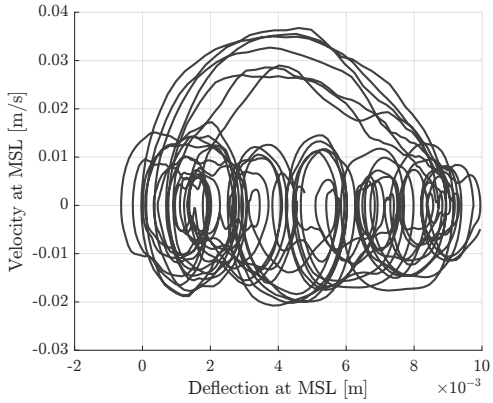

(a) Phase diagram for time series at 5 mm/s, shown in Figure 7.3

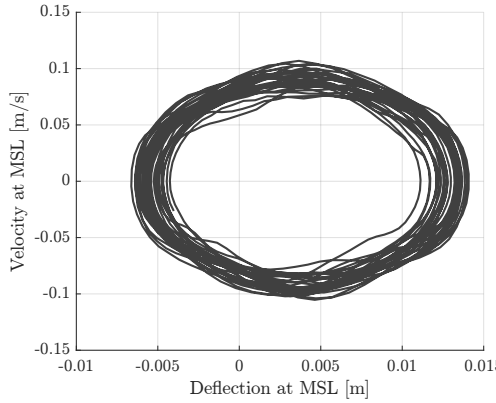

(b) Phase diagram for time series at 85 mm/s, shown in Figure 7.6

Figure 7.4

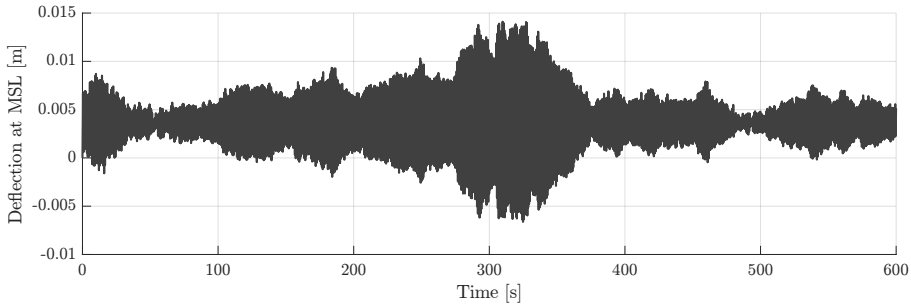

Figure 7.5: Deflection at MSL for the full 600s simulation, including the 50s initialization

V For ice velocities **higher than 100 mm/s** the ratio between kinetic and potential energy is relatively smaller. Furthermore, other modes beside the first three bending modes dominate the contribution to the kinetic energy in the OWT. This can be explained by continuous brittle crushing occurring at higher ice velocities. Furthermore, Figure 7.2 shows that the contribution of the second bending mode remains relatively large. This can be explained by the proportion of the mode shape amplitude at MSL. A larger mode shape amplitude at the location where the load is applied, allows for more energy to be transferred from the ice to the structure. Since the the mode shape amplitude of the second bending mode is the largest of the three, most energy will go to this mode during quasi random loading.

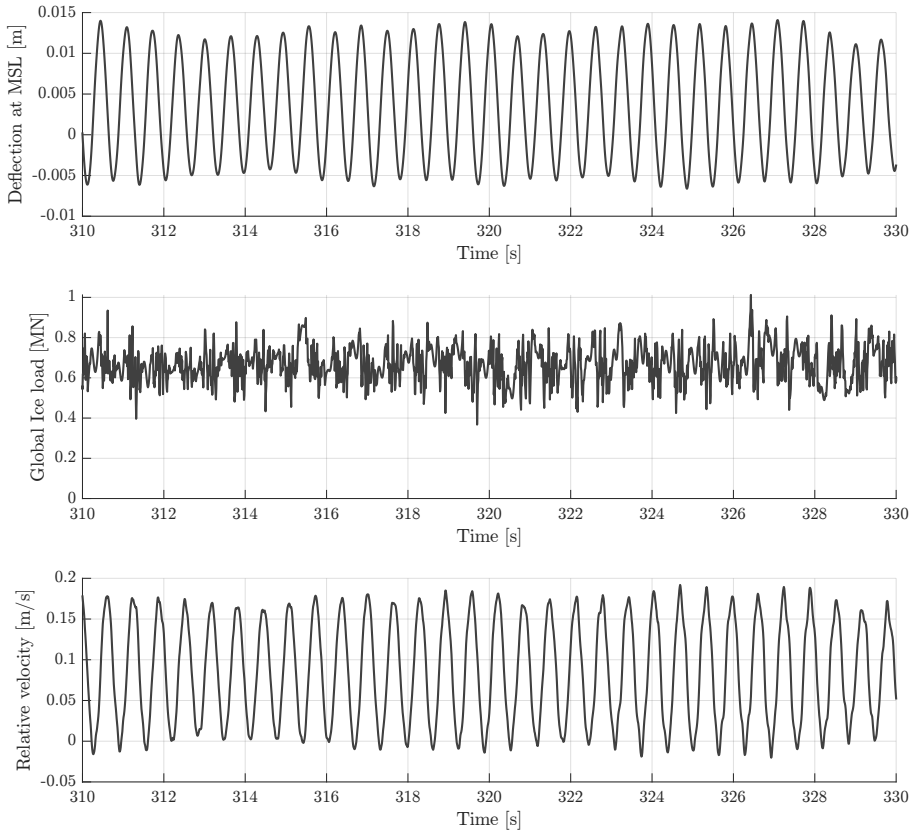

Figure 7.6: From top to bottom: Structural deflection at MSL, global ice load, and relative velocity between the ice and the structure. The ice velocity is equal to 85 mm/s

7.2.2. DEL at mudline for the ice-only reference case

The ice velocity range is divided into five velocity ranges. These ranges will be related to the behavior discussed above. Figure 7.7 shows the DEL over a range of 59 ice velocities, of which its relation to the ice-structure interaction behavior is discussed next.

I At an ice velocity of **1 mm/s** the DEL is lowest. This is explained by the quasi-static behavior of creep.

II From **1.5 mm/s to 4 mm/s** the DEL gradually decreases. These velocities are related to

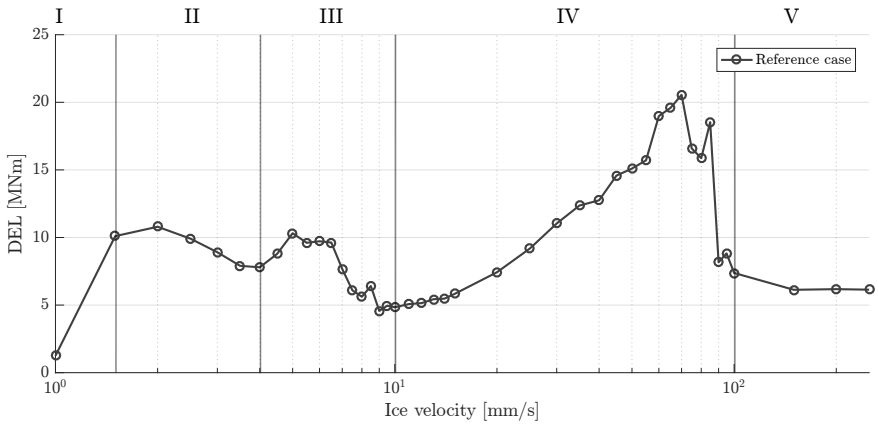

Figure 7.7: DEL for reference case at **mudline**, the circles indicate the separate simulations

intermittent crushing. The maximum amplitude during intermittent crushing decreases with increasing ice velocity, decreasing the bending moment at mudline.

III From **5 mm/s to 10 mm/s** a small peak is visible in the DEL. This peak is related to the resonance in the first bending mode.

IV From **10 mm/s to 100 mm/s** a large peak in DEL can be observed. This peak is related to the FLI in the second bending mode.

V For ice velocities **higher than 100 mm/s** the DEL seems to be relatively low. This is related to continuous brittle crushing occurring at high ice velocities. The mean amplitude during continuous brittle crushing is relatively low, resulting in a lower bending moment.

7.2.3. Seed sensitivity

The failure of the ice is modeled such, that it includes a random distribution for the initial deflection of a new ice element. The implementation of this distribution is discussed in section 4.1. The uniform distribution introduces a certain amount of randomness to the model, resulting in differences between simulations with identical input parameters. These different realizations are referred to as 'seeds'. This subsection elaborates on the effects caused by the different seeds. The obtained data is visualized in Figure 7.8 as follows:

- The DEL data of the reference case combined with the DEL data of an extra seed for every ice velocity (grey dots).
- A line fitted as the mean of the two seeds at each ice velocity
- Four added seeds at specific ice velocities (black diamonds).

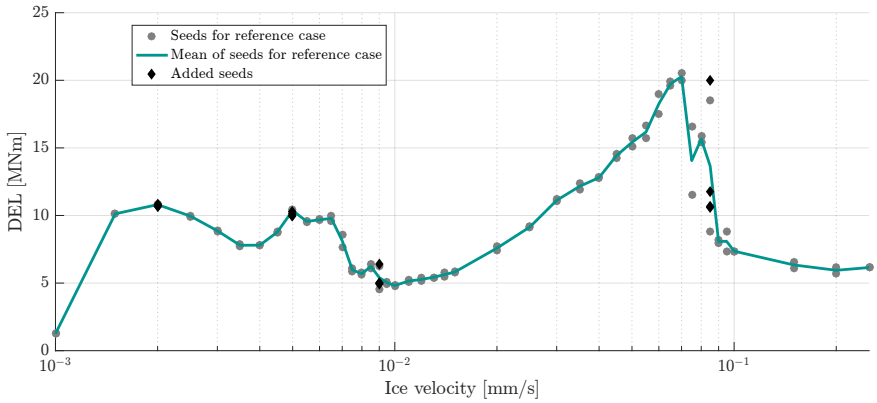

Figure 7.8: Normalized DEL for different seeds at mudline

In general it can be concluded that the results from the seeds stay within a range of 10% from each other, except for the values on the right side of the resonance peaks. An explanation for the large differences is that these ice velocities are in the transition zone between resonance and no resonance. E.g. the resonance at 85 mm/s seems to occur at events as was shown in Figure 7.5. The occurrence of such an event has a large influence on the DEL. It is therefore concluded that for practical application of the model, multiple seeds are required to obtain a reliable DEL. For now, the ice velocities in the range of this transition will not be included in further conclusions.

7.3. Results of the coupled modeling of ice and wind loads

During the simulations of the coupled model with combined ice and wind loading, the ice load is modeled in a coupled sense while a thrust load is applied as an external load signal at tower top. The values that were used during the simulations are equal to the ice-only case and given in Table 7.2.

In this section the data from the coupled ice and wind case is discussed and compared to the ice-only case. Conceivable explanations for the observed behavior are given to acquire insight on the proportion of both ice and aerodynamic effects. For obvious reasons the aerodynamic influence on the model is highly dependent on the wind velocity. The thrust is relatively low in the vicinity of cut-in wind speed, and has a peak in the vicinity of the rated wind speed as discussed in section 6.3. Furthermore, the aerodynamic damping is dependent on the wind velocity as shown in Figure 7.9.

A study is performed on the differences with the ice-only case to get a better understanding of the phenomena that occur for the combined model. It must be noted that more elaborate research is required to identify the phenomena over the full range of ice and

Table 7.2: Properties used for the assessment of dynamic effects wind velocity

Parameter	Symbol	Value	Unit
Ice thickness	h	0.4	m
Ice velocity	v_{ice}	1-250	mm/s
Mean wind velocity	V_{w}	3,12	m/s
Number of ice velocities	N_{sim}	23	#
Simulation time	t_{sim}	600	s
Time cut-off	t_{ini}	50	s
Time step size	Δt	0.01	s

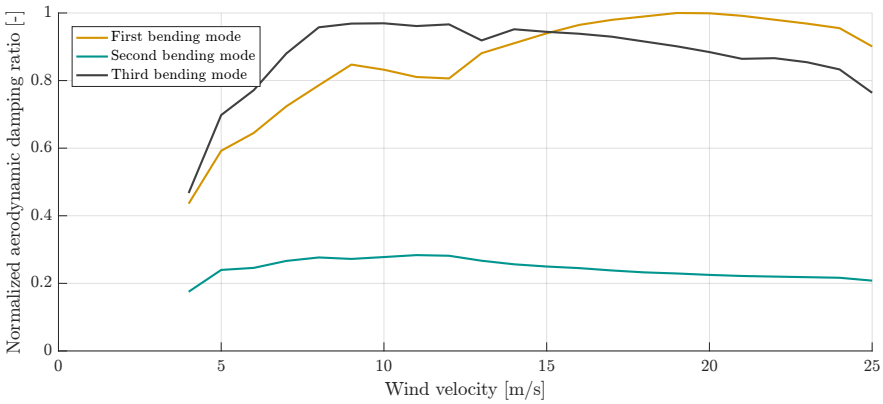

Figure 7.9: Typical normalized aerodynamic damping for the first three bending modes

wind velocities. This is however outside the scope of this thesis. The focus of this section is to gain a high level insight on the dynamic behavior, in support of a comparison with the uncoupled model in the next chapter. To acquire this insight, two wind velocities are examined and compared to the ice-only case:

- *Around cut-in wind speed (3 m/s)*
  The cut-in wind speed includes a relatively small aerodynamic damping and relatively low thrust. Hence, this case represents the situation with a small aerodynamic influence to the model.

- *Around rated wind speed (12 m/s)*
  In the vicinity of rated wind speed, the aerodynamic damping is relatively large for all modes. Furthermore, according to the thrust curve in Figure 6.10, the thrust is near its maximum at rated wind speed. Hence, this case represents the situation with a large aerodynamic influence to the model.

The ice-only case discussed in the previous section is related to the situation where the wind velocity is zero. Since a wind speed of 0 m/s is below the cut-in wind speed, the OWT is considered to be in idling mode. This is based on two assumptions:

1. The differences between the structural model in idling mode and the structural model in production mode, e.g due to the pitch angle of the blades, are small.

2. The aerodynamic damping for an idling wind turbine at 0 m/s wind speed is small enough to be neglected.

7.3.1. Modal contribution

For convenience reasons the comparison study is presented in accordance with the previous section. Therefore, the ratio between kinetic and potential energy and the modal contribution is discussed first.

- Figure 7.10 and Figure 7.11 show the ratio between potential and kinetic energy at wind speeds of 3 and 12 m/s respectively. For both wind velocities it holds that the potential energy is clearly dominant. However, at cut-in wind speed the kinetic energy is relatively higher, with a maximum at about 5 mm/s.

- Figure 7.12 and Figure 7.13 show the contribution of the kinetic energy of the first three bending modes. It is observed that the kinetic energy is governed by the first bending mode for both wind velocities.

A conceivable reasoning behind the observations above is related to the location where the wind load applies. Tower top is at approximately 140 m from mudline, creating a significantly larger moment compared to the location where the ice acts upon the structure. Furthermore, the mode shape amplitude at tower top is maximum for the first bending mode. This combined results in a relatively large deflection in the first bending mode, clarifying the dominance of the first bending mode.

Clear differences can be observed between rated and cut-in wind speed. It is expected that these differences are originating from the difference in aerodynamic influence. The modal contribution at cut-in wind speed shows more variation over the ice velocities, indicating varying influence of the ice. This ice influence is investigated further by observing the time signals at an ice velocity of 2 mm/s.

Figure 7.14 shows the deflections at MSL for cut-in and rated wind speed, at an ice velocity of 2 mm/s. Both signals suggest that intermittent crushing occurs, which is expected for this ice velocity. The mean deflection appears to be larger for rated wind speed. Furthermore, at rated wind speed, the motion of the first bending mode is more apparent in the signal. Both observations can be explained by the larger thrust at rated wind speed.

It is therefore concluded that the aerodynamic influence on the ice-structure interaction, for intermittent crushing, is larger at rated wind speed in comparison to cut-in wind speed. This influence is apparent in the mean deflection, and during the loading phase of intermittent crushing.

7.3.2. Influence of ice using DEL at mudline

The previous observations raise questions about the influence of the ice on the dynamics in the combined model. To evaluate the isolated influence of the ice, the DELs are compared as follows. First, the DEL is computed by a model in which only thrust is applied, resulting in the values per wind velocity given in Table 7.3. Next, the DEL for this wind-only case is subtracted from the values of the combined model. This gives an indication of the ice contribution to the DEL. The results are shown in Figure 7.15.

Table 7.3: DEL for wind-only per wind speed

Wind speed	Value	Unit
0 m/s	0	MNm
3 m/s	4	MNm
12 m/s	20	MNm

For reference, in Figure 7.15 the DEL computed from the ice-only case is included as well. This enables a comparison of the combined model with the assumed idling model. A very interesting observation is the negative contribution of the ice at rated wind speed, for ice velocities between 1 and 10 mm/s. This range even includes the ice velocity where creep is expected; 1 mm/s. To get a better understanding of the interaction behavior occurring at this ice velocity, the deflections at MSL are for an ice velocity of 1 mm/s is shown in Figure 7.16.

A conceivable explanation for the negative contribution of the ice to the DEL, is that the harmonics occur during the loading phase of intermittent crushing. During this loading phase the ice deforms inelastically. As the structure moves in the direction of the ice, the contact area will increase. Since this directly increases the load, it will serve as a damping effect to the structural motion.

The damping subsequently results in a negative contribution of the ice to the DEL. For 'ice damping' to occur, the contribution to the deflection, originating from the thrust, must be large enough to increase the contact area. It is believed that this contribution is too small at cut-in wind speed.

A second observation is discussed regarding the ice velocities where FLI occurred in the ice-only case, i.e. in the vicinity of 85 mm/s. It is clearly shown in Figure 7.15 that in the combined wind and ice simulations, the contribution from the ice to the DEL is

significantly lower for both cut-in and rated wind speed. This observation can be clarified with the aerodynamic damping. It is therefore suggested that the influence of aerodynamic damping to the second bending mode is large enough to prevent FLI in the second bending mode. A second clarification could be that the wind loading significantly disturbs the ice-structure interaction behavior, hence preventing FLI to occur. Therefore, even a relatively small influence by the thrust force, as was observed for the cut-in wind speed in Figure 7.14, would be able to disturb the FLI behavior.

7.4. Chapter summary

In this chapter, the model was applied to two cases. The first case considered ice as the only applied external load to the OWT model. The second case considered the combination of ice and aerodynamic loading. The results were visualized by the potential and kinetic energy in the system. Moreover, the fatigue damage obtained during the simulation is used to compare the coupled model to the uncoupled model in the next chapter.

In the first case where ice was the only applied load, the following conclusions are drawn for the specific case study:

I The behavior at an ice velocity of **1 mm/s** is explained by the quasi-static behavior of creep.

II The behavior from **1.5 mm/s to 4 mm/s** is related to intermittent crushing.

III The behavior from **5 mm/s to 10 mm/s** is related to the resonance in the first bending mode. This resonance is not related to FLI, but originating from intermittent crushing in the eigen frequency of the first fore-aft bending mode.

IV The behavior from **10 mm/s to 100 mm/s** is related to frequency lock-in in the second bending mode.

V The behavior at velocities **higher than 100 mm/s** is related to continuous brittle crushing occurring at high ice velocities.

In the second case where both ice and wind loading were applied, the following conclusions are drawn for the specific case study:

- The aerodynamic influence on the ice-structure interaction, for intermittent crushing, is larger at rated wind speed in comparison to cut-in wind speed.
- At rated wind speed, the contribution of the thrust is large enough to induce significant deflection at MSL. It is believed that due to increase of contact area while the structure moves in the opposite direction of the ice velocity, the structural motion is damped.

- Due to the aerodynamic influence, FLI does not occur. It is suggested that this may be caused by the aerodynamic damping, and the disturbance at MSL originating from the thrust load.

A comparison was made between coupled and uncoupled models for dynamic ice-structure interaction. The uncoupled models use an external ice load series to represent the ice-structure interaction and were based on methodology used in industry practice.

Two cases were considered; the situation where only ice loading is applied to the structure, and the situation where the structure is subjected to both ice and wind loading. In case of ice-only loading, it was concluded that the uncoupled model is not capable of capturing intermittent crushing and frequency lock-in behavior due to inconsistency between the load signal and the response.

In case of combined ice and wind loading, it was concluded that the uncoupled model in incapable of capturing intermittent crushing behavior and the ice-damping phenomenon. The same inconsistency was used as an explanation.

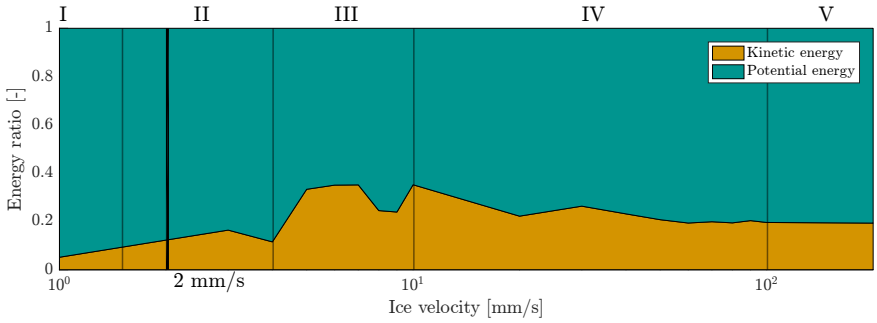

Figure 7.10: Ratio between potential and kinetic energy at **cut-in** wind speed

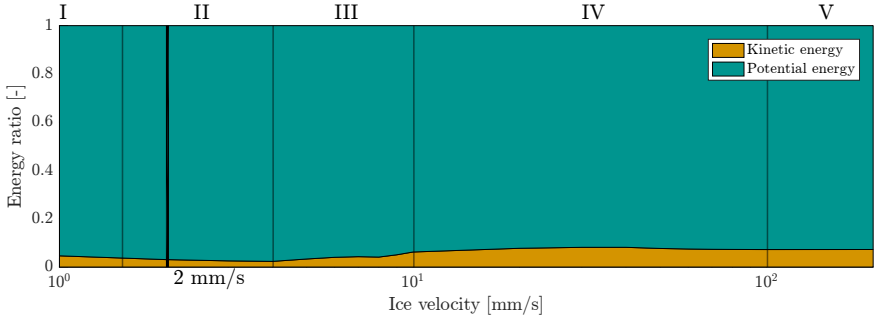

Figure 7.11: Ratio between potential and kinetic energy at **rated** wind speed

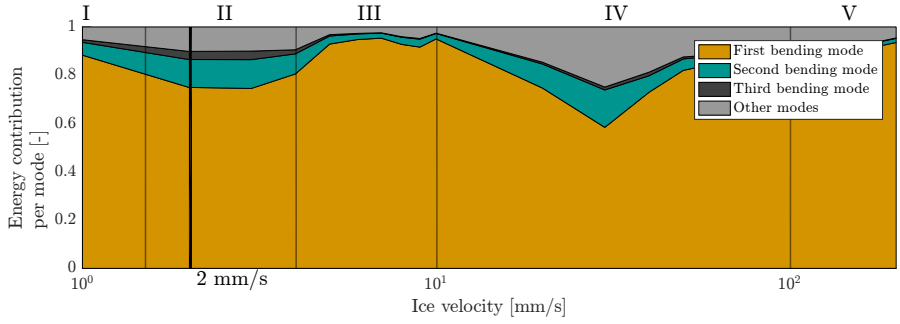

Figure 7.12: Energy contribution of the first three modes at **cut-in** wind speed

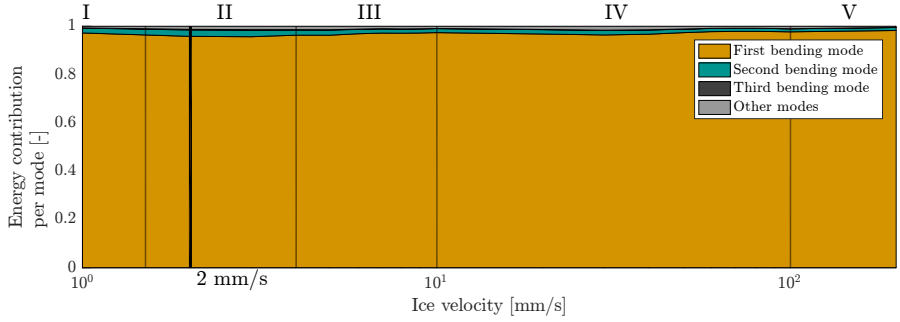

Figure 7.13: Energy contribution of the first three modes at **rated** wind speed

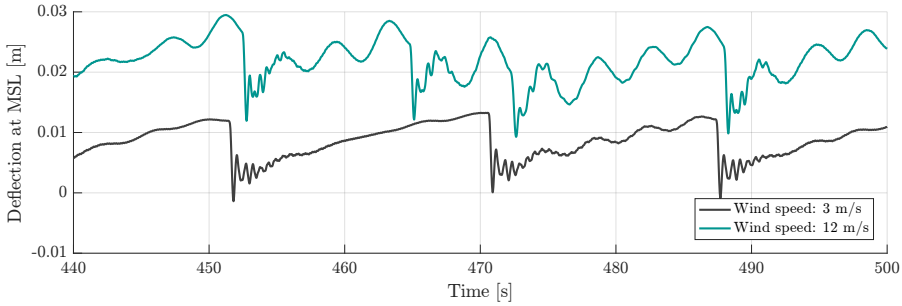

Figure 7.14: Deflection at MSL at an ice velocity of **2 mm/s** for cut-in and rated wind speed

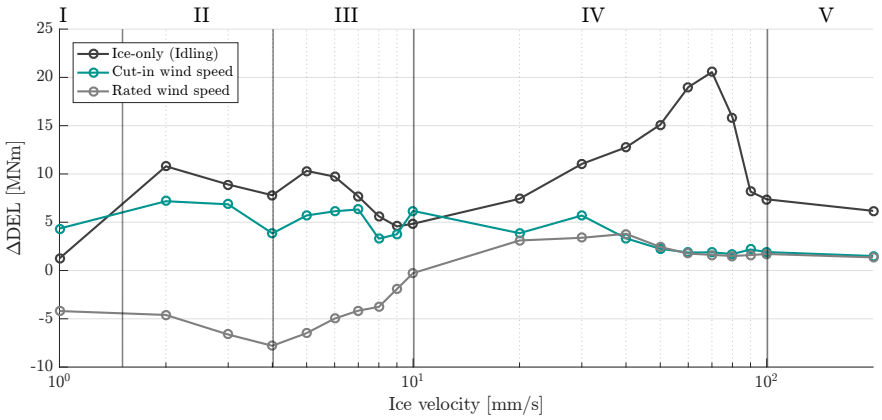

Figure 7.15: Contribution of the ice to the DEL for zero, cut-in, and rated wind speed

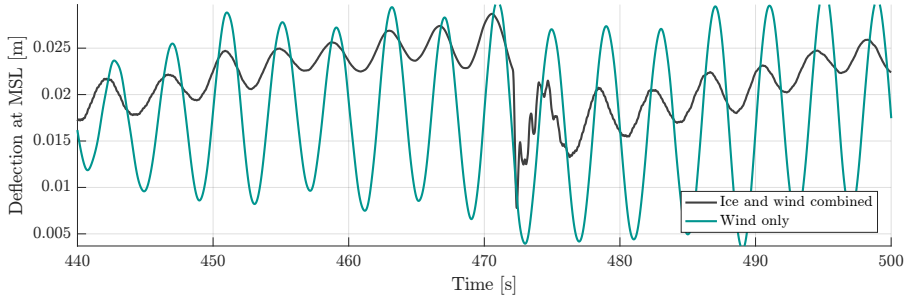

Figure 7.16: Deflection at MSL at an ice velocity of **1 mm/s** and **rated** wind speed. Two cases are considered: 1): The combination of wind and coupled ice 2): Only wind loading.

Chapter 8
Comparison between coupled and uncoupled modeling of ice-structure interaction and wind loading

In this chapter the results of of coupled models of dynamic ice-structure interaction are compared to the results of uncoupled models. Firstly an elaboration is give on the approach of the comparison study in section 8.1. The first comparison study involves the ice-only case in section 8.2, where no other external load except for ice loading is considered. The second comparison study involves the combined ice and wind case in section 8.3, where both ice and wind loading are included.

8.1. Approach to the comparison study

A comparison is made between the results of the coupled models discussed in chapter 7 and the results of uncoupled models used in current practice. The results created by the coupled simulations are referred to as the 'reference case'. The reference cases are compared to simulations in which the ice was modeled in an uncoupled manner. These uncoupled simulations are referred to as 'simplifications'. All simplifications involve the method of applying an ice load as an external load series, simplifying the simulation to a linear problem. The manner in which this load series is generated differs for each simplification.

The simplifications are based on methodology for uncoupled models as used in industry practice. The current approach of analyzing responses induced by ice loading, involves the application of a load-time series to an OWT model. To investigate the effect of such uncoupled modeling, two simplified models are discussed, representing models typically

used in practice:

1. In the first simplification, the structural model used to generate the ice load series is different from the model on which the load-time series is subsequently applied. The structural difference is the usage of a lumped mass to represent the RNA, instead of the RNA super element. The results om this simplification are compared to the results of the coupled modeling for the ice-only case, as discussed in section 7.2. The procedure for this comparison study is illustrated in Figure 8.1.

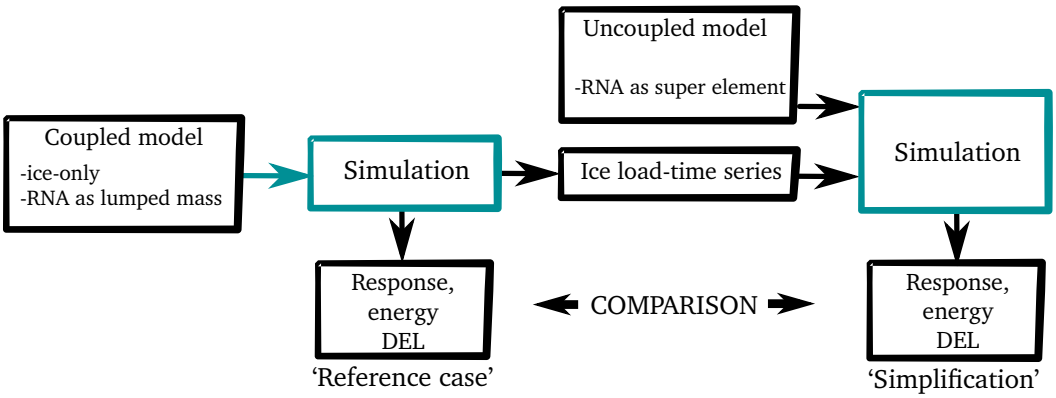

Figure 8.1: Flowchart of the comparison study for ice-only loading

The first simplification will demonstrate the effect of not using the exact same model to generate the ice load-time series. This effect is a consequence of uncoupled simulation, since in the case of the simplification, the ice load-time series is not depending on the structural response of the OWT.

2. In the second simplification, the ice load-time series is generated during the coupled modeling of the ice-only case. The ice load-time series is applied to an uncoupled model where aerodynamic effects are included. The results of this simplification are compared to the results from the coupled model of the combined ice and wind case, as discussed in section 7.3. The procedure for this comparison study is illustrated in Figure 8.2.

The second simplification will demonstrate a consequence of uncoupled simulation since the ice-load is not influenced by the aerodynamic effects. In other words, influence of wind induced motion on ice is neglected. It must be noted that in practice often a combination of simplification 1 and 2 occurs. However, for clarity both effect are investigated separately.

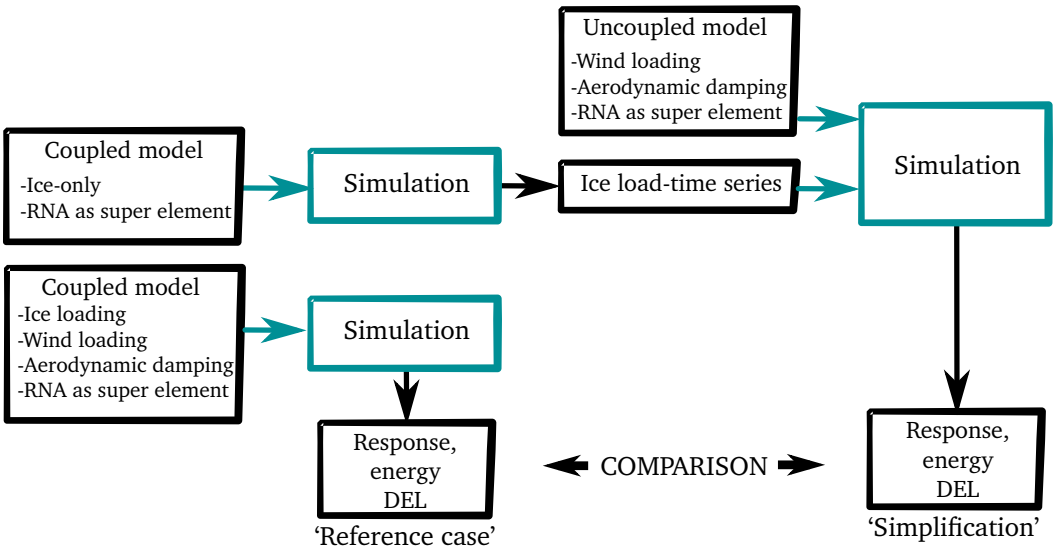

Figure 8.2: Flowchart of the comparison study for combined ice and wind loading

8.2. Simplification for ice-only loading

In section 7.2 the behavior of the OWT subjected to ice loading was examined. With this in mind the simulations are repeated in an uncoupled manner and compared to the reference case. The global ice load that is applied to the structural model, is generated using a simplified structural model. The differences between the structures are discussed in section 6.2 and are considered to be small. The results of the simulations with the simplified model are discussed next.

8.2.1. Modal contribution

The ratio between potential and kinetic energy, and the kinetic energy contribution to the first three bending modes are shown in Figure 8.3 and Figure 8.4 respectively.

The following can be observed when comparing these figures to the reference case in Figure 7.1 and Figure 7.2:

I At an ice velocity of **1 mm/s** both the energy ratio, and modal contribution remain equal to the reference case. This can be explained by the creep failure at this velocity. Since the applied load remains quasi-constant, the response remains quasi static.

II At ice velocities from **1.5 mm/s to 4 mm/s** the second bending mode is dominant and the energy ratio is close to 1:1. This indicates that resonance in the second bending

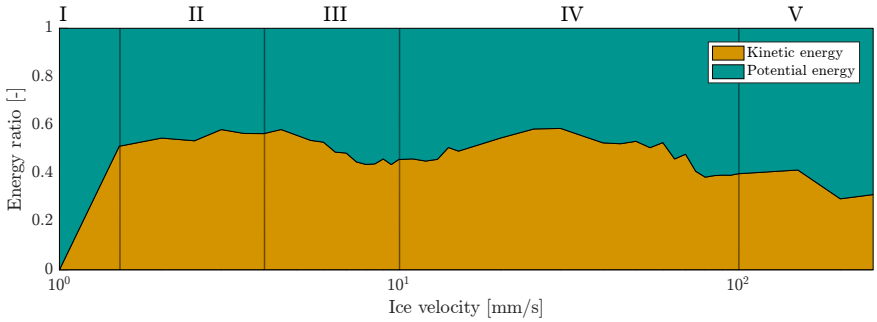

Figure 8.3: Ratio between mean kinetic and mean potential energy over varying ice velocities. The ice load is produced using a simplified structure

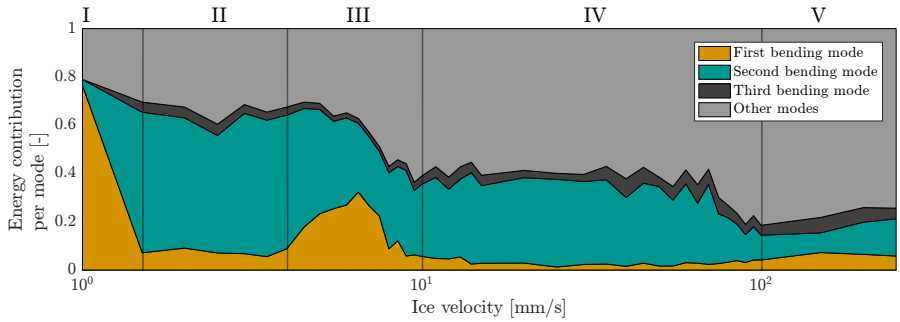

Figure 8.4: Energy contribution for varying ice velocities. The ice load is produced using a simplified structure

mode occurs, for ice velocities where intermittent crushing is expected. This is in contrast to the reference case, which shows intermittent crushing at these ice velocities. The time signal for a specific ice velocity in this range will be further investigated.

To gain a better understanding of what causes the discrepancy with the reference case, the responses of the different structures are compared. The top graph of Figure 8.5 shows the deflection at MSL of the simplified structure while producing the ice load-time series. In the center graph the applied load series is shown, and in the bottom graph the deflection response of the simplified model is given.

One can conclude that both responses are a product of the same load series in the center graph of Figure 8.5. The top graph shows the deflection of the structure with the lumped mass, and the bottom graph shows the deflection of the structure with the RNA super element.

One must keep in mind that the displacement of the structure with the lumped mass

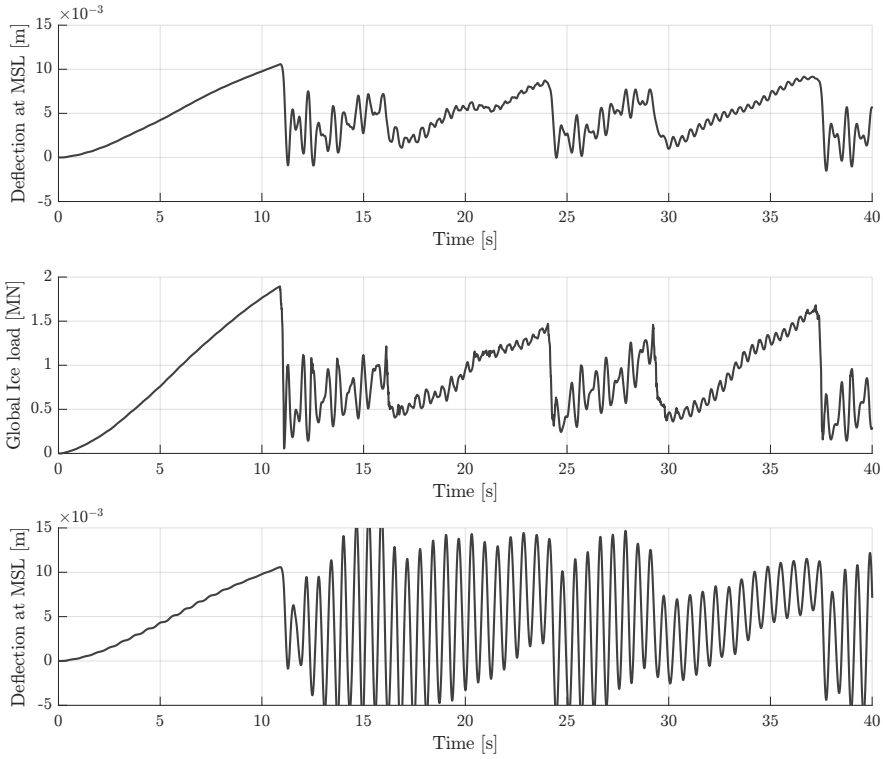

Figure 8.5: Top: Deflection at MSL of the simplified structure. Center: Global ice load created from the simulation with the simplified structure. Bottom: Deflection at MSL of the reference structure while the ice load series is applied. Ice velocity: 3mm/s

(top) and the ice load (center) can be considered as the product of a coupled solution. This means that e.g. when the structure moves in the opposite direction of the ice velocity, the load is relatively low. Subsequently, when the structure moves in the same direction as the ice velocity, the ice load is relatively high.

However, this is not the case for the displacement of the structure with the RNA super element (bottom plot in Figure 8.5). Here, the timing of the load signal does not correspond to the deflection of the structure. Even the slightest difference in the structural properties will cause this inconsistency. In Figure 8.5 this occurs first at about 12 seconds into the simulation. From this instance in time, the load signal is merely a quasi random external load with a certain frequency content. The response of the structure is governed

by the second bending mode since its modeshape amplitude at MSL is relatively large and its frequency is apparent in the load signal.

The inconsistency between the load and the motion of the OWT will occur for all ice velocities as a consequence of uncoupled modeling. Its effect at higher velocities is discussed next.

III At ice velocities from **5mm/s to 10mm/s** a small peak in the contribution of the first bending mode remains apparent. However, it has decreased significantly compared to the reference case. In section 7.2 this peak was explained by intermittent crushing occurring in the frequency of the first bending mode. Since the load signal contains the frequency of the first bending mode, resonance occurs. However, as a consequence of the inconsistency, the resonance is disrupted resulting in a smaller contribution of the first bending mode.

IV At ice velocities from **10mm/s to 100mm/s** the second bending mode is governing in both cases. However, the peak related to FLI of the second bending mode has decreased. This can be explained by the inconsistency of the load signal as well. During frequency lock-in, the loading and unloading are exactly in phase with the motion of the structure, i.e. it is not the result of a load with a governing frequency. Therefore, the slightest inconsistency will disrupt the FLI regime and results in a quasi-random response.

V **For higher ice velocities** the second bending mode remains dominant. This is clarified by a smaller magnitude of the effect at higher ice velocities. Since load signal in continuous brittle crushing is quasi-random in the reference case, the inconsistency has a relatively small effect, hence the structural dynamics can be captured by the simplified model. Here, only in this regime, the two models produce similar results.

8.2.2. Damage equivalent load

The discussed discrepancies are supported by the computed values for the DEL illustrated in Figure 8.6. The discrepancies between the reference case and the simplification are discussed next.

I At an ice velocity of **1 mm/s** the DEL remains equal for both models, since the load is quasi static for both cases.

II At ice velocities from **1.5 mm/s to 4 mm/s** intermittent crushing occurs in the reference case. Due to the inconsistency discussed in the previous subsection, a relatively large discrepancy is observed in the DEL.

III At ice velocities from **5mm/s to 10mm/s**, intermittent crushing will occur in the reference case, at the eigen frequency of the first bending mode. This behavior is not captured in the simplified model, hence a discrepancy in the DEL is observed. However, the discrepancy in DEL seems to decrease in the vicinity of an ice velocity of 10

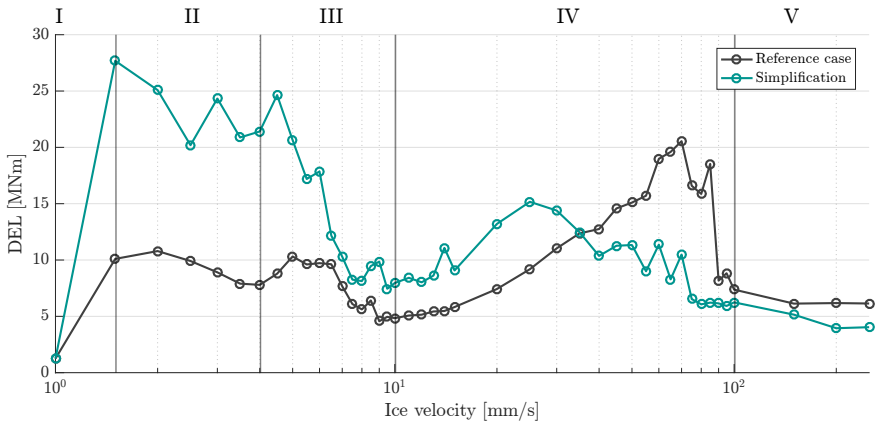

Figure 8.6: Comparison between DEL for reference case and DEL from applied load created using a simplified structure at **mudline**

mm/s. It is suggested that a transition from intermittent crushing to FLI occurs for the reference case. Since the load signal in this transition is quasi-random, the resulting quasi-random dynamics can be captured by the simplified model.

IV At ice velocities from **10mm/s to 100mm/s**, FLI in the second bending mode occurs for the reference case. Also this behavior cannot be captured by the simplified model and thus a discrepancy in DEL is observed.

V **For higher ice velocities**, continuous brittle crushing occurs in the reference case. The load signal for this regime is quasi-random, hence can be captured by the simplified model. The discrepancy in DEL is therefore relatively small.

8.3. Simplification for ice and wind loading

In this section a comparison is made between reference case for ice and wind as discussed in section 7.3, and the second simplification discussed in section 8.1. In the simplified model, the ice load is applied as an external load series. This load series was generated by the coupled model where solely ice-structure interaction was incorporated. In other words, the load generated by the ice-only reference case is applied to the structural model, together with a thrust force and aerodynamic damping.

The focus of this section will be on the identification of the discrepancy created by the simplification. To demonstrate this, only a single wind speed is discussed. The chosen wind speed is the rated wind speed, since its influence on the ice-structure interaction is considered to be largest. The comparison is made using the contribution of the ice to the DEL,

which was computed as discussed in section 7.3. Figure 8.7 shows the contribution of the ice to the DEL, over varying ice velocities for both the reference case and the simplification.

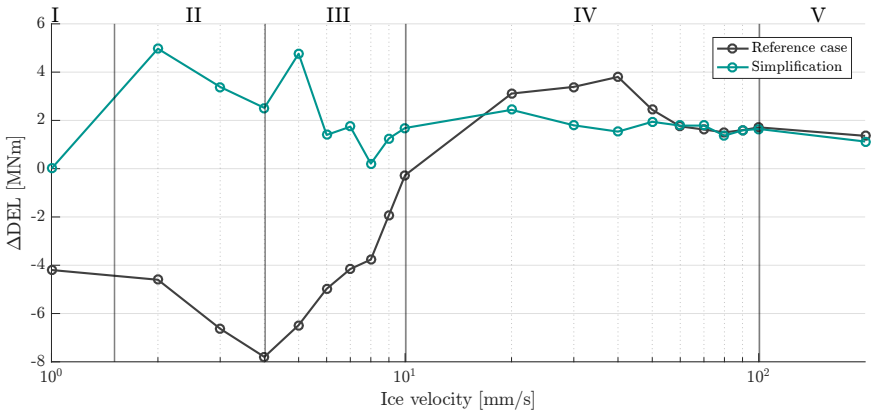

Figure 8.7: Contribution of the ice to the DEL for the reference case and the simplification

I II, and III
The reference case shows a negative contribution originating from ice damping at the ice velocities between 1 and 10 mm/s, as discussed in section 7.3. This negative contribution is not observed in the DEL of the simplification. To investigate the behavior occurring at these velocities the time series at 2 mm/s is shown in Figure 8.8.

Figure 8.8 shows the deflection at MSL and the applied ice load series, for the reference case and the simplification. The reader is reminded that the load signal of the simplification is created during the reference case of ice-only, hence does not include influence of wind loading. The major difference between the load signals is therefore the aerodynamic influence. Furthermore, in both signals intermittent crushing is apparent, which is expected at this ice velocity. When comparing the deflection at MSL the following two observations are made:

- From the response at MSL, in the reference case, the intermittent crushing regime can be observed. During the loading phase, the frequency of the first bending mode is apparent in the signal, as discussed in section 7.3. However, in the response of the simplified model the intermittent crushing behavior cannot be observed.
- The amplitude of the response of the simplified model is significantly larger compared to the reference case. This suggests that ice damping is not captured in the simplified model and clarifies the fact that the uncoupled model fails to generate a negative ice contribution to the DEL, at velocities where intermittent crushing is expected to occur.

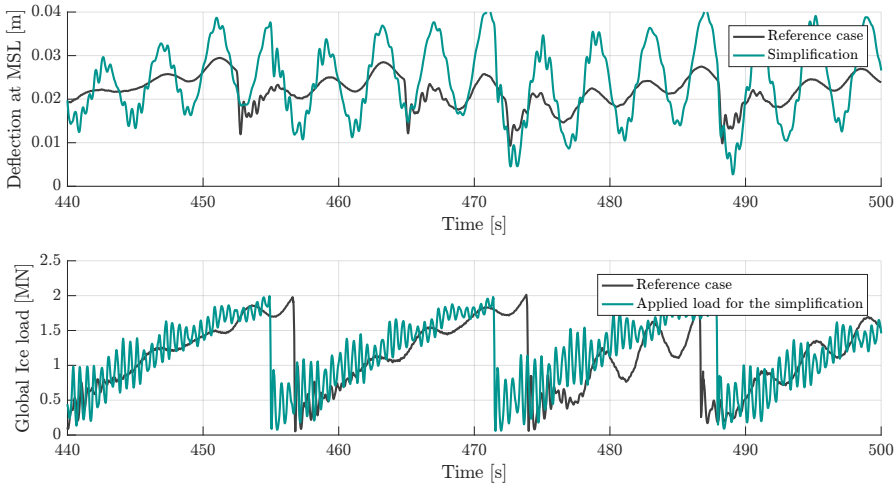

Figure 8.8

Both observations can again be explained by the inconsistency between the loading and the structural motion as was discussed in section 8.2. Due to disturbances induced by the wind loading, the timing of the load signal does not correspond to the motion of the structure. The latter results in the fact that intermittent crushing and ice damping cannot be captured by the simplified model.

The observations from Figure 8.7 for ice velocities where intermittent crushing does not occur are discussed next.

IV and V
: At higher velocities where continuous brittle crushing is expected, the smallest discrepancies in the ice contribution to the DEL are observed. This can again be explained by the quasi-random nature of the ice load during continuous brittle crushing.

8.4. Chapter summary

A comparison was made between coupled and uncoupled models for dynamic ice-structure interaction. The uncoupled models use an external ice load series to represent the ice-structure interaction and were based on methodology used in industry practice.

Two cases were considered; the situation where only ice loading is applied to the structure, and the situation where the structure is subjected to both ice and wind loading. In

case of ice-only loading, it was concluded that the uncoupled model is not capable of capturing intermittent crushing and frequency lock-in behavior due to inconsistency between the load signal and the response.

In case of combined ice and wind loading, it was concluded that the uncoupled model in incapable of capturing intermittent crushing behavior and the ice-damping phenomenon. The same inconsistency was used as an explanation.

Chapter 9
Conclusions and recommendations

The general goal of this thesis was to create and apply a model to simulate the dynamic interaction between ice and an offshore wind turbine. To demonstrate the value of such a model, a comparison was made to uncoupled approaches used in current practice. The work was divided in two separate objectives:

1. Create a coupled model for dynamic ice-structure interaction on offshore wind turbines
2. Compare the the results of the coupled model and uncoupled modeling as is more commonly applied

The conclusions of this thesis are discussed according to the structure of this thesis in section 9.1. Then finally, the thesis is concluded by a brief discussion on recommendations for future work in section 9.2.

9.1. Conclusions

In this section, the conclusion of this thesis are formulated. Firstly, the conclusions regarding the extension and implementation of the phenomenological model are discussed, followed by the conclusions on the application of the phenomenological model to an OWT. The latter will include the conclusions of the comparison study of chapter 8.

9.1.1. Extension and implementation of the phenomenological model

A phenomenological model for dynamic ice-structure interaction published by Hendrikse and Metrikine (2015a) has been numerically implemented. The existing model covers the phenomena of intermittent crushing, frequency lock-in, and continuous brittle crushing.

Extensions have been realized to include creep and buckling behavior as well.

Reference data from the LOLEIF project (Fransson and Lundqvist, 2006) as well as the JOIA project (Takeuchi and Sakai, 2001) was used to compute realistic full-scale input parameters for the model. With the use of these parameters, a verification study was performed. From the results of this study, it can be concluded that the model is verified in a qualitative as well as in a quantitative sense.

Conclusion 1: *A coupled model for dynamic ice-structure interaction was successfully implemented and extended to include creep and buckling failure as well as the application to cylindrical structures*

9.1.2. Results from the coupled modeling of dynamic ice-structure interaction

A study was performed on the coupled modeling of dynamic ice-structure interaction. The study was performed for specific cases, hence general conclusions cannot be drawn from this study alone. However, the conclusions drawn from these specific cases are given here. The first case consists of a situation where the OWT model is solely subjected to ice interaction.

A sensitivity study was performed by using multiple seeds and comparing the differences at varying ice velocities. At velocities where a transition between resonance and quasi-random behavior occurs, large discrepancies in DEL are observed.

Conclusion 2: *The discrepancy in fatigue damage, at mudline, for different seeds is significant in the vicinity of ice velocities where transition from resonance to quasi-random behavior occurs.*

Observations of FLI in the second fore-aft bending mode of the OWT were made. Moreover, resonance unrelated to FLI was noticed in first fore-aft bending mode during intermittent crushing behavior.

Conclusion 3: *Resonance behavior, unrelated to FLI, may occur during the intermittent crushing regime*

The second case consisted of the coupled modeling of ice-structure interaction combined with wind loading and aerodynamic damping. From the results it was observed that the fatigue damage in the OWT at mudline, originating from the wind loading, decreased due to the ice-structure interaction.

Conclusion 4: *The phenomenological model predicts an ice-induced decrease in fatigue damage at mudline, at ice velocities where intermittent crushing is occurs.*

The observed FLI in the situation where solely ice loading was modeled, does not occur for the situation where wind loading and aerodynamic damping are included as well.

Conclusion 5: *Due to aerodynamic effects, FLI does not occur in the specific case study.*

9.1.3. Comparison between coupled and uncoupled modeling

A comparison was made between the results of the coupled model and the uncoupled model for the situation where the structure is solely subjected to ice loading. Large differences in fatigue damage were observed. Moreover, intermittent crushing and frequency lock-in were not captured in the uncoupled model.

Conclusion 6: *The uncoupled model is unable to capture intermittent crushing and frequency lock-in behavior correctly, when the ice load-time series is generated by a model that contains small differences in structural properties.*

Finally, a coupled model was compared with an uncoupled model for the situation where both ice and wind loading are applied. The results showed that intermittent crushing and the decrease in fatigue damage were not captured by the uncoupled model.

Conclusion 7: *For the combined modeling of ice and wind loading, the uncoupled model is incapable of capturing intermittent crushing behavior and the decrease in fatigue damage that is described by the coupled model.*

9.2. Recommendations

The recommendations are divided in two categories in accordance with the structure of this thesis. The first category focuses on the phenomenological model for dynamic ice-structure interaction. The second category considers recommendations originating from the results of the coupled and uncoupled modeling.

9.2.1. Recommendations on the phenomenological model

i *Statistical reference parameters*
The phenomenological model uses constant values as a reference to determine the input parameters of the ice. It is suggested to implement statistical reference data, which can be translated into stochastic input parameters. The distributed values will resemble the inhomogeneous properties of the ice sheet. This conceivably will give a more realistic representation of the ice as it interacts with the structure.

(a) *Measurement data*
Subsequent to the previous recommendation, more full-scale measurement data is required to improve the reliability of the model. To the author's knowledge, no single project is performed that covers a complete set of reference data required in the model. Moreover, in order to improve the model by using statistical input parameters, more reference data is vital.

(b) *Variation of ice velocity and ice thickness*
A relatively easy step can be made by using statistical data on ice velocity and ice thickness. The model created for this thesis already includes the feature of varying ice velocity. Furthermore, a thickness profile over the length of a simulation could be generated from statistical data available. From this profile, the input parameters can be computed as a series. Since this data can be pre-processed, no significant increase in computational time is expected.

ii *Model sensitivity*
It is suggested that a comprehensive study should be performed to identify the sensitivity of the phenomenological model to its reference parameters. Such a sensitivity study could These parameters require a more careful approach when being obtained from measurement data and should be the focus of future measurement campaigns.

iii *Numerical improvements*
The current numerical method involves the inversion of the relatively large stepping matrix. A part of this matrix is related to the linear structural model and can therefore be solved with a constant stepping matrix. Solving the models separately as suggested by Van der valk (2014), can potentially reduce computational time by a significant amount. It must be noted that iteration at the interface between the now separate models, is then required to find a solution.

9.2.2. Recommendations originating from the results of the coupled and uncoupled models

iv *Influence of damping*
From the results of the coupled model, where the structure was subjected to both ice and wind loading, it was concluded that aerodynamic damping has a significant influence on the occurrence of FLI. It is therefore recommended to perform extensive research on the sensitivity of this failure regime, to damping in the structural model. Moreover, it is suggested to investigate the influence of passive damping e.g. tuned mass dampers in the prevention of FLI.

v *Integration with a fully coupled offshore wind turbine model*
In the used structural model, aerodynamics are included in an uncoupled manner. Furthermore, hydrodynamic loading from e.g. currents is omitted, as well as the RNA dynamics of a producing wind turbine. It is therefore suggested to couple the phe-

nomenological model to a more comprehensive structural model including more realistic structural and environmental factors, e.g. BHawC.

vi *Increase of the result accuracy*
To reduce the computational time of generating the results, a limited amount of simulations was performed. For engineering purposes it is recommended to perform a more extensive research of the influence of ice and wind velocity on the ice-structure interaction behavior, i.e. simulate for more velocities. This research may then result in a better understanding of the dynamic ice-structure interaction phenomena.

Appendix A
Numerical time stepping

This section elaborates on the numerical method used to compute solutions of the model in the time domain. For its known capability of solving finite element models with small computational resources, its widely spread knowledge across the Siemens Wind Power department, and for other convenience reasons, the Newmark scheme is used. A derivation of this scheme is given here, as was done by Rixen (2012), starting with a scheme to solve a linear problem.

Newmark for linear problems

For each step in the time domain an equilibrium of forces in the system must be found. The Newmark scheme is a typical prediction-correction scheme starting with predicting a solution for the next step in time, called step n.

$$\boldsymbol{r}(\boldsymbol{u}_n) = \boldsymbol{M}\ddot{\boldsymbol{u}}_n + \boldsymbol{C}\dot{\boldsymbol{u}}_n + \boldsymbol{K}\boldsymbol{u}_n - \boldsymbol{g} = 0 \tag{A.1}$$

Where $\boldsymbol{r}$ is the residual, $\boldsymbol{M}$, $\boldsymbol{C}$, and $\boldsymbol{K}$ are the mass, damping, and stiffness matrices respectively, and $\boldsymbol{g}$ is the load vector. For each step in time a routine is used starting with the conditions of the previous step $n-1$, being the initial conditions in the first time step.

$$\boldsymbol{u}_{n-1}, \dot{\boldsymbol{u}}_{n-1}, \ddot{\boldsymbol{u}}_{n-1} \tag{A.2}$$

The Newmark time integration Rixen (2012) states the following approximations for time step n, given the conditions of the previous step:

$$\boldsymbol{u}_n = \boldsymbol{u}_{n-1} + dt \cdot \dot{\boldsymbol{u}}_{n-1} + \left(\frac{1}{2} - \beta\right) \cdot dt^2 \cdot \ddot{\boldsymbol{u}}_{n-1} + \beta \cdot dt^2 \cdot \ddot{\boldsymbol{u}}_n \tag{A.3a}$$

$$\dot{\boldsymbol{u}}_n = \dot{\boldsymbol{u}}_{n-1} + (1-\gamma) \cdot dt \cdot \ddot{\boldsymbol{u}}_{n-1} + \gamma \cdot dt \cdot \ddot{\boldsymbol{u}}_n \tag{A.3b}$$

The approximation involves the constants β and γ. For stability reasons the constant acceleration algorithm is used where these constants are equal to $\frac{1}{2}$ and $\frac{1}{4}$ respectively. As

$\ddot{\boldsymbol{u}}_n$ is not known yet, a prediction, denoted with *, is made assuming $\ddot{\boldsymbol{u}}_n = 0$. This reduces Equation A.3 to:

$$\boldsymbol{u}_n^* = \boldsymbol{u}_{n-1} + dt \cdot \dot{\boldsymbol{u}}_{n-1} + \left(\frac{1}{2} - \beta\right) \cdot dt^2 \cdot \ddot{\boldsymbol{u}}_{n-1} \tag{A.4a}$$

$$\dot{\boldsymbol{u}}_n^* = \dot{\boldsymbol{u}}_{n-1} + (1-\gamma) \cdot dt \cdot \ddot{\boldsymbol{u}}_{n-1} \tag{A.4b}$$

Therefore, the difference between the predicted deflections and the actual deflections, and the difference between the predicted velocities and the actual velocities can be written as:

$$(\boldsymbol{u}_n - \boldsymbol{u}_n^*) = \beta \cdot dt^2 \cdot \ddot{\boldsymbol{u}}_n \tag{A.5a}$$

$$(\dot{\boldsymbol{u}}_n - \dot{\boldsymbol{u}}_n^*) = \gamma \cdot dt \cdot \ddot{\boldsymbol{u}}_n \tag{A.5b}$$

Which can be rewritten to functions for the actual velocity $\dot{\boldsymbol{u}}_n$ and actual acceleration $\ddot{\boldsymbol{u}}_n$ at time step n, as a function on the difference between the predicted deflections and actual deflections $\Delta\boldsymbol{u}_n = (\boldsymbol{u}_n - \boldsymbol{u}_n^*)$.

$$\ddot{\boldsymbol{u}}_n = \ddot{\boldsymbol{u}}_n^* + \frac{1}{\beta \cdot dt^2}\Delta\boldsymbol{u}_n \tag{A.6a}$$

$$\dot{\boldsymbol{u}}_n = \dot{\boldsymbol{u}}_n^* + \frac{\gamma}{\beta \cdot dt}\Delta\boldsymbol{u}_n \tag{A.6b}$$

Substituting Equation A.6a and Equation A.6b into Equation A.1 gives a dynamic equilibrium problem in terms of displacements only:

$$\boldsymbol{r}(\boldsymbol{u}_n) = 0 \tag{A.7}$$

Which gives an equilibrium to be solved for the displacements at time step n:

$$\left[\boldsymbol{M}\frac{1}{\beta \cdot dt^2} + \boldsymbol{C}\frac{\gamma}{\beta \cdot dt} + \boldsymbol{K}\right]\boldsymbol{u}_n = \boldsymbol{g} + \boldsymbol{u}_n^*\left[\boldsymbol{M}\frac{1}{\beta \cdot dt^2} + \boldsymbol{C}\left(1 + \frac{\gamma}{\beta \cdot dt}\right)\right] \tag{A.8}$$

Now the actual displacement $\boldsymbol{u}_n)$ can be calculated and the displacement correction $\Delta\boldsymbol{u}_n$ can be found. The actual velocity and acceleration can be computed using Equation A.6a and Equation A.6b.

Newmark for nonlinear problems

The discontinuities in the ice element described earlier introduce nonlinearities into the system. The switch between contact and no contact causes the K matrix to be a function of the displacements. Furthermore, the external load $\boldsymbol{g}$ includes the nonlinear friction load

and is a function of the displacements as well. This changes Equation A.1 and Equation A.8 into:

$$\boldsymbol{r}(\boldsymbol{u}_n) = \boldsymbol{M}\ddot{\boldsymbol{u}}_n + \boldsymbol{C}\dot{\boldsymbol{u}}_n + \boldsymbol{K}(\boldsymbol{u}_n)\boldsymbol{u}_n - \boldsymbol{g}(\boldsymbol{u}_n) = 0 \tag{A.9}$$

and:

$$\left[\boldsymbol{M}\frac{1}{\beta \cdot dt^2} + \boldsymbol{C}\frac{\gamma}{\beta \cdot dt} + \boldsymbol{K}(\boldsymbol{u}_n)\right]\boldsymbol{u}_n = \boldsymbol{g}(\boldsymbol{u}_n) + \boldsymbol{u}_n^*\left[\boldsymbol{M}\frac{1}{\beta \cdot dt^2} + \boldsymbol{C}\left(1 + \frac{\gamma}{\beta \cdot dt}\right)\right] \tag{A.10}$$

As Equation A.10 cannot be solved directly a linearization technique is used. A linear expression of $\boldsymbol{u}_n$) is created and iterated until a certain tolerance for the residual is reached. These iterations are done according to the Newton-Raphson method which is explained here. First $\boldsymbol{u}_n^k$ is taken ad an approximate value of $\boldsymbol{u}_n$ at iteration k. Then a linear approximation for $\boldsymbol{r}(\boldsymbol{u}_n)$ is found by iteration as follows:

$$\boldsymbol{r}_L(\boldsymbol{u}_n^{k+1}) = \boldsymbol{r}_L(\boldsymbol{u}_n^k + \Delta\boldsymbol{u}^k) \cong \boldsymbol{r}_L(\boldsymbol{u}_n^k) + \boldsymbol{S}(\boldsymbol{u}_n^k) \cdot \Delta\boldsymbol{u}^k \tag{A.11}$$

Where $\Delta\boldsymbol{u}^k$ is an approximation to the displacement correction that should be applied to find the equilibrium of forces where $\boldsymbol{r}_L(\boldsymbol{u}_n^{k+1}) = \boldsymbol{0}$. From this follows:

$$\boldsymbol{r}_L(\boldsymbol{u}_n^k) = \boldsymbol{S}(\boldsymbol{u}_n^k)^{-1} \cdot -\boldsymbol{r}_L(\boldsymbol{u}_n^k) \tag{A.12}$$

The S matrix is called the 'Jacobian', or the 'iteration matrix' and is defined as:

$$\boldsymbol{S}(\boldsymbol{u}_n^k) = \left[\frac{\partial \boldsymbol{r}}{\partial \boldsymbol{u}}\right]_{\boldsymbol{u}_n^k} = \left[\boldsymbol{K}^t + \frac{\gamma}{\beta \cdot dt}\boldsymbol{C}^t + \frac{1}{\beta \cdot dt^2}\boldsymbol{M}\right]_{\boldsymbol{u}_n^k} \tag{A.13}$$

Where $\boldsymbol{K}^t$ and $\boldsymbol{C}^t$ are the tangent stiffness and the tangent damping matrices, meaning that they are the stiffness matrix $\boldsymbol{K}(\boldsymbol{u}_n^k)$ and the damping matrix $\boldsymbol{C}(\dot{\boldsymbol{u}}_n^k)$. For the ice element the damping matrix is linear and thus: $\boldsymbol{C}^t = \boldsymbol{C}$. The displacement correction $\Delta\boldsymbol{u}^k$ can now be computed and should be used to correct the displacements, velocities, and accelerations.

$$\boldsymbol{u}_n^{k+1} = \boldsymbol{u}_n^k + \Delta\boldsymbol{u}^k \tag{A.14a}$$

$$\dot{\boldsymbol{u}}_n^{k+1} = \dot{\boldsymbol{u}}_n^k + \frac{\gamma}{\beta \cdot dt}\Delta\boldsymbol{u}^k \tag{A.14b}$$

$$\ddot{\boldsymbol{u}}_n^{k+1} = \ddot{\boldsymbol{u}}_n^k + \frac{1}{\beta \cdot dt^2}\Delta\boldsymbol{u}^k \tag{A.14c}$$

Finalizing each iteration a convergence check is done by comparing the ratio of the internal forces to the residual. The internal forces are defined here as $\boldsymbol{f}(\boldsymbol{u}_n^k, \dot{\boldsymbol{u}}_{\boldsymbol{n}}^{\boldsymbol{k}}, \ddot{\boldsymbol{u}}_{\boldsymbol{n}}^{\boldsymbol{k}}) = \boldsymbol{M}\ddot{\boldsymbol{u}}_{\boldsymbol{n}}^{\boldsymbol{k}} + \boldsymbol{C}\dot{\boldsymbol{u}}_{\boldsymbol{n}}^{\boldsymbol{k}} + \boldsymbol{K}\boldsymbol{u}_n^k$. When a certain tolerance Tol is reached, the next step in time is made.

$$\frac{\parallel \boldsymbol{r}(\boldsymbol{u}_n^{k+1}) \parallel}{\parallel \boldsymbol{f} \parallel} \leq Tol \tag{A.15}$$

Appendix B
Stick-Slip

To show how the stick slip element behaves the following mechanical system is considered:

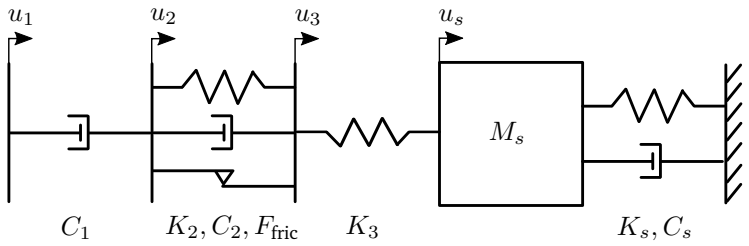

Figure B.1

The loads in the system may be defined as follows:

$$F_{c1} = C_1(\dot{u}_1 - \dot{u}_2) \tag{B.1}$$
$$F_{k2} = K_2(u_2 - u_3) \tag{B.2}$$
$$F_{c2} = C_2(\dot{u}_2 - \dot{u}_3) \tag{B.3}$$
$$F_{k3} = K_3(u_3 - u_s) \tag{B.4}$$
$$F_{ks} = K_s u_s \tag{B.5}$$
$$F_{cs} = C_s \dot{u}_s \tag{B.6}$$
$$F_{ms} = M_s \ddot{u}_s \tag{B.7}$$

Looking at the equilibrium in each node, the equations of motion for this system can be written as follows:

$$F(t) = F_{c1} \tag{B.8}$$
$$F_{c1} = F_{k2} + F_{c2} + F_{\text{fric}} \tag{B.9}$$
$$F_{k2} + F_{c2} + F_{\text{fric}} = F_{k3} \tag{B.10}$$
$$F_{k3} = F_{ms} + F_{ks} + F_{cs} \tag{B.11}$$

Next the different situation of stick and slip will be discussed separately.

B.1. Stick

For stick, the relative motion between the node with displacement u_2 and the node with displacement u_3 is impeded such that:

$$F_{k2} = K_2(u_2 - u_3) = \text{constant} \tag{B.12}$$
$$F_{c2} = C_2(\dot{u}_2 - \dot{u}_3) = 0 \tag{B.13}$$

During stick, F_{fric} is an unknown force that follows from the system of equations of motion. To remove F_{fric} from the system of equations Equation B.9 is added into Equation B.10:

$$F(t) = F_{c1} \tag{B.14}$$
$$\dot{u}_2 = \dot{u}_3 \tag{B.15}$$
$$F_{k3} = F_{c1} \tag{B.16}$$

B.2. Stick-to-slip transition

Stick-to-slip transition occurs when the friction threshold of the slider element F_{crit} is met. This condition is independent of the direction of the loading. Therefore, the stick-to-slip transition occurs when:

$$|F_{\text{fric}}| > F_{\text{crit}} \tag{B.17}$$

The friction force F_{fric} can now be derived from Equation B.9 or Equation B.10. However, for convenience it is chosen to use Equation B.10.

$$F_{\text{fric}} = F_{k3} - F_{k2}^{C} \tag{B.18}$$

Where the force F_{k2} is denoted with a C as it is constant during stick. It must be noted that in a physical sense F_{fric} cannot exceed the threshold F_{crit}. Therefore, a more correct way to formulate the condition for stick-to-slip transition would be:

$$|F_{\text{appl}}^{\text{fric}}| > F_{\text{crit}} \tag{B.19}$$

Where $F_{\text{appl}}^{\text{fric}}$ is the applied load to the slider element and is defined by:

$$F_{\text{appl}}^{\text{fric}} = F_{k3} - F_{k2} = F_{\text{fric}} + F_{c2} \tag{B.20}$$

This way of checking if the sliding element is in stick or slip is used in the numerical model developed in this thesis. Since the sliding element may be a confusing concept, the reader is reminded that the focus of this appendix is to prove that if Equation B.19 is true, slip occurs and stick occurs otherwise.

As during stick $F_{c2} = 0$, the friction force is always equal to the applied force:

$$F_{\text{fric}} = F_{\text{appl}}^{\text{fric}} \quad \text{stick} \tag{B.21}$$

Furthermore, during slip the friction force is always equal to the threshold:

$$F_{\text{fric}} = F_{\text{crit}} \quad \text{slip} \tag{B.22}$$

B.3. Slip

During slip the following conditions apply:

$$F_{k2} = K_2(u_2 - u_3) \neq \text{constant} \tag{B.23}$$
$$F_{c2} = C_2(\dot{u}_2 - \dot{u}_3) \neq 0 \tag{B.24}$$
$$F_{\text{fric}} = F_{\text{crit}} \tag{B.25}$$

This changes the system of equations into:

$$F(t) = F_{c1} \tag{B.26}$$
$$F_{c1} = F_{k2} + F_{c2} + F_{\text{crit}} \tag{B.27}$$
$$F_{k2} + F_{c2} + F_{\text{crit}} = F_{k3} \tag{B.28}$$
$$F_{k3} = F_{ms} + F_{ks} + F_{cs} \tag{B.29}$$

B.4. Slip-to-stick transition

Slip occurs until the relative motion between the node with displacement u_2 and the node with displacement u_3 becomes zero or changes direction. Considering the latter, the threshold F_{crit} must first be overcome in the opposite direction. This is hypothetically possible.

However, it will cost a certain amount of time to reach the threshold in the other direction. The time step must therefore be chosen such that this moment can be captured. The condition for slip-to-stick transition is thus:

$$\text{sgn}(\dot{\epsilon}_2(t)) \neq \text{sgn}(\dot{\epsilon}_2(t - \Delta t)) \tag{B.30}$$

Where:

$$\dot{\epsilon}_2(t) = \dot{u}_2(t) - \dot{u}_3(t) \tag{B.31}$$

Since $F_{c2} = C_2(\dot{u}_2 - \dot{u}_3)$, Equation B.30 can be written as:

$$\text{sgn}(F_{c2}(t)) \neq \text{sgn}(F_{c2}(t - \Delta t)) \tag{B.32}$$

To properly consider the transition from slip to stick, the following situation is considered: Slip-to-stick transition in the case that during slip, the nodes with displacements u_2 and u_3 move towards each other. It is assumed that at time $t - \Delta t$ slip occurs, and that at time t stick occurs. At time $t - \Delta t$ the system is in slip. Therefore, one could combine Equation B.20 and Equation B.25 to:

$$F^{\text{fric}}_{\text{appl}}(t - \Delta t) = F_{\text{crit}} + F_{c2}(t - \Delta t) \tag{B.33}$$

As the nodes with displacements u_2 and u_3 move towards each other, it follows that:

$$F^{\text{fric}}_{\text{appl}}(t - \Delta t) > 0 \tag{B.34}$$

$$\dot{\epsilon}_2(t - \Delta t) = \dot{u}_2(t - \Delta t) - \dot{u}_3(t - \Delta t) > 0 \tag{B.35}$$

$$F_{c2}(t - \Delta t) > 0 \tag{B.36}$$

From which follows that during slip:

$$|F^{\text{fric}}_{\text{appl}}(t - \Delta t)| > F_{\text{crit}} \tag{B.37}$$

Next, the time t is considered at which $\dot{\epsilon}_2(t)$ becomes 0 exactly. Equation B.33 now becomes:

$$F^{\text{fric}}_{\text{appl}}(t) = F_{\text{crit}} + F_{c2}(t) \tag{B.38}$$

$\dot{\epsilon}_2(t) = 0$ results in $F_{c2}(t) = 0$, and therefore:

$$|F^{\text{fric}}_{\text{appl}}(t)| = F_{\text{crit}} \tag{B.39}$$

Since there are no other forces to induce a relative motion between the nodes with displacements u_2 and u_3, it must be that the sliding element sticks. Thus, as soon as $\dot{\epsilon}_2(t) = 0$, the force applied to the sliding element is insufficient to remain in the slip regime and thus

stick occurs. For the next time step it is not known if stick or slip will occur. It solely depends on the internal forces in the system.

Finally, it is considered that the exact time at which $\dot{\epsilon}_2(t) = 0$ is passed and thus the sign changes.

$$\text{sgn}(\dot{\epsilon}_2(t)) \neq \text{sgn}(\dot{\epsilon}_2(t - \Delta t)) \tag{B.40}$$

Again, the equality of Equation B.33 becomes:

$$F_{\text{appl}}^{\text{fric}}(t) = F_{\text{crit}} + F_{c2}(t) \tag{B.41}$$

As the exact moment where $\dot{\epsilon}_2(t) = 0$ first occurred is passed, and since the sign changed, it must be that $\dot{\epsilon}_2(t) < 0$. As a consequence $F_{c2}(t) < 0$ as well. From this follows that:

$$|F_{\text{appl}}^{\text{fric}}(t)| < F_{\text{crit}} \tag{B.42}$$

It now follows that if Equation B.40 holds, Equation B.42 also holds. The only situation where Equation B.42 would be true and the element would still be in slip, is where $F_{\text{appl}}^{\text{fric}}(t)$ has changes so fast that $F_{\text{appl}}^{\text{fric}}(t) < -F_{\text{crit}}$ and slip occurs in the opposite direction. This would mean that $F_{c2}(t) \leq -2F_{\text{crit}}$ which is impossible for the system it is applied to.

Bibliography

K. Blenkarn. Measurement and analysis of ice forces on Cook Inlet structures. *Offshore Technology Conference*, 1970. doi: 10.4043/1261-MS. URL http://www.onepetro.org/mslib/servlet/onepetropreview?id=OTC-1261-MS.

Charlotte Boesen and Henriette Corlin Hassing. Nysted wind farm. URL http://188.64.159.37/graphics/Publikationer/Havvindmoeller/kap03.htm.

Karla Jean Booth. Real Snow Flake, 2014. URL http://www.realsnowflakephotography.com/.

DONG Energy. DONG Energy wins tender for Dutch offshore wind farms, 2016. URL http://www.dongenergy.com/en/media/newsroom/news/articles/dong-energy-wins-tender-for-dutch-offshore-wind-farms.

Ernst & Young et Associés. Offshore wind in Europe, 2015. ISSN 1502SG448.

European Commission. Paris Agreement, 2015. URL http://ec.europa.eu/clima/policies/international/negotiations/paris/index{_}en.htm.

Lennart Fransson and Jan-eric Lundqvist. a Statistical Approach To Extreme Ice Loads on Lighthouse. pages 1–6, 2006.

Gregg Freebury and Walter Musial. Determining equivalent damage loading for full-scale wind turbine blade fatigue tests. *2000 ASME Wind Energy Symposium*, (February): 12, 2000. doi: 10.2514/6.2000-50. URL http://arc.aiaa.org/doi/abs/10.2514/6.2000-50.

Henri P Gavin. Structural Element Stiffness, Mass, and Damping Matrices, 2014.

Hayo Hendrikse. *Ice-induced vibrations of vertically-sided offshore structures*. PhD thesis, TU Delft, 2017.

Hayo Hendrikse and Andrei Metrikine. Interpretation and prediction of ice induced vibrations based on contact area variation. *International Journal of Solids and Structures*, 75-76:336–348, 2015a. ISSN 00207683. doi: 10.1016/j.ijsolstr.2015.08.023.

Hayo Hendrikse and Andrei Metrikine. Edge indentation of ice with a displacement-controlled oscillating cylindrical structure. *Cold Regions Science and Technology*, 121(0): 100–107, 2015b. ISSN 0165232X. doi: 10.1016/j.coldregions.2015.10.013.

P V Hobbs. *Ice Physics*. Clarendon Press, 1974. ISBN 9780198519362.

Guojun Huang and Pengfei Liu. A Dynamic Model for Ice-Induced Vibration of Structures. *Journal of Offshore Mechanics and Arctic Engineering*, 131(February):011501, 2009. ISSN 08927219. doi: 10.1115/1.2979795.

ISO 19906. Petroleum and natural gas industries ÂŮ Arctic offshore structures. *International Standard*, 2010(50), 2010. ISSN 1545-0279. doi: 10.5594/J09750.

I. J. Jordaan. NRC Publications Archive Archives des publications du CNRC. 2000. doi: 10.1023/B.

T Karna, K Kamesaki, and H Tsukuda. A numerical model for dynamic ice Âś structure interaction. 72:645–658, 1999.

Arnold D. Kerr. On the determination of horizontal forces a floating ice plates exert on a structure. 20(82), 1978.

S Løset, K Shkhinek, and K V Høyland. *Ice Physics and Mechanics*. Trondheim, 1998.

Mauri P. Määttänen. On Conditions For The Rise Of Self-excited Ice-Induced Vibrations. 1978.

Hudson Matlock, William P. Dawkins, and John J. Panak. A Model for the Prediction of Ice-Structure Interaction. *First Offshore Technology Conference*, pages 687–694, 1969.

M. Matsuiski and T. Endo. Fatigue of Metals Subjected to Varying Stress. *Japan Soc. Mech. Eng., Fukuoka*, 1969.

B Michel and N Toussaint. Mechanisms and Theory of Indentation of Ice Plates. 19:532–552, 2000.

Maren Pauly Mills and Tristan. Sea Ice Types & Seasonality, 2016.

Naoki Nakazawa and D. S. Sodhi. Ice Forces on Flat , Vertical lndentors Pushed Through Floating Ice Sheets. (May), 1990.

Chris Petrich and Hajo Eicken. Growth Structure and Properties of Sea Ice. In *Sea Ice*, chapter 2, pages 23–77. 2010. ISBN 9781405185806. doi: 10.1002/9780470757161.

Harold R. Peyton. Ice and Marine Structures. pages 59–65, 1968.

Daniel J Rixen. *Numerical methods in Engineering Dynamics*. 2012. ISBN 9780521852876.

E M Schulson and P Duval. *Creep and Fracture of Ice*. 2009. ISBN 0521806208. doi: 10.1017/CBO9780511581397.

N.K. Sinha. Creep model of ice for monotonically increasing stress. *Cold Regions Science and Technology*, 8:25–33, 1983.

Devinder S. Sodhi. Nonsimultaneous crushing during edge indentation of freshwater ice sheets. *Cold Regions Science and Technology*, 27(3):179–195, 1998. ISSN 0165232X. doi: 10.1016/S0165-232X(98)00010-X.

DS Sodhi, FD Haynes, K Kato, and K Hirayama. Experimental determination of the buckling loads of floating ice sheets. *Proceedings of the 2nd . . .* , 1983.

T Takeuchi and M Sakai. On the factors influencing the scaling of ice forces. *Solid Mechanics and Its Applications*, pages 149–160, 2001.

G. W. Timco. Laboratory observations of macroscopic failure modes in freshwater ice. In *International Cold Regions Engineering Conference*, volume 6, pages 605–614, 1991. ISBN 0872627985.

G. W. Timco and W. F. Weeks. A review of the engineering properties of sea ice. *Cold Regions Science and Technology*, 60(2):107–129, 2010. ISSN 0165232X. doi: 10.1016/j.coldregions.2009.10.003.

P.L.C. Van der valk. *Coupled Simulations of Wind Turbines and Offshore Support Structures*. 2014. ISBN 9789462036819.

Herman Frederik Veldkamp. *Chances in Wind Energy - A Probablistic Approach to Wind Turbine Fatigue Design*. PhD thesis, 2006.

VGB PowerTech e.V. Levelised Cost of Electricity. Technical report, 2015.

W. F. Weeks and S.F. Ackley. The Growth, Structure, and Properties of Sea Ice. In *The Sea Geophysics Ice of Sea Ice*, chapter 1, pages 9–164. 1986. ISBN 9781489953544.